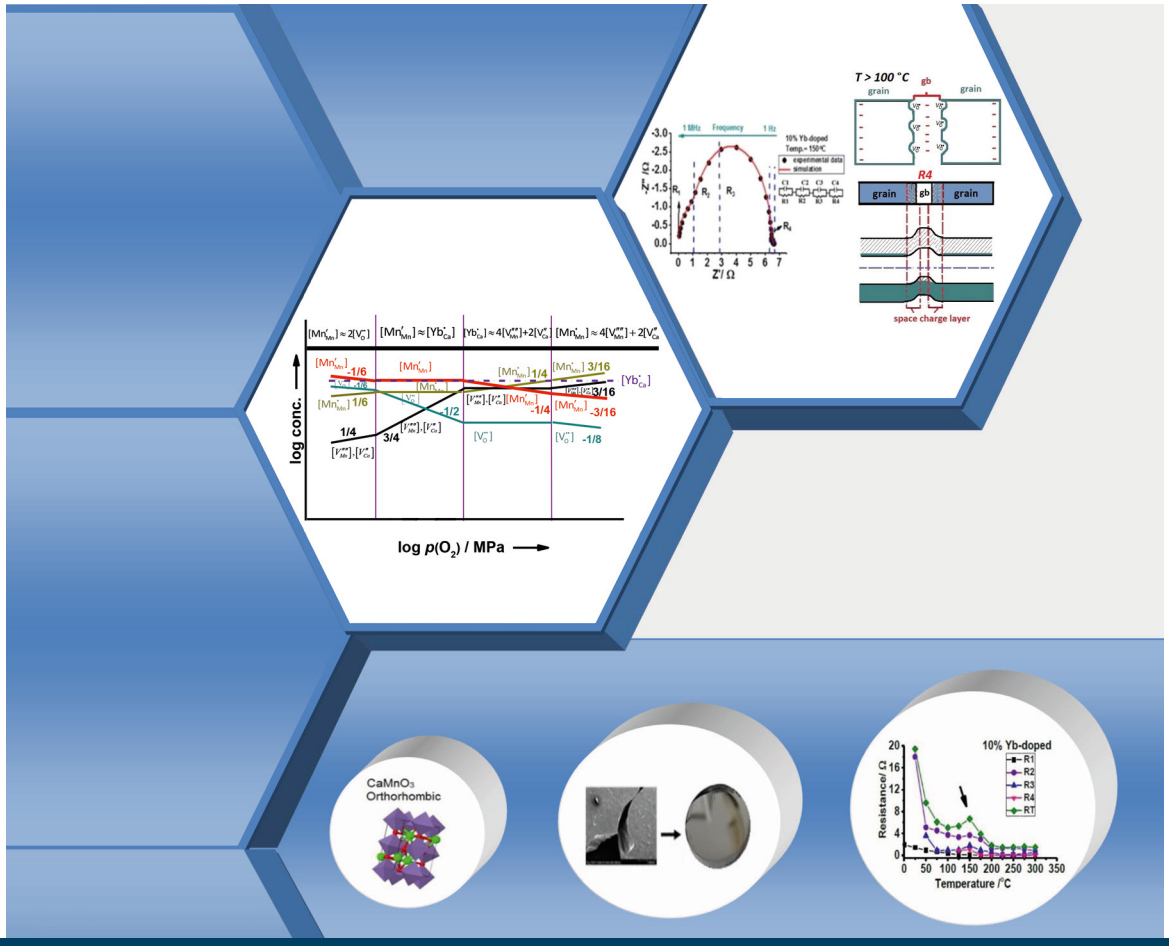

Optimization of powder and ceramic processing, electrical characterization and defect chemistry in the system $Yb_xCa_{1-x}MnO_3$

Meimanat Rahmani

Information
Band / Volume 54
ISBN 978-3-95806-323-5

Mitglied der Helmholtz-Gemeinschaft

JÜLICH
Forschungszentrum

Schriften des Forschungszentrums Jülich
Reihe Information / Information Band / Volume 54

Forschungszentrum Jülich GmbH
Peter Grünberg Institut (PGI)
Elektronische Materialien (PGI-7)

Optimization of powder and ceramic processing, electrical characterization and defect chemistry in the system $Yb_xCa_{1-x}MnO_3$

Meimanat Rahmani

Schriften des Forschungszentrums Jülich
Reihe Information / Information Band / Volume 54

ISSN 1866-1777 ISBN 978-3-95806-323-5

Bibliografische Information der Deutschen Nationalbibliothek.
Die Deutsche Nationalbibliothek verzeichnet diese Publikation in der
Deutschen Nationalbibliografie; detaillierte Bibliografische Daten
sind im Internet über http://dnb.d-nb.de abrufbar.

Herausgeber und Vertrieb:	Forschungszentrum Jülich GmbH Zentralbibliothek, Verlag 52425 Jülich Tel.: +49 2461 61-5368 Fax: +49 2461 61-6103 zb-publikation@fz-juelich.de www.fz-juelich.de/zb
Umschlaggestaltung:	Grafische Medien, Forschungszentrum Jülich GmbH
Druck:	Grafische Medien, Forschungszentrum Jülich GmbH
Copyright:	Forschungszentrum Jülich 2018

Schriften des Forschungszentrums Jülich
Reihe Information / Information, Band / Volume 54

D 82 (Diss., RWTH Aachen, Univ., 2018)

ISSN 1866-1777
ISBN 978-3-95806-323-5

Vollständig frei verfügbar über das Publikationsportal des Forschungszentrums Jülich (JuSER)
unter www.fz-juelich.de/zb/openaccess.

Kurzfassung

Die gemischtvalenten Erdalkalimanganite $RE_xA_{1-x}MnO_3$ mit ihrer sehr reichhaltigen und komplexen Kristallphysik und -chemie haben in letzter Zeit viel Aufmerksamkeit auf sich gezogen. Zwei innovative potentielle Anwendungen für Manganite unt Seltenen Erden sind nichtflüchtige Speicher, die auf resistivem Schalten- beruhen sowie Abwärmerückgewinnungstechniken durch thermoelektrische Generatoren basieren. Der Widerstandsschaltmechanismus und die thermoelektrischen Eigenschaften hängen stark von der Konzentration und der Art der Ladungsträger ab. Der Mechanismus der Defektchemie, der an diesen Prozessen beteiligt ist, wurde noch nicht klar verstanden. Der Informationsmangel in der Literatur ist sicherlich auch auf die Komplexität dieses Materialsystems zurückzuführen, da Mangankationen in solchen quaternären Oxiden mehrere Valenzzustände besitzen Können. Der andere Grund liegt möglicherweise in der Bildung von Rissen oder der Verformung von keramischen Verbindungen in dem Pulver während elektrischer Messungen under stark reduzierenden Bedingungen.

Daher wurden in der vorliegenden Arbeit erstmals umfassende Untersuchungen durchgeführt, die beim Sintern auftretende Rissbildung zu reduzieren oder zu verhindern. Zu diesem Zweck wird die Wirkung verschiedener Kalzinierungs- und Sinterbedingungen auf die physikalischen Eigenschaften von stöchiometrischen, nicht stöchiometrischen (Ca-Überschuss und Mn-Überschuss) und 0,1 bis 10 at. % Yb-dotierten $CaMnO_3$-Keramiken in Abhängigkeit von Temperatur T und Sauerstoffpartialdruck $p(O_2)$ untersucht. Nach dem Auffinden der erforderlichen Parameter zur Herstellung der gewünschten rissfreien Keramiken, wie Kalzinierungstemperatur, Sintergaszusammensetzung und Heiz- / Kühlraten usw., wurden elektrische Charakterisierungen durchgeführt, einschließlich DC-Leitfähigkeits- und Impedanzspektroskopiemessungen.

Leitfähigkeitsmessungen werden durch Impedanzspektroskopie durchgeführt, wobei die Verbindungen in Form einer elektrischen Ersatzschaltung in einem weiten Bereich von Temperaturen und Frequenzen modelliert werden. Diese Experimente zeigen die Hauptrolle von Korngrenzen und elektronischen und ionischen Beiträgen in der Leitfähigkeit. Eine neuartige schematische Darstellung basierend auf dem Doppel-Schottky-Barrieren-Modell für polykristalline Keramiken wird vorgeschlagen, die den Beitrag verschiedener Widerstandskomponenten zu elektrischen Transporteigenschaften deutlich beschreibt. Die Migration von Sauerstoffleerstellen und ihre Beteiligung an der Leitfähigkeit werden in der vorliegenden Studie diskutiert, und die Ergebnisse werden durch Beobachtung von Sauerstoff, der mit einem ZrO_2-Sauerstoffsensor bei Dilatometrie-Messungen in einem breiten Temperaturbereich freigesetzt wurde, bestätigt.

Das Defektchemie-Modell soll die Details der Chemie von Punktdefekten klären. Dieses theoretische Modell, begleitet von experimentellen DC-Leitfähigkeitsmessungen, Dilatometrie-Analysen, SEM-, EDX-, XRD-Messungen, Raman-Spektroskopie, iodometrischen Titrationen und thermogravimetrischen (TGA) Experimenten, zeigt sowohl ionische- als auch elektronische Ladungstransportleitfähigkeit in Abhängigkeit vom Sauerstoffpartialdruck $p(O_2)$ für Donator-dotierte $Yb_xCa_{1-x}MnO_3$-Systeme. Ein Vergleich der experimentellen Beobachtungen und der theoretischen defektchemischen Modelle zeigt deutlich, wie Ladungsträger in Abhängigkeit von $p(O_2)$ - und Dotierstoffkonzentrationen gesteuert werden können. Eine negative Steigung der elektrischen Leitfähigkeit gegen $p(O_2)$ zeigt an, dass eine Leitfähigkeit vom n-Typ auftritt. Eine p (O_2) -unabhängige Leitfähigkeit (Plateau-Bereich) wird sowohl für undotiertes als auch für Donator-dotiertes $CaMnO_3$ beobachtet. Elektrische Messungen, begleitet von einer thermischen Analyse und einer Bewertung der Phasenreinheit zeigen, dass der Ursprung der Plateau-Bereich in der Leitfähigkeit auf einer intrinsischen oder extrinsischen elektronischen Kompensation beruht. In diesem Bereich beeinflussen Sauerstoffionen wahrscheinlich aufgrund der Bildung von Sekundärphasen die Elektronen- und Lochkonzentrationen nicht wesentlich. Zusätzlich wird der Ursprung der drastischen Abnahme der Leitfähigkeit im Reduktionsbereich aufgeklärt.

Insgesamt demonstrieren die vorliegenden Experimente deutlich die Wirkung der Donator-Dotierstoffkonzentration, die Bildung von Sauerstoffleerstellen und die entsprechende Änderung der Dichte der Mn^{3+}-Mn^{4+} -Paarstellen am Phasenübergangs-, Ladungsverschiebungs- und Leitfähigkeitsmechanismus des komplexen Systeme $Yb_xCa_{1-x}MnO_3$. Die erhaltene Information wird wahrscheinlich nützlich sein, um den Leitungsmechanismus in zukünftigen technologischen Anwendungen besser zu verstehen.

Abstract

Mixed valence alkaline earth manganites $RE_xA_{1-x}MnO_3$ with very rich and complex crystal physics and chemistry have attracted a great deal of attention recently. Two innovative potential applications for rare earth manganites are non-volatile memories based on resistive switching and waste heat recovery techniques by thermoelectric generators. The resistive switching mechanism and thermoelectric properties strongly depend on the concentration and nature of the charge carriers. Defect chemistry mechanism involved in these process have not been understood clearly yet. The lack of information in the literature is certainly also due to complexity of this material system, since manganese cations possess several valence states in the quaternary oxide. The other reason possibly is due to the formation of cracks or deformation of ceramic compounds in to the powder during electrical measurements in the reduction regions.

Therefore, in the present thesis comprehensive studies were performed for the first time in order to find the way for reducing or preventing crack formation that occurs during sintering. For this purpose the effect of different calcination and sintering conditions on the physical properties of stoichiometric, non-stoichiometric (Ca-excess and Mn-excess) and 0.1 to 10 at. % of Yb-doped $CaMnO_3$ ceramics were investigated in dependence of temperature T and partial pressure of oxygen $p(O_2)$. After finding the required parameters to produce desired crack free-ceramics such as calcination temperature, sintering gas composition types and heating/cooling rates, etc., electrical characterizations were performed including DC-conductivity and impedance spectroscopic measurements.

Bulk conductivity measurements are performed by impedance spectroscopy accompanied by modeling the compounds in terms of an electrical equivalent circuit in a wide range of temperatures and frequencies. These experiments reveal the main role of grain boundaries and electronic and ionic contributions in conductivity. A novel schematic illustration based on the double-Schottky-barrier model for polycrystalline ceramics is proposed which clearly describes the contribution of different resistance components in electric transport properties. Migration of oxygen vacancies and their participation in conductivity are discussed in the present study and the results are confirmed by observing oxygen released using a ZrO_2 oxygen sensor during dilatometry measurements in a wide range of temperatures.

The defect chemistry model is proposed to clarify the details of the chemistry of point defects. This theoretical model accompanied by experimental DC-conductivity measurements, dilatometry analysis, SEM, EDX, XRD-measurements, Raman spectroscopy, iodometric titration and thermogravimetric (TGA) experiments reveal ionic as well as electronic charge transport conductivity contribution in dependence of the oxygen partial pressure $p(O_2)$ for donor-doped $Yb_xCa_{1-x}MnO_3$ systems. A comparison of the experimental observations and the theoretical defect chemical models clearly show the way for controlling charge carriers in dependence of $p(O_2)$ and dopant concentrations. A negative slope of electrical conductivity versus $p(O_2)$ indicates that n-type conductivity occurs. A $p(O_2)$ independent conductivity (plateau region) is observed for both undoped and donor-doped $CaMnO_3$. Electrical measurements accompanied by thermal analysis and phase purity assessment reveal that the origin of the plateau region in conductivity is due to intrinsic or extrinsic electronic compensation. In this region probably due to formation of secondary phases oxygen ions do not considerably influence the electron and hole concentrations. In addition, the origin of the drastic decrease in conductivity at reduction region is elucidated.

Overall, the present experiments clearly demonstrate the effect of donor dopant concentration, formation of oxygen vacancies and corresponding change in density of Mn^{3+}-Mn^{4+} pair sites on phase transition, charge migration and conductivity mechanism of the complex systems $Yb_xCa_{1-x}MnO_3$. The obtained information probably will be useful for better understanding the conduction mechanism in future technological applications.

Contents

List of figures

List of tables

1 Introduction

Electronic oxides with a perovskite type or related crystallographic structures exhibit a large variety of interesting functional properties making them indispensable for the use in many electronic devices and possibly in future novel applications in information and energy technology [1]. Typical applications of these materials are solid state electrolytes e.g. for fuel cells [2], membranes for gas separation [3], catalysts [4] and sensors [5]. The outstanding spectrum of different physical functions includes electric conduction or insulation, which may be tuned by external magnetic or electric fields, di-, ferro-, piezo- or pyroelectric polarization as well as electro- and magnetooptical activity. All of these properties can be widely modified according to the desired functionality by variations in the composition, stoichiometry, crystallography or materials morphology and microstructure [6,7]. As an illustrating example electrical conductivity might be considered, which can range over many orders of magnitude from highly insulating oxides over semi-conduction to metallic behavior or even to superconducting characteristics. Perovskites thus show a remarkable flexibility in properties within the field of solid state science and engineering. One of the reasons for this extensive richness and variability of physical properties is the fact that the crystal structure of the perovskite lattice tolerates considerable distortions and may be formed by a multitude of cationic and anionic chemical species. Additionally perovskite type oxides can accommodate large concentrations of mobile charged lattice defects – electronic as well as ionic ones. The chemical description of deviations from the perfect ordered crystalline state in inorganic materials and the effect of such disorder on their properties are treated by the field of defect chemistry which describes qualitatively or quantitatively point-type lattice disorder [8].

A prominent example of material systems that have extensively been studied in the past with respect to its defect chemistry are alkaline earth titanates. The description of the electrical properties in dependence of the partial pressure of oxygen $p(O_2)$ and temperature T in terms of defect chemistry in single crystalline and bulk ceramic titanates for both cases of acceptor- and donor-doped compositions has been widely studied since the late 1960s [9-18]. On the basis of the defect chemical reactions observed, kinetic exchange processes of oxygen with the atmosphere and changes of

the valence state regarding their individual thermal activation and thermodynamically equilibria [9-12], reliability and degradation effects of passive electronic devices for instance multilayer capacitors [5-17] or semiconducting resistors with positive temperature coefficient [12] could be widely understood and improved. Figure 1-1 represents two illustrative examples obtained by the measurement of DC-conductivity respectively at elevated temperatures for different partial pressures of oxygen $p(O_2)$. Both cases shown were described for $BaTiO_3$ in some earlier reports [15,16].

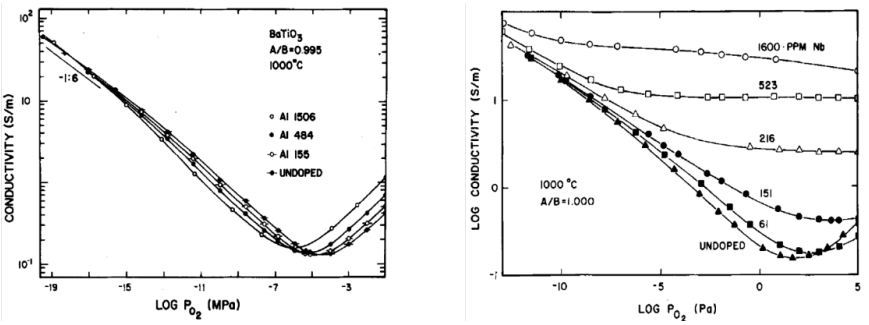

Figure 1-1: Equilibrium electrical conductivity in dependence of the oxygen partial pressure $p(O_2)$ for undoped and acceptor-doped $BaTiO_3$ (left side, Ba/Ti-ratio = 0.995, Al-doping [15]) and donor-doped $BaTiO_3$ (right side, Ba/Ti-ratio =1, with increasing additions of Nb [16]), at 1000°C.

At lower concentrations of oxygen n-type semi-conduction occurs and the corresponding defect chemical equilibrium according to the formalism of Kröger and Vink [18] may be formulated as follows:

$$O_O^{\times} \rightleftarrows \frac{1}{2}O_2^{(g)} + V_O^{\bullet\bullet} + 2e^- \qquad \textbf{Eq. 1-1}$$

Below the critical partial pressure of oxygen, where n-type conduction is observed oxygen vacancies and electrons are formed in the crystal lattice of the perovskite phase under the release of oxygen gas to the ambient. The formation of oxygen vacancies originates from intrinsic reduction or from the incorporation of an aliovalent acceptor dopant. In the present case of the example shown in Figure 1-1 (left side) trivalent Al^{3+}cations partially substitute tetravalent Ti^{4+}cations:

$$Al_2O_3 + 2BaO \longrightarrow 2Ba_{Ba}^{\times} + 2Al_{Ti}' + 5O_O^{\times} + V_O^{\bullet\bullet} \qquad \textbf{Eq. 1-2}$$

In higher $p(O_2)$ region charge neutrality can be approximated by $[A_{Ti}'] \approx 2[V_O^{\bullet\bullet}]$. This equation demonstrates that, in this high $p(O_2)$ regime concentration of oxygen vacancies

$[V_O^{\bullet\bullet}]$ will be fixed at a level two times lower than the acceptor level $[A'_{Ti}]$ and will be independent of $p(O_2)$. Here generally a minimum value of conductivity arises at a particular partial pressure of oxygen, which depends on the level of acceptor doping. According to this charge neutrality electron and hole concentrations can be calculated with the value of the slopes -1/4 and +1/4, respectively. The mentioned slopes of the conductivity and concentrations versus $p(O_2)$ cause a typical conductivity minimum where the concentrations of electron and hole are equal. The calculations are presented and discussed in more detail in the section 2.1.3.6. With increasing $p(O_2)$ the concentration of hole will be more than electron concentrations, therefore this region is called p-type regime.

If temperature is sufficiently high, in the high oxidizing regime, above the critical partial pressure, oxygen vacancies in the lattice are filled and electron holes become the majority charge carriers, according to the oxidation reaction:

$$\frac{1}{2}O_2^{(g)} + V_O^{\bullet\bullet} \rightleftharpoons O_O + 2h^{\bullet} \qquad \textbf{Eq. 1-3}$$

Analogous considerations can be made for the donor-doped case, shown in the right part of Figure 1-1. Here the donor-dopant is either compensated by electrons or by metal vacancies, e.g. of titanium (V_{Ti}'''') in the oxidizing regime, whereas oxygen vacancies ($V_O^{\bullet\bullet}$) are formed under strongly reducing conditions.

Comparable to titanates that were treated above, rare earth modified and mixed valence alkaline earth manganites $RE_xA_{1-x}MnO_3$ (RE represents a rare earth element such as La, Nd, Yb, Pr etc., and A a divalent alkaline earth metal such as Ca or Sr) crystallizing in the perovskite structure also reveal a very rich and complex crystal physics and chemistry.

Generally, many manganites show orbital-, charge- or spin-ordering. They may be magnetically ordered or disordered and are electrically either insulating or conducting. The physical properties of these compounds depend on the nature of the A and B cations, their content and in particular on the ordering of oxygen vacancies that affects the coordination of the cations. Historically, they led to the formulation of new physical concepts such as double exchange and the formation of Jahn-Teller polarons [19].

Some manganites, in particular compositions of the system $La_xSr_{1-x}MnO_3$ are employed as cathode material in solid oxide fuel cells [20]. Numerous compositions such as $La_{0.67}Ca_{0.33}MnO_3$ show a remarkable magnetoresistive effect being responsible for a drastic reduction of resistivity when a magnetic field is applied. This so called GMR- or CMR-effect (giant or colossal magnetoresistive effect) [21,22] which is illustrated in Figure 1-2 makes manganites attractive for applications in magnetic sensors or reading heads as well as in magnetoresistive random access memories. As can be recognized from Figure 1-2 the properties and the quality of such oxide GMR-materials strongly depend on the oxidation process. Despite of this large variety of interesting physical properties and the technologically highly relevant applications they imply, the defect chemistry describing the lattice point disorder in manganites is, however, dissimilar as in titanates only partially and often not sufficiently known or understood [23].

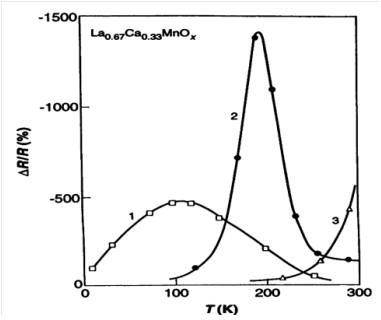

Figure 1-2: Temperature dependence of the magnetoresistive ratio ΔR/R for $La_{0.67}Ca_{0.33}MnO_3$ thin films prepared by pulsed laser deposition (PLD) in pure O_2 at different conditions: (1) as deposited, (2) annealed for 0.5 hour at 700°C, (3) annealed for 3 hours at 900°C in pure oxygen [21].

Among these perovskite type functional oxides, rare earth modified $CaMnO_3$ based ceramics have attracted much attention recently driven by their potential applications in information technology as well as in energy harvesting. In the first case they are believed to be very promising candidate materials for resistive switching memory cells (ReRAM: resistive random-access memory cells) [24]. They could also play an important role in high temperature ceramic thermoelectric generators [25]. With respect to this latter potential application considerable research activities have been devoted also due to extraordinary advantages such as their environmentally ecological compatibility [26], economical raw materials [27], high thermal stability [28]. The pure undoped perovskite type compound $CaMnO_3$ is an n-type semiconducting oxide and exhibits antiferromagnetic ordering below its Néel temperature (T_N) of 130K. Coexistence of different magnetic ordered states was reported in $CaMnO_{3-\delta}$ nanoparticles with

antiferromagnetic (AFM) structure in the core and ferromagnetism (FM) in the shell [29,30].

The incorporation of dopants introduces significant changes in the electrical and magnetic properties of this material [31, 32, 33]. The electrical and magnetic properties of $CaMnO_{3-\delta}$ are influenced by the oxygen content as well as the valence states of manganese which can be Mn^{2+}, Mn^{3+}, or Mn^{4+} in the solid state [34]. Most of the previously reported investigations are concentrated on acceptor-doped $RE_{1-x}A_xMnO_3$ perovskite manganites (where A represents a divalent alkaline earth cation substitute for RE which is a trivalent lanthanide cation) [35,36]. However, donor-doped (i.e. substitution of trivalent ions at the Ca-site in $CaMnO_3$) allows the injection of electrons at low concentration in the Mn^{4+} sublattice which is of great interest since it promotes metal-like resistivity-temperature behavior and possibly improves thermoelectric properties such as the Seebeck coefficient (S), electrical conductivity (σ) and thermal conductivity (κ). Nevertheless, the effect of nonstoichiometry on these properties as well as on the conduction mechanism is not understood comprehensively.

The electric transport properties of $RE_xCa_{1-x}MnO_3$ related material systems are expected to be strongly depended to the chemistry of point defects that determines the kind and concentration of the electronic or ionic majority charge carriers. Only very limited and incomplete information on this subject is published in the literature [23].

Furthermore only very few reports describe systematically the ceramic technology of powder formation and consolidation by sintering with respect to parameters like gas composition and temperature.

The present thesis therefore aims to elaborate and supply a comprehensive overview on the lattice disorder in such systems. This report focuses on pure $CaMnO_3$, as well as a non-stoichiometric $CaMnO_3$, as a potential n-type material for practical thermoelectric applications at elevated temperatures in air [37]. More specifically $Yb_xCa_{1-x}MnO_3$ based material systems are discussed.

In the present work, following aspects and questions have been attempted to address:

- Systematical optimization of ceramic synthesis and processing procedure.
- Eventual effects of different calcination conditions on the physical properties after sintering.

- The role of stoichiometry and non-stoichiometry (A/B-ratio, Ca- & Mn-excess), oxygen deficiency on morphology and physical properties.
- Role of the Mn^{3+}/Mn^{4+} concentration ratio on conductivity.
- The influence of the thermodynamic parameters temperature *T* and partial pressure of oxygen $p(O_2)$ on the phase stability in the quaternary oxide system $Yb_xCa_{1-x}MnO_3$ (x = 0.1 up to 10 at %).
- Theoretical and experimental investigation on the role of oxygen vacancies regarding chemical and electrical properties of ceramics.
- What kind of electronic and/or ionic contributions of conductivity originate from the bulk (volume effect) and from interfaces?
- How do grain boundaries affect the electrical properties of quaternary oxide ceramic $Yb_xCa_{1-x}MnO_3$ (x=0.1 up to 10 at %)?
- Identification and Quantification of the defect chemistry in the mentioned material system.

For this purpose, materials compositions of $CaMnO_3$-based ceramics of this study have been modified systematically starting with stoichiometric and non-stoichiometric compounds with Ca- or Mn-excess according to the concentration of the respective rare earth cation in the overall composition. Ytterbium doped $CaMnO_3$ based compositions with a dopant level ranging from 0.1 to 10 at % have also been prepared. Accordingly the Mn^{3+}/Mn^{4+} ratio as well as the proportion of A-site cations (Yb^{3+}, Ca^{2+}) relative to the overall Mn-content (degree of stoichiometry) has been varied.

The present thesis describes in chapter 1 and 2 the fundamental properties of $CaMnO_3$ based ceramic and the state of the art reported in literature. The theory of electrical properties of metals, semiconductors, and insulators are explained in chapter 3. Chapter 4 describes and introduces the experimental procedures applied. All materials prepared were thoroughly characterized regarding to their microstructure (electron microscopy), phase purity and crystallography (X-ray diffraction, XRD, in combination with Rietveld refinements of the corresponding diffraction patterns) as well as to their chemical compositions (chemical analysis). Iodometric titration served as a valuable method for determining the valence states of the Mn-cations and of oxygen deficiency.

Moreover, the phase stability in dependence of temperature *T* and partial pressure of oxygen $p(O_2)$ was evaluated. Systematic studies on the stoichiometric, non-stoichiometry and doped $CaMnO_3$ are presented in chapter 5. In order to understand the role of bulk conductivity contributions (electronic and/or ionic) these studies were complemented by impedance spectroscopic measurements of the electrical complex AC-resistivity for polycrystalline ceramics. These results are reported in chapter 6. Finally, to further clarify which defect chemical reaction dominates in particular limits of different oxygen concentrations $p(O_2)$, experimentally determined of DC conductivity is compared with proposed defect chemistry models for undoped as well as for rare earth-doped $CaMnO_3$ (acceptor and donor- doped) are described in chapter 7. The present thesis concludes with a summary in chapter 8.

.

2 State of the art

The compound calcium manganite $CaMnO_3$ and many of its doped or substitutionally modified compositional derivatives crystalizes in the so called perovskite lattice structure. The crystallography of the ideal form of cubic ABO_3 perovskite represents an ionic arrangement of corner sharing BO_6 octahedra. A and B generally represent metallic ions. The cation A is situated in a twelve-fold oxygen coordination site in the center between eight of such BO_6 octahedra [19]. Generally, perovskite structures are not perfectly cubic in symmetry but rather distorted depending on the size of the cations, deviations from the ideal ABO_3 composition, e.g. variations of the valency of Mn ions in $Ca^{2+}\ Mn^{3+}/Mn^{4+}\ O^{-2}_{3-\delta}$ by heating a sample in oxidizing or reducing condition, and/or the Jahn-Teller effect (energy lowering by splitting the energy level of 3d ions such as Mn^{3+}, which is due to the distortion of the oxygen octahedron surrounding the B site cation). Reducing symmetry in distorted perovskites has a significant influence on their electric and magnetic properties. These properties attract much attention with respect to their potential practical applications. Especially for n-type semiconducting rare earth modified $CaMnO_3$ this concerns promising thermoelectric [31] and resistive switching proprieties [24].

2.1 Fundamental principles of perovskites ABO_3

2.1.1 Crystallography

In many compounds containing oxygen ions and divalent transition metals (valence +2), e.g. MnO, oxygen ions form a cubic close packed lattice (ccp) with metal ions located in octahedral interstitials formed by the oxygen anions. If additional cations e.g. from alkali, alkaline earth or rare earth elements are added to such a structure, they occupy octahedral lattice voids and thus the number of such unoccupied sites is reduced. The resulting crystal structure is ABO_3 perovskite. In the ABO_3 structure the crystallographic A site is generally occupied by a larger cation, such as Ba^{2+}, Ca^{2+}, Sr^{2+}, K^{+}, or Na^{+}, (r_A > 0.09 nm [38]) which is 12-fold coordinated by oxygen. The B site generally hosts smaller cations (r_B > 0.051 nm [38]) like Ti^{3+}or Ti^{4+}, Nb^{5+}, Ta^{5+}, Mn^{3+} or Mn^{4+}, and is six-fold coordinated by oxygen anions O^{2-}, as shown in Figure 2-1.

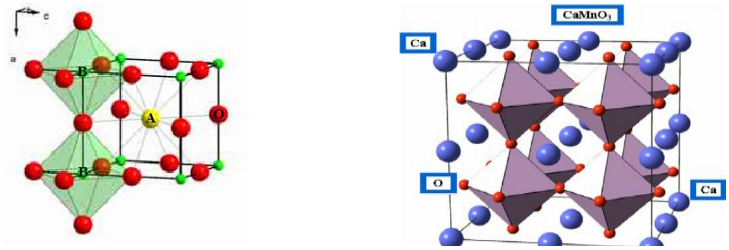

Figure 2-1: Ideal crystallographic unit cell of cubic perovskite oxides with ABO_3 structure (left side). Oxygen ions are octahedrally coordinated around B cations, and A cations occupy the 12-fold coordination sites formed in between these polyhedra. The right side shows the cubic perovskite oxide of $CaMnO_3$ as an ideal perfect crystal [39,40]

The perovskite structure is mostly distorted due to different factors which are described below:

- **Changing the size of the cations**

In a perovskite oxide the radii of the contained ions are related to each other by the formula of $(r_A+r_O)=t\sqrt{2}(r_B+r_O)$ [19], where t is the Goldschmidt's tolerance factor which is equal to unity (1) in a perfect crystal with cubic perovskite structure. Reduction in the size of the A cation changes the bonding length between A cations and oxygen anions. Therefore, BO_6 octahedra tilt in order to accommodate such distortions. As a result, t becomes smaller than one and the symmetry of the crystal structure decreases. In the case of large A cations or small B cations, the tolerance factor will be more than one. Hence, the cubic lattice of perovskites may change into a hexagonal structure. As shown in Figure 2-2, $GdFeO_3$ and $BaNiO_3$ with a tolerance factor less or larger than one, respectively, indicate examples of distorted perovskite structures.

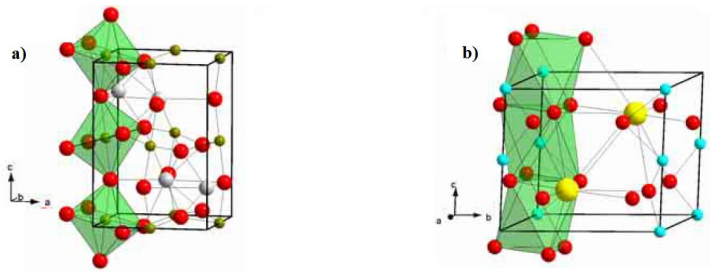

Figure 2-2: Distorted perovskite ABO_3, a) crystallization in an orthorhombic system for $GdFeO_3$ with t=0.81, b) $BaNiO_3$ with a hexagonal structure and a t value of 1.13 [39].

- **Deviations from the ideal stoichiometric ABO_3 composition**

The ideal structure of perovskite compounds ABO_3 can also be distorted by changing the valance state of the B cations. As an example, the valance of Mn in inorganic compounds ranges from -3 to +7 [41]. The tetravalent manganese cation in the compound $Ca^{2+}Mn^{4+}O_3$ can be changed to trivalent Mn^{3+} also by annealing in reducing atmosphere. Accordingly, the crystallographic structure might change. To illustrate this variability in structure Figure 2-3 shows examples of the compounds $Ca^{2+}Mn^{4+}O_3^{2-}$, $Ca^{2+}Mn^{4+}O_3^{2-}$, $Ca^{2+}Mn_2^{3+}O_4^{2-}$ and $Ca_2^{2+}Mn^{4+}O_4^{2-}$.

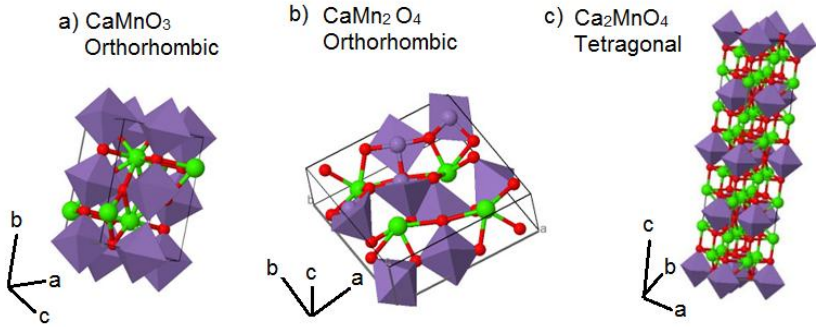

Figure 2-3: Unit cell for the crystal structure of a) $Ca^{2+}Mn^{4+}O_3^{2-}$ [42], b) $Ca^{2+}Mn_2^{3+}O_4^{2-}$ [43], and c) $Ca_2^{2+}Mn^{4+}O_4^{-2}$ [44].

- **Jahn – Teller distortion**

The so called Jahn–Teller effect at the B position in perovskite type crystals may be another reason for lattice distortions in the perovskite structure. The d-orbitals of transition metals are generally of five types, t_{2g}=d_{xy}, d_{yz}, d_{zx} and e_g=$d_{3z^2-r^2}$, $d_{x^2-y^2}$, as shown in Figure 2-4. For instance, the electronic configuration of Mn cations in bulk $CaMnO_3$ is t^3_{2g} e^0_g (Mn^{4+}). Since three t_{2g} orbitals are symmetric and fully occupied, energetic splitting does not exist (Figure 2-4). However, in the case of „electron-doped" $CaMnO_3$, e_g orbitals can also be occupied partially. If an electron hops into an empty e_g orbital, a distortion of the octahedral structure of oxygen atoms lowers the symmetry and further splits the e_g and t_{2g} levels [45]. Therefore, MnO_6 octahedra will be distorted in the direction of the e_g orbital. This phenomenon is referred to the Jahn-Teller effect. The electron with its accompanying lattice distortion forms a so-called lattice polaron.

Generally, polarons are of two types: large and small polarons. Large polarons are itinerant entities, while small polarons in real materials have a tendency to self-trap themselves in form of localized states [46,47].

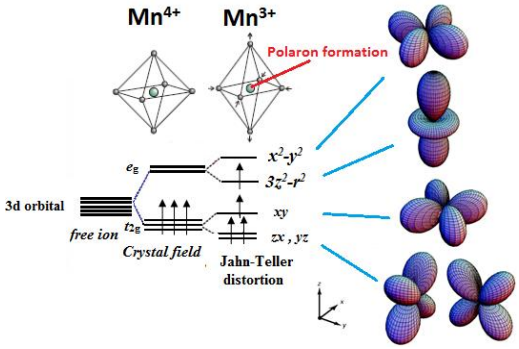

Figure 2-4: Schematic illustration of crystal-field splitting of the five-fold degenerated atomic 3d-levels into lower t_{2g} (triply degenerated) and higher e_g (doubly degenerated) levels, the Jahn–Teller distortion of the MnO_6 octahedron that further lifts the degeneracy, polaron formation, and five types of d-orbitals in transition metals (right side) [48,49].

2.1.2 Electronic and magnetic properties of perovskites

The chemical flexibility of oxides with a perovskite ABO_3 structure in combination with their complex nature of transition metal ions located in certain coordinations with oxygen lead to a considerable diversity in electronic and magnetic properties.

The present thesis focuses on electronic oxides based on the stoichiometric compound $CaMnO_3$. This type of perovskite manganite with complex electronic, magnetic, and structural phase diagrams, has been known for its charge-, spin-, and orbital- (lattice) ordering which can be induced by double-exchange interaction, (which is a type of a magnetic exchange that may arise between ions in different oxidation states), super-exchange interaction (which involves virtual electron transfer), and Jahn–Teller-type electron–lattice distortion, etc. These properties and transition phenomena are described in more detail below.

2.1.2.1 Exchange interaction

The Coulomb energy between two electrons depends on their relative spins, since electrons with identical spin cannot occupy the same orbital. This Coulomb exchange is the basis of Hund's first rule. In systems with more than one atom, electrons can hop

from one site to a neighboring one. However, this kinetic aspect is restricted by the Pauli principle in a way that the hopping to an orbital on the neighboring atom will only be possible, if there is not already an electron of the same spin occupying that orbital and by the Coulomb repulsion among the electrons (Figure 2-5). In Kinetic exchange, the resulting interactions prefer antiparallel spins.

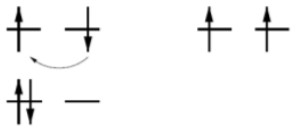

Figure 2-5: Direct exchange and electron hopping between antiparallel alignment of the spins (left side) is allowed, but for parallel spins (right side) the Pauli principle prevents hopping [50].

In transition-metal oxides, relatively large oxygen anions separate transition-metal cations (d- orbitals). Therefore, it is improbable to have direct electron hopping between the d-orbitals [51]. In this case, hopping via the intermediate p-orbital of oxygen can be considered, which is called “super-exchange” (SE) mechanism. This mechanism depends on the geometrical arrangment of the oxygen ion between the two d-orbitals, as illustrated in Figure 2-6.

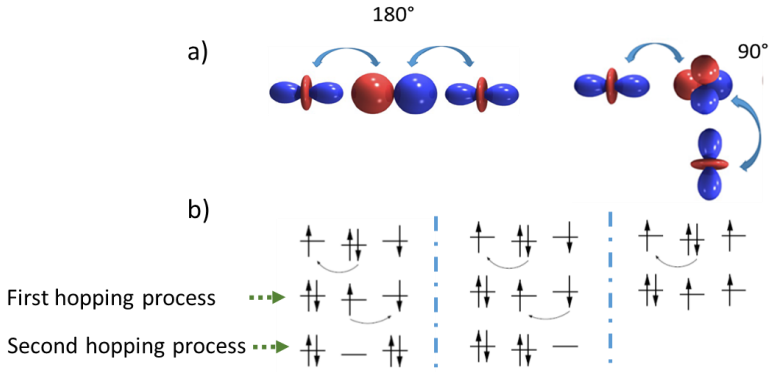

Figure 2-6: In the super-exchange mechanism a central oxygen p-orbital couples with two neighboring d-orbitals of Mn cations and mediates the exchange interaction. a) Dependence of super-exchange on geometry. b) There are two possible ways of sequential hopping for antiparallel spins on the d-orbitals. For parallel spins, the second hopping process is prevented according to the Pauli principle [50].

If the bonding angle of M-O-M (M: Metal, O: Oxygen) is 180° antiferromagnetic super-exchange will occur. If the orbitals are arranged in a 90° configuration, the d-orbitals couple to orthogonal p-orbitals, making it impossible for an electron on one d-orbital to reach the d-orbital on the other site. In this condition, super-exchange is mediated via the Coulomb exchange on the connecting oxygen and weak ferromagnetism is predicted. When Coulomb exchange and kinetic exchange work together, we speak of double-exchange. In this respect the 90° super-exchange mechanism is a double-exchange (DE) mechanism. More commonly, the DE mechanism is expected in mixed valence compounds [50].

The double exchange mechanism (DE) has attracted considerable attention after the discovery of the metallic ferromagnetic state in $La_{1-x}Ca_x(Mn^{3+}_{1-x}Mn^{4+}_x)O_3$ by Jonker and van Santen [52]. Some research has been done in order to find the theoretical relation between conductivity and ferromagnetism [53, 54, 55]. Due to Hund's coupling, the spins of electrons in the t_{2g} and e_g states of Mn cations are aligned parallel to each other. As shown in Figure 2-7, if Mn^{3+} and Mn^{4+} cations are neighbors and the spins of their d-shells are aligned in parallel, the e_g electron from Mn^{3+} can hop on an empty e_g state at the Mn^{4+} site. This results in an exchange of the valence states. However, in the case of antiparallel spins the hopping is prevented by the Hund's coupling. Hence, there exist a strong correlation between the metallic state and ferromagnetism. This transport mechanism was suggested by Zener and is known as "double-exchange". This mechanism is always ferromagnetic, different from super-exchange suggested by Kramers [56], which involves indirect electron transfer between transition-metal cations with the same valence through the intermediate p-orbital of an anion and is frequently antiferromagnetic.

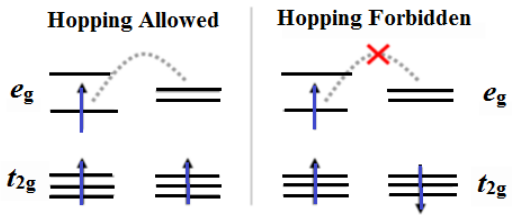

Figure 2-7: Double-Exchange (DE) interaction [50]

2.1.2.2 Charge-, spin- and orbital-ordering

Besides the double-exchange (DE) interaction and Hund's coupling, there are also some other important factors affecting the physical properties of ion-doped perovskite manganite [57]:

(i) electron–lattice interaction,

(ii) ferromagnetic (FM) or antiferromagnetic (AFM) super-exchange (SE) interaction between local spins,

(iii) inter-site exchange interaction between the e_g orbitals (orbital ordering tendency),

(iv) intra-site and inter-site Coulomb repulsion interaction between the e_g electrons.

These interactions/instabilities compete with the ferromagnetic DE-interaction and produce complex electronic phases and interesting phenomena such as colossal magnetoresistance (CMR), i.e., drastic change in electrical resistance under an applied magnetic field [18, 58].

For instance, in the compound $LaMnO_3$ [59] which contains Mn^{3+} cations, one electron occupies one of two possible d orbitales. The degeneracy of the e_g orbitals is eliminated due to the Jahn–Teller distortion and then $d_{3z^2-r^2}$ and $d_{x^2-y^2}$ orbitals are ordered (Figure 2-4). Depending on orbital-ordering and its direction double-exchange interaction or super-exchange interaction occurs and thus gives a complex spin-orbital coupled state. If the spins are arranged in parallel to each other ferromagnetism (FM) results. Antiferromagnetism (AFM) occurs when they are arranged in an anti-parallel manner. Basically, there are four types of magnetic ordering in perovskites, as shown in Figure 2-8. F-type ordering indicates ferromagnetism, A-type ordering contains ferromagnetically aligned xy planes that are coupled antiferromagnetically, C-type ordering consists of ferromagnetic chains oriented antiparallel to each other, and in G-type ordering, all nearest neighbor manganese cations are coupled antiferromagnetically.

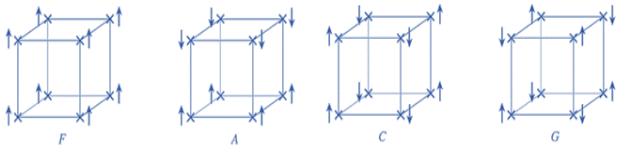

Figure 2-8: Different types of magnetic ordering configurations for B cations in ABO_3 perovskite cubic lattice [60].

If a divalent cation such as Ca^{2+} is doped to the compound $LaMnO_3$ substituting La^{3+}, the electrons redistribute to give some Mn^{4+} ions with an empty d-orbital (a hole). By the formation of "electron-vacancy" sites (or "hole-doping") the e_g electron can hop between two manganese cations depending on the relative configuration of the local spins. Therefore, the material behaves as a metallic conductor. Besides, if 30 or 40 percent of acceptor doped manganite is cooled below the ferromagnetic (FM) transition temperature, T_c (i.e., Curie temperature, where the paramagnetic state transforms into the FM state or vice and versa), the spins of these electrons align so that the material becomes ferromagnetic. Since aligned electrons scatter oppositely-aligned electrons trying to pass through, the resistivity increases [61]. Therefore, a large magnetoresistance can be expected around T_c. The colossal magnetoresistance (CMR) phenomenon is most relevant to the orbital-charge correlation. Charge-ordering is localization of charges due to strong interactions between electrons. It is coexisting with symmetry breaking which leads to insulating and antiferromagnetic or paramagnetic behavior. Charge-ordering (CO) in manganites means an ordered arrangement of Mn^{3+}/Mn^{4+} cations in some special range of dopant concentration [62]. Figure 2-9 shows the charge and orbital configuration for $La_{0.5}Sr_{0.5}MnO_4$ compound, as an example.

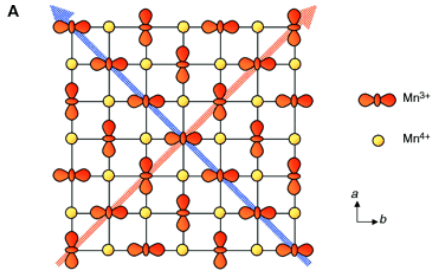

Figure 2-9: Charge- and orbital-ordering along a ab-plane in $La_{0.5}Sr_{0.5}MnO_4$ [49].

In the case of donor-doped $CaMnO_3$, for instance $(La,Ca)MnO_3$, the valency of the Mn ions is mixed, since the valence state in pure $LaMnO_3$ is 3+ and in $CaMnO_3$ is 4+. The ionic size of Mn^{3+} is significantly larger than the size of Mn^{4+} ions, and additionally, Mn^{3+} is a good Jahn-Teller ion. Antiferromagnetic super-exchange coupling exists between Mn^{4+} ions via an oxygen ion between the two d-orbitals. However, depending on the relative orbital ordering, the super-exchange interaction between Mn^{3+} ions via intervening oxygen can be antiferromagnetic or ferromagnetic. The real hopping of the e_g electron between Mn^{3+} and Mn^{4+} through an oxygen produces a ferromagnetic coupling in the double exchange mechanism. Hence, charge carriers, magnetic coupling, and structural distortion in mixed valent $La_xCa_{1-x}MnO_3$ have an effect on each other [63]. Electron doped $CaMnO_3$ (donor-doping) is one of the most preferred colossal magnetoresistance (CMR) compounds due to the high efficiency and small disorder [64, 65]. In addition, the strong correlation between the charge-ordered and the charge-delocalized states in these systems strongly influences the CMR properties. Temperature dependence characteristics of resistivity (ρ) and magnetoresistance ($\Delta R/R_H$) for La-Ca-Mn-O film, prepared by pulsed laser deposition (PLD) and annealed at 900°C in an oxygen atmosphere was studied by S. Jin et. al, [66]. As shown in Figure 2-10, negative slopes $d\rho/dT$ above 95K represent semiconductor behavior, while positive $d\rho/dT$ below this temperature indicates metallic behavior.

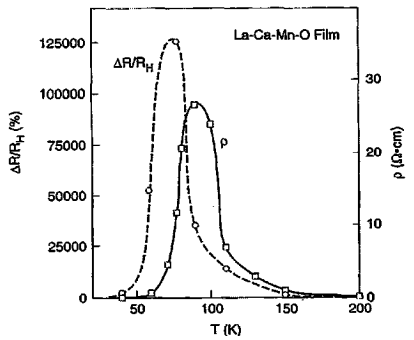

Figure 2-10: Large magnetoresistances $\Delta R/R_H$ in a La-Ca-Mn-O film within the metallic region of the resistivity $d\rho/dT > 0$ [66].

The maximum magnetoresistance ($\Delta R/R_H$) is located in the metallic-behavior region of the resistivity. The exact mechanisms responsible for the observed MR in La-Ca-Mn-O

are not clearly understood, although it seems to be related to the semiconductor- metal transition.

In addition, perovskite type oxides can accommodate large concentrations of mobile, charged lattice defects – electronic as well as ionic ones, which influence conductivity. Temperature *T* and partial pressure of oxygen are two important thermodynamic parameters in transport mechanism. It has been reported [67] that conductivity increases with raising temperature and decreasing $p(O_2)$ from 10^{-1} down to 10^{-6} MPa for compound $CaMnO_{3-\delta}$.

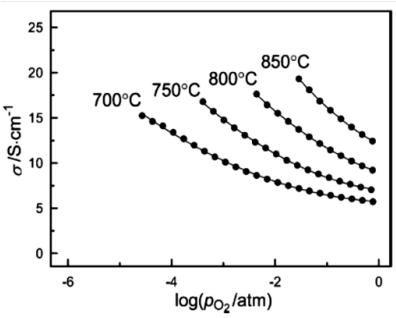

Figure 2-11: Oxygen partial pressure dependence of DC electrical conductivity measured in orthorhombic $CaMnO_{3-\delta}$ at different temperatures shows that conductivity increases with decreasing oxygen partial pressure ($p(O_2)\approx10^{-1}$-10^{-6} MPa) [67].

These results are in good agreement with present thesis. However in the present dissertation a plateau region and a drastic decrease in conductivity are also observed by further reduction lower than $p(O_2)\approx10^{-6}$ MPa and 10^{-16} MPa respectively which may be due to phase transition and defect formation. The chemical description of deviations from the perfect ordered perovskite type oxides in inorganic materials and the effect of such disorder on their properties are treated by the field of defect chemistry which describes qualitatively or quantitatively point-type lattice disorder.

2.1.3 Principal aspects of defect chemistry

2.1.3.1 Classification of defects in crystals

There are four basic classes of defects representing deviations of a real crystal from the ideal crystallographic structure. Point defects, linear defects, planar defects and bulk

defects stand for zero-, one-, two- and three-dimensional imperfections, respectively. This is demonstrated in a hierarchical scheme shown in figure 2-12.

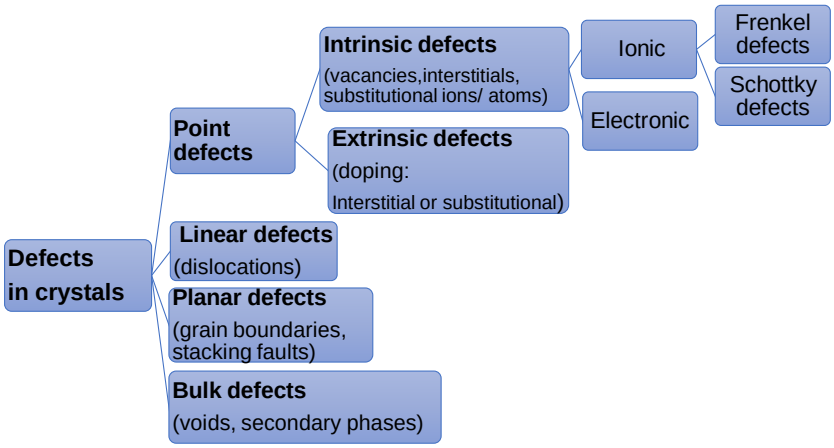

Figure 2-12: Series of defects classifications in crystals.

Defects are defined as any deviation from the ideally perfect crystal structure. Point defects involve only a single atomic species or lattice site. They always are part of the thermodynamical equilibrium and cannot be avoided. The other more complex types of defects such as dislocations (linear defects) and grain boundaries (planar defects) are generally non-equilibrium states of a crystal.

There are many different types of point defects, which are explained in more detail in section 2.1.3.5. These various defects result in different electronic conduction behavior of transition metal oxides for instance from insulating or semiconducting behavior to metallic behavior. Defect chemical models can generally describe the relation between electronic properties and the defect configuration. The basic technique of the defect chemical approach is to write down equilibrium reactions for the formation of defects and for the interaction between them. Subsequently, mathematical expressions for the correlation between the equilibrium concentrations of the different defects with temperature, and for instance the partial pressure of oxygen for oxides, and other parameters that affect the defect structure, can be formulated by the application of the law of mass action.

2.1.3.2 The equilibrium state: Gibbs free energy and the law of mass action

Generally, the change in Gibbs free energy (ΔG) associated with a process determines whether the process is energetically favorable. For an oxidation reaction or a phase transformation in which $A \longrightarrow B$ the change in Gibbs free energy is $\Delta G = G_B - G_A$, where G_B and G_A are the free energy of the final state and the initial state, respectively. Table 2-1 shows different states for change in the Gibbs free energy from which spontaneous, non-spontaneous, or equilibrium state can be determined.

Table 2-1: Change in the Gibbs free energy ΔG

$\Delta G < 0$	The reaction is spontaneous in the direction written from A to B
$\Delta G > 0$	The reaction as written does not proceed spontaneously; the reverse reaction is the spontaneous one.
$\Delta G = 0$	The process is at equilibrium and there is no net change either in forward or reverse direction.

- **Gibbs free energy ΔG in a crystal**

There is an equilibrium concentration of point defects in a crystal at a given temperature. Point defects play an important role in characterizing the properties of ceramics. Therefore determining the concentration of point defects present in thermal equilibrium is necessary. A crystal containing point defects must have a lower free energy G, than a corresponding crystal without any defects. The change in free energy ΔG and the change in enthalpy ΔH of a chemical reaction is expressed as:

$$\Delta G = \Delta H - T\Delta S \qquad \textbf{Eq. 2-1}$$

$$\Delta H = \Delta E + p\Delta V \qquad \textbf{Eq. 2-2}$$

where ΔH represents the enthalpy to form a point defect. ΔE is the change in the internal energy on forming the defect. If volume does not change in the process $p\Delta V = 0$, thus $\Delta H = \Delta E$. The internal energy of the disordered crystal is the energy of the perfect crystal plus nE, where n indicates the number of point defects. The nearest neighbors and the interatomic bonding affect E. The formation of point defects results in the breaking of chemical bonds and this costs energy. Therefore, the internal energy increases when the number of point defects increases [68].

Such disorder should occur under equilibrium condition, therefore another term must be considered in order to balance the enthalpic cost of introducing disorder to the lattice [8]. According to thermodynamics, equilibrium at constant pressure is defined as the state in which the system has its minimum value of the Gibbs free energy, so there is an entropy term $T\Delta S$ that must be subtracted from enthalpy contribution. The product $T\Delta S$ increases by increasing point defects.

Consider a perfect crystal with N atoms as starting material with N atomic sites. By moving atoms from a regular crystallographic site of the lattice in the bulk to the surface of the crystal, unoccupied sites as vacancies (defects) are formed. The number of vacancies formed (N_v) thus is added to the total number of sites in $N + N_v$. The entropy change includes modified vibrational modes (S_v) of the atoms in the vicinity of each vacancy, and a configurational entropy contribution (S_c) which is related to the distribution of N_v vacancies among $N + N_v$ sites. The enthalpy of formation of each vacancy ΔH, in combination with the entropy associated with the formation of the defects ΔS, give rise to the change in the Gibbs free energy. Consequently, the change in Gibbs free energy corresponding to the formation of vacancies (N_v) can be expressed as:

$$\Delta G = N_v (\Delta H - T\Delta S_v) - T\Delta S_C \qquad \textbf{Eq. 2-3}$$

The configurational entropy can be written in terms of the thermodynamic probability, W, in the form of an equation of $\Delta S_C = k_B \ln W$, where k_B is Boltzmann's constant, and W indicates the number of distinct ways in which vacancies (N_v) may be distributed on $N+N_v$ lattice sites. W is expressed as:

$$W = (N + N_v)!/N!N_v! \qquad \textbf{Eq. 2-4}$$

The change of the configurational entropy ΔS_C can be expressed according to the Stirling's approximation ($\ln x! = x \ln x - x$ for $x \gg 1$), as follows:

$$\Delta S_C = k_B [(N + N_v) \ln(N + N_v) - (N + N_v) - N \ln N + N - N_v \ln N_v + N_v]$$

$$= k_B [(N + N_v) \ln(N + N_v) - N \ln N - N_v \ln N_v] \qquad \textbf{Eq. 2-5}$$

This equation can be substituted into Eq.2-3.

ΔG will be a minimum with respect to N_v at equilibrium i.e. $\partial \Delta G/\partial N_v = 0$:

$$\partial \Delta G/\partial N_v = \Delta H - T\Delta S_v - \partial/\partial N_v \{k_B T [(N + N_v) \ln(N + N_v) - N \ln N - N_v \ln N]\}$$

$$\approx \Delta H - T\Delta S_v - k_B T \ln((N + N_v)/N_v) = 0 \qquad \textbf{Eq. 2-6}$$

This gives the fraction of the total number of sites that are vacant $[N_v] = N_v/(N + N_v)$ (e.g. oxygen vacancies in an oxide concentration in present thesis). The formation reaction for vacancies leads to the mass action constant $K_v(T)$, which is a function of temperature and expressed as:

$$N_v/(N + N_v) \approx \exp(\Delta S_v/k_B) \exp(-\Delta H/ k_B T) = K_v(T) \qquad \textbf{Eq. 2-7}$$

The vibrational entropy change is presented by ΔS_v, and ΔH indicates the enthalpy change per vacancy. Configurational entropy does not appear in Eq 2-7, because it was expanded and consumed in derivation. Generally, the concentration of intrinsic defects depends primarily on the enthalpic contribution and temperature, since the vibrational entropy term is comparatively small [8].

Although to create vacancies costs energy, overall G may decrease because of the entropy contributionthion. Figure 2-13 illustrates that vacancy formation lowers the free energy of the crystal until an equilibrium concentration is reached, adding too many vacancies increases G again [68].

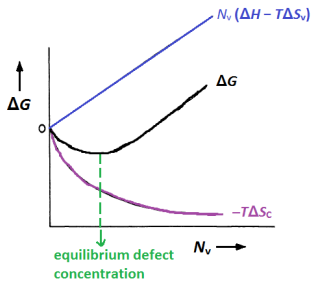

Figure 2-13: Example of the variation in Gibbs free energy (ΔG), enthalpy (ΔH) combined with the vibrational entropy (ΔS_v), and configurational (ΔS_c) entropy with the concentration of vacancies in a crystalline solid.

Consequently, the mass-action expression for a general chemical reaction in thermodynamic equilibrium can be calculated according to the following formula [8]:

$$aA + bB \rightleftharpoons cC + dD \qquad \textbf{Eq. 2-8}$$

$$\frac{[C]^c[D]^d}{[A]^a[B]^b} = K(T) = e^{-\Delta H/k_B T} e^{\Delta S_v/k_B} \qquad \textbf{Eq. 2-9}$$

where the capital letters indicate chemical species and the lowercase letters represent small integer coefficient. ΔH and ΔS determine the value of the equilibrium constant (K) at specific temperature. This mass action treatment can be used in defect chemistry.

2.1.3.3 Conservation rules

There are three essential conservation rules that should be considered in formulating and balancing defect chemical reactions. The first rule is the conservation of mass, which means that atoms or ions are neither created nor destroyed within a system. The second rule represents the conservation of charge, which indicates electrical neutrality in the bulk. The third rule is conservation of structure, which implies stoichiometric creation or annihilation of occupied cationic and anionic sites in the host compound. There is another rule which is called the conservation of electronic states, which is not related to ionic disorder, but is categorized as intrinsic electronic disorder. It refers to the fact that the total number of electronic states in a system derives directly from the electronic states of the atoms/ions contained in a compound and must be conserved.

There is a simple example and clear explanation in the book written by Smyth [8]: Consider compound M_2O_3. For Schottky disorder an electrically neutral combination of ions is moved from their normal lattice site to a new sites on a surface, leaving an electrically neutral combination of vacancies in the bulk. As discussed above, to conserve mass, charge, and lattice site ratio, it is most convenient to write the equilibrium reaction in terms of the displacement of one formula unit of the component ions. If the Schottky disorder in M_2O_3 (i.e. $nil \rightleftharpoons 2V_M''' + 3V_O^{\bullet\bullet}$ with corresponding mass-action expression $[V_M'''][V_O^{\bullet\bullet}]^3 = K_s(T) = K_s^0 e^{\Delta S_s/k_B} e^{-\Delta H_s/k_B T}$) is the major source of defects, then the expression for charge neutrality is $3[V_M'''] \approx 2[V_O^{\bullet\bullet}]$. In fact the mentioned charge neutrality expression is mathematical relationship between the concentrations. It indicates that there cannot be the same number of cation and anion vacancies, since cation and anion in compound M_2O_3 do not have the equal charges. Accordingly, the concentration of the more highly charged V_M''' requires to be 2/3 that of the lesser charged $V_O^{\bullet\bullet}$. As convenience, the correct result is always obtained if each defect in a charge neutrality expression is multiplied by the number of its defect charges [8].

2.1.3.4 Kröger–Vink notation

The defect notation used in this thesis is based on the formalism proposed by Kröger and Vink (1953) [18], as listed in table2-2. In this notation (X_Y^Z) X corresponds to the respective species under consideration, such as Mn, Ca, and O for the present thesis.

The subscript *Y* indicates the lattice or interstitial one site that the species occupies. In this work only regular crystallography sites and no interstitial are considered. The superscript (*Z*) denotes the difference in charge at the defect site relative to the charge at that site in the perfect crystal. A dot (•) is used for an extra positive charge, a slash (') for an extra negative charge and x denotes a neutral charge.

Table 2-2: Kröger–Vink notation for formulating defect chemical expressions.

X_Y^Z	
X	Nature of species located on a site: element symbol for an atom or ion, • Vacancy: V
Y	Type of the site occupied by X • Interstitial occupancy: *i* • Chemical symbol of the respective atom or ion.
Z	Electronic charge relative to the normal ion charge on the site • Negative relative charge: ' • Positive relative charge: • • Zero relative charge: X

2.1.3.5 Intrinsic and extrinsic point defects in ionic crystal

Point defects arise due to deviations in the regular arrangement around an ion or a group of ions in a crystalline substance. This kind of defects in a crystal may be classified into intrinsic defects, which could be ionic or electronic disorder, and extrinsic defects, which indicate the presence of dopant ions, dissolved in the lattice. As shown in Figure 2-14, there are three possible types for intrinsic and extrinsic ionic defects: vacancies (regularly occupied lattice sites that are empty), interstitial defects (the ions occupy a normally unoccupied interstitial site in the lattice), and substitutional defects (dopants substituting other normal ions of the crystal).

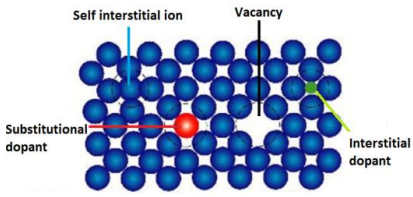

Figure 2-14: Three types of point defects: interstitial defects, vacancies, and substitutional defects [70].

If the substitutionally dissolved dopant has the same valency as the host it replaces, it is called homovalent otherwise it is known as heterovalent or aliovalent.

- **Intrinsic ionic disorder: Frenkel and Schottky defects**

Frenkel and Schottky defects are two different types of intrinsic ionic point defects. Frenkel defects were first observed in 1926 by Frenkel for AgCl [70]. They occur when the concentration of cationic or anionic vacancies are the same as cationic or anionic interstitial ions in a stoichiometric crystal. More specifically Frenkel defects with anion interstitials are called Anti-Frenkel defects. A formation reaction for a cation Frenkel pair in a related oxide MO that satisfies the mass, charge, and site balance can be written as:

$$nil \rightleftharpoons M_i^{\bullet\bullet} + V_M'' \qquad \textbf{Eq. 2-10}$$

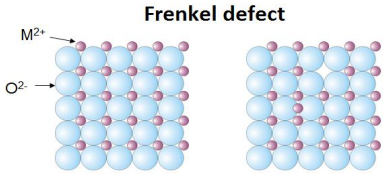

Figure 2-15: Formation of cation Frenkel disorder in MO [71].

Walter Schottky and Carl Wagner presented a systematic organization of the field of defect chemistry in the late 1920. Schottky defects are named after Walter Schottky [5]. In this model, the concentrations of cationic and anionic vacancies are equivalent in a stoichiometric crystal. The defect formation reaction of an ionic crystal MO is:

$$nil \rightleftharpoons V_M'' + V_O^{\bullet\bullet} \qquad \textbf{Eq. 2-11}$$

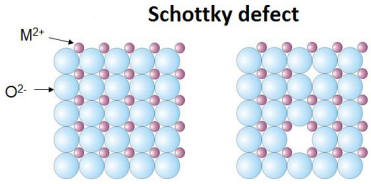

Figure 2-16: Formation of Schottky defect in MO [71].

Schottky and Frenkel disorder may be simultaneously present in a chemical compound, but one type of disorder usually predominates. For instance, when the structure is very effectively packed then the interstitial defects (Frenkel disorder) are not favorable and Schottky type disorder prevails.

- **Intrinsic electronic disorder**

A missing electron (a hole) can be formed, if an electron does not occupy its lowest available energy state in the valence band E_v, because it has been transferred to another higher energetic level [8]. This type of defect is known as intrinsic electronic disorder involving the thermal excitation of electrons from the chemical bonds of a solid material into higher energy states (Figure 2-17). In contrast to intrinsic ionic disorder which exists in many different types e.g. cationic Frenkel, anionic Frenkel, and Schottky defects, etc., there is only one equilibrium ionization reaction for the intrinsic electronic disorder, which can be expressed by:

$$\text{nil} \rightleftharpoons e' + h^{\bullet} \qquad \textbf{Eq. 2-12}$$

where *e* and *h* represent an electron and a hole, respectively.

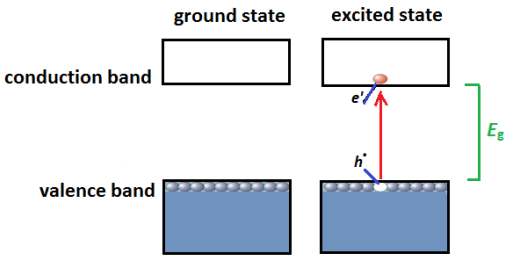

Figure 2-17: Intrinsic electronic disorder.

2.1.3.6 Defect chemistry of titanates

A prominent example of material systems that have been extensively studied in the past with respect to their defect chemistry are alkaline earth titanates. The description of the electrical properties in dependence of the partial pressure of oxygen $p(O_2)$ and temperature *T* in terms of defect chemistry in single crystalline and bulk ceramic titanates for both cases of acceptor and donor-doped compositions has been widely reported since the late 1960s [6, 9-16].

In close-packed ABO_3 perovskite structures, such as $BaTiO_3$ and $SrTiO_3$, vacancies are more favorable than interstitials, and hence anionic Frenkel disorder can be neglected [5]. Accordingly theoretical calculations show that the enthalpies of formation for Schottky disorder reactions are much lower than for Frenkel defects, and therefore in $SrTiO_3$ and $BaTiO_3$ Schottky type disorder is predominant. In addition, undoped $SrTiO_3$

and $BaTiO_3$ nominally are always slightly acceptor doped, since small impurity concentrations of transition metal ions with a lower valency than that of Ti^{4+} cations originating from the raw materials (such as Al^{3+} or Mn^{3+}) cannot completely be avoided.

2.1.3.6.1 Defect chemistry for acceptor-doped $SrTiO_3$

Point defect chemistry for the compound $SrTiO_3$ has been widely studied experimentally as well as theoretically [72, 73, 74,75, 76]. In stoichiometric $SrTiO_3$, the empty 3d-orbitals of the titanium ions form the conduction band while the valence band is formed by the contribution of occupied 2p-orbitals of the oxygen ions. $SrTiO_3$-like perovskite-type oxides have a densely packed crystal lattices; hence, Schottky disorder is the only possible type of intrinsic disorder. If the associated equilibrium constants are known, the concentrations of point defects can be predicted by defect-chemical modeling (Kröger–Vink diagram), as a function of the thermodynamic variables, such as temperature *T* and oxygen partial pressure $p(O_2)$. The number and kind of active defect equilibria determining the defect concentrations strongly depend on the temperature range (low, intermediate, and high temperature regimes) in this type of material [77].

(i) Low temperature regime: below $T \approx 750K$

Electron and holes are generated by thermal excitation across the band gap within this low temperature region around 550 K. The recombination reaction of this internal equilibrium can be written as:

$$\text{nil} \rightleftharpoons e' + h^{\bullet} \qquad \textbf{Eq. 2-13}$$

The equilibrium constant can be formulated as:

$$n \cdot p = K_r(T) = K_r^{\circ} \exp\left(\frac{-\Delta H_r}{k_B T}\right) \qquad \textbf{Eq. 2-14}$$

where *n* and *p* indicate the electron and hole concentrations, respectively.

(ii) Intermediate temperature regime: above T≈750K

Due to the considerably activated kinetics of the oxygen exchange reaction at the intermediate temperature regime, the oxygen in the gas phase and the oxygen ions in the solid can be equilibrated. At lower temperatures the kinetics for this mechanism is

too slow. The substitution of a trivalent acceptor $[A'_{Ti}]$ in the Ti site rises to the formation of oxygen vacancies in $SrTiO_3$ which can be expressed as following reaction:

$$A_2O_3 + 2Ti_{Ti}^{\times} + O_O^{\times} \longrightarrow 2A'_{Ti} + V_O^{\bullet\bullet} + 2TiO_2 \qquad \textbf{Eq. 2-15}$$

The full charge neutrality condition for acceptor-doped $SrTiO_3$ in this temperature region is formulated as:

$$n + [A'_{Ti}] = p + 2[V_O^{\bullet\bullet}] \qquad \textbf{Eq. 2-16}$$

where n and p denote electron and hole concentrations, respectively, $[A'_{Ti}]$ represents the summation of all acceptor states, and $[V_O^{\bullet\bullet}]$ indicates the concentration of oxygen vacancies.

- **Intrinsic region**

At very low values of the partial pressure of oxygen, the loss of oxygen from the lattice to the atmosphere is the dominant mechanism, which is determined by the reduction reaction:

$$O_O^{\times} \rightleftharpoons \frac{1}{2}O_2^{(g)} + V_O^{\bullet\bullet} + 2e^{-} \qquad \textbf{Eq. 2-17}$$

The equilibrium constant of the reduction reaction is given by:

$$[V_O^{\bullet\bullet}]n^2 p(O_2)^{1/2} = K_{red}(T) = K_{red}^0 \exp\left(\frac{-\Delta H_{red}}{k_B T}\right) \qquad \textbf{Eq. 2-18}$$

In this region, the condition of charge-neutrality can be simplified as:

$$n \approx 2[V_O^{\bullet\bullet}] \qquad \textbf{Eq. 2-19}$$

- **Extrinsic region**

Increasing pressures of oxygen $p(O_2)$ reduces concentration of electrons n. when the concentration of acceptor level $[A'_{Ti}]$ is larger than n, charge-neutrality condition requires that,

$$2[V_O^{\bullet\bullet}] \approx [A'_{Ti}] \qquad \textbf{Eq. 2-20}$$

This equation demonstrates that, in this high $p(O_2)$ regime $[V_O^{\bullet\bullet}]$ will be fixed at a level two times lower than the acceptor level and will be independent of $p(O_2)$, as shown in Figure 2-18 (left-side). Substituting Eq. 2-20 into the reduction reaction (Eq. 2-18) gives electron concentrations n:

$$n=\left(\frac{2K_{red}(T)}{[A'_{Ti}]}\right)^{1/2}.p(O_2)^{-1/4} \qquad \textbf{Eq. 2-21}$$

Hole concentration p can be calculated by inserting n in oxidation reaction. The oxidation reaction can be expressed as:

$$\frac{1}{2}O_2^{(g)}+V_O^{\bullet\bullet}\rightleftharpoons O_O^{\times}+2h^{\bullet} \qquad \textbf{Eq. 2-22}$$

The mass-action expression of this oxidation reaction is formulated as:

$$\frac{p^2}{p(O_2)^{1/2}.[V_O^{\bullet\bullet}]}=K_{ox}(T)=K_{ox}^0\exp\left(\frac{-\Delta H_{ox}}{k_BT}\right) \qquad \textbf{Eq. 2-23}$$

Therefore hole concentration can be calculated:

$$p=\left(\frac{K_{ox}(T)[A'_{Ti}]}{2}\right)^{1/2}.p(O_2)^{1/4} \qquad \textbf{Eq. 2-24}$$

It is represented in the defect diagram (Figure 2-18) as straight line with a slope of −1/4 and +1/4 in a double logarithmic plot of n and p as a function of $p(O_2)$, respectively.

(iii) High-temperature regime: above T≈1250 K

Since strontium vacancies display sufficient mobility at the high-temperature regime, the partial Schottky disorder reaction can be considered,

$$Sr_{Sr}^{\times}+O_O^{\times}\rightleftharpoons V_{Sr}''+V_O^{\bullet\bullet}+SrO_{(secondary\ phase)} \qquad \textbf{Eq. 2-25}$$

The generation of a V_{Sr}''-$V_O^{\bullet\bullet}$ pairs gives rise to form a (SrO) secondary phase either at the surface of $SrTiO_3$ or wihin the crystal lattice [78]. This equation results in a simplified mass action law, where the SrO concentration [SrO] is assumed to be constant:

$$[V_{Sr}''][V_O^{\bullet\bullet}]=K_{Sch}(T)=K_{Sch}^0\exp\left(-\frac{\Delta H_{Sch}}{k_BT}\right) \qquad \textbf{Eq. 2-26}$$

As a result, the general charge-neutrality condition for acceptor-doped $SrTiO_3$, in the high-temperature regime, can be expressed as:

$$n+[A'_{Ti}]+2[V_{Sr}'']=p+2[V_O^{\bullet\bullet}] \qquad \textbf{Eq.2-27}$$

2.1.3.6.2 Defect chemical modeling for $SrTiO_3$

Electrical conductivity (σ_i) is a measure of the flux (J_i) of electrical charge carriers (product of concentration (c_i) and velocity (υ_i) of electrical charge carriers (i) per unit electric field (E) with the unit of $(\Omega\ cm)^{-1}$ or Siemens per meter.

$$\sigma_i = \frac{J_i z_i e}{E} = \frac{c_i \upsilon_i z_i e}{E} = c_i z_i e \mu_i \qquad \textbf{Eq. 2-28}$$

Therefore, electrical conductivity depends on particle charge ($z_i e$) where z_i denotes charge numbers, and mobility μ_i defined as the velocity (υ_i) per unit electric filed E. The charge carrier concentrations (c_i) in the material can be determined by defect chemistry (Kröger–Vink diagram) and the mobility (μ_i) of the charge carriers can be measured by Hall effect experiments. Here an electric field E_x with a current density j_x is applied to an electrical conductor in positive x direction. A magnetic field B points in the positive z-direction. Therefore, each electron is subjected to the Lorentz force which deflects electrons in the negative y-direction. Consequently, the electrons accumulate on one side of the conductor and a field builds up in direction to oppose their motion that is called the Hall field and balances the Lorentz force. Accordingly, the velocity can be determined and thus the number of charge carries N per unit volume can be calculated [79].

Generally, all charge defects may participate in the electrical transport, hence total conductivity includes mixed ionic and electronic conduction. The latter case consists of electron and hole conduction, represented by σ_n and σ_p, respectively. Total conductivity is expressed by the following equation:

$$\sigma_{total} = \sigma_{electronic} + \sigma_{ionic} = (\sigma_n + \sigma_p) + \sum_i c_i z_i e\ \mu_i \qquad \textbf{Eq. 2-29}$$

As an example, the total conductivity of $SrTiO_3$ for the case of oxygen vacancies as a mobile ionic species thus can be expressed as:

$$\sigma_{SrTiO_3} = e\mu_n n + e\mu_p p + 2e\mu_{V_O^{\bullet\bullet}} [V_O^{\bullet\bullet}] \qquad \textbf{Eq. 2-30}$$

Where μ_n, μ_p, and $\mu_{V_O^{\bullet\bullet}}$ indicate the mobility of electrons, holes and oxygen vacancies respectively.

Waser and his colleagues [72, 74, 76, 77] extensively studied $SrTiO_3$ as a model system to describe the lattice disorder with respect to point defects and to extended defects. The

electrical conductivity of a nominally undoped epitaxial $SrTiO_3$ thin film grown by pulsed laser deposition as a function of the equilibrium oxygen partial pressure is shown in Figure 2-18 (right side). The term of "nominally undoped" or "weakly acceptor- doped" is used, since undoped $SrTiO_3$ typically contains trivalent cation impurities such as Fe^{3+} and Al^{3+}, which when substituted for Ti^{4+} act as acceptor-dopants. Equation for the law of mass action for the equilibria described above can be used to interpret conductivity curves. Figure 2-18 (left side) demonstrates the dependence of the point defect concentration in acceptor-doped $SrTiO_3$ as a function of oxygen partial pressure at T≈400 and 1000 K.

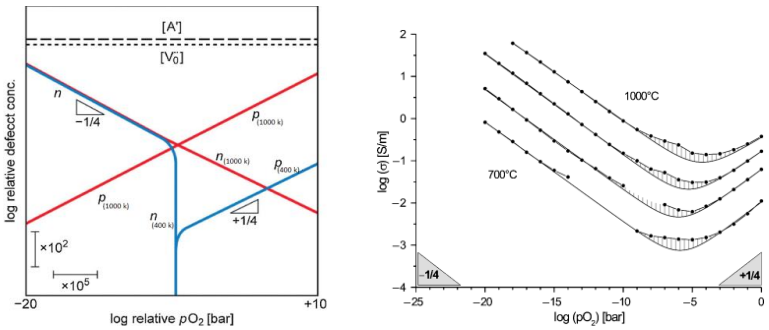

Figure 2-18: Calculated equilibrium defect concentrations for a slightly acceptor-doped $SrTiO_3$ sample as a function of $p(O_2)$ at the intermediate temperature regime, T≈1000 K and at the low temperature regime T≈400 K (left side) [74]. And, experimental (symbols) and calculated (lines) conductivities predicted from the defect model for weakly acceptor doped (possibly also a nominally undoped $SrTiO_3$ where the Sr vacancies act as native acceptor-dopants) epitaxial $SrTiO_3$ thin film with a thickness of 1 µm grown by pulsed laser deposition as a function of oxygen activity $p(O_2)$ at 700 - 1000°C (Right side) [76].

Vacancies of strontium V''_{Sr} in these temperature regimes are not mobile enough, hence the concentration of strontium vacancies $[V''_{Sr}]$ is a constant and the defects are frozen-in. However, oxygen vacancies are much more mobile and may lead to an ionic conductivity even at room temperature. The electron (n) and hole (p) concentrations cause a typical conductivity minimum. At this point contributions of electrons and holes must be equal and conductivity is at an intrinsic minimum value. This can be expressed as:

$$\sigma_n = ne\mu_n = pe\mu_p = \sigma_p \qquad \textbf{Eq. 2-31}$$

As mentioned above (Eq.2-21 and 2-24) the slope of the conductivity and concentrations versus $p(O_2)$ equal -1/4 and +1/4 at both sides of the minimum.

2.1.3.6.3 Defect chemistry of donor-doped $BaTiO_3$

Some of the first investigations on the physicochemical aspects of the point defect chemistry of donor-doped $BaTiO_3$ have been reported by Daniels, Härdtl and Hennings from the Philips research laboratory. These authors estimate the electron concentration indirectly by thermogravimetric measurements (TGA) [11] and compared the results to the DC conductivity measured as a function of oxygen partial pressure [9]. Besides, many other comprehensive studies on the preparation of $BaTiO_3$-based materials and their defect chemistry have been reported recently [80, 81, 82, 83, 84].

Kröger-Vink defect notations required for writing defect reactions for the compound $BaTiO_3$ are described in table 2-3.

Table 2-3: Kröger-Vink defect notation for $BaTiO_3$ compound.

$O_O^{\times}$ $Ba_{Ba}^{\times}$	
$Ti_{Ti}^{\times}$	
$V_O^{\bullet\bullet}$	Oxygen vacancy
V_{Ba}''	Barium vacancy
V_{Ti}''''	Titanium vacancy
$La_{Ba}^{\bullet}$	La^{3+} substituted for Ba^{2+}
n	Concentration of electrons
p	Concentration of holes

The equilibrium constants of the compound $BaTiO_3$ are slightly different from the ones for $SrTiO_3$, but the principal defect equilibria for both types of compounds are similar. The $BaTiO_3$ compound is of the closed-packed perovskite type with intrinsic Schottky type disorder.

$$nil \rightleftharpoons V_{Ba}'' + V_{Ti}'''' + 3V_O^{\bullet\bullet} \qquad \textbf{Eq. 2-32}$$

Figure 2-19 shows the calculated Kröger-Vink diagram for La-doped barium titanate at high temperature where Schottky equilibrium is active and at an intermediate temperature where Schottky equilibrium is inactive.

In the high temperature regime (above 1200°C) both, the redox and the Schottky equilibria are active. However, the Schottky reaction is considered to be frozen-in at intermediate temperatures (500 - 1000°C) for kinetic reasons. In this range of

temperatures the diffusivity of metal vacancies is too low to reach equilibration in reasonable time.

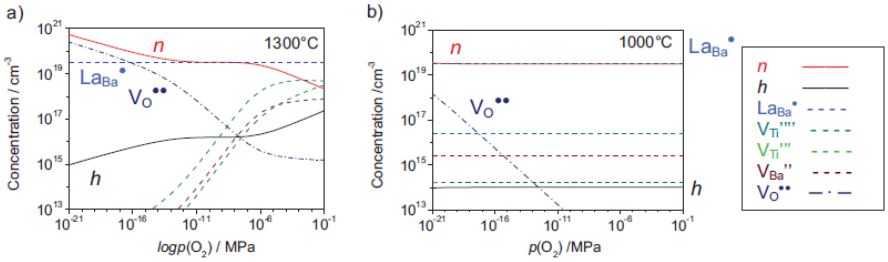

Figure 2-19: Defect diagram calculated by defect chemical modeling as a function of $p(O_2)$ for donor-doped $(Ba_{0.998}La_{0.002})TiO_{3+\delta}$ a) at 1300°C and (b) for the quenched state at 1000°C where Schottky equilibrium is frozen [83].

The large trivalent La^{3+} cations substitute Ba^{2+}-cations as donors. Generally, donors could be charge-compensated by cationic vacancies, anionic interstitials, or electrons. Due to the close packed perovskite structure of $BaTiO_3$ oxygen interstitials are not favorable. Therefore, electrical neutrality of all related charged point defects must satisfy the following equation:

$$2[V_O^{\bullet\bullet}]+p+[La_{Ba}^{\bullet}]=n+2[V_{Ba}'']+4[V_{Ti}''''] \qquad \textbf{Eq. 2-33}$$

At high partial pressures of oxygen $p(O_2)$ above 10^{-6} MPa donors are compensated by cationic vacancies, and the charge- neutrality equation can be simplified as:

$$[La_{Ba}^{\bullet}] \approx 2[V_{Ba}''] \qquad \textbf{Eq. 2-34}$$

However, this process is only possible at elevated temperatures above typically 1200°C due to kinetic reasons [83]. Compensation by electrons is otherwise the preferable case, since the conduction band, made up of reducible Ti 3d states, lies at a fairy low level [8].

In an intermediate plateau-type region (Figure 2-19) the number of electrons is fixed by the concentration of donor ions. In this regime the concentration of electrons is independent of the partial pressure of oxygen, and charge-neutrality is expressed as:

$$n \approx [La_{Ba}^{\bullet}] \qquad \textbf{Eq. 2-35}$$

When the electron concentration becomes fixed by the donor content, oxygen vacancy concentration $[V_O^{\bullet\bullet}]$ must drop off with increasing partial pressure of oxygen as $p(O_2)^{-1/2}$.

As a result, the equilibration times for these samples are extremely long and the process may not be complete at lower temperatures even after many hours. In the most highly reducing conditions when the major source of defects is a reduction reaction (Eq.2-17), the condition of charge-neutrality can be written as $n \approx 2[V_O^{\bullet\bullet}]$ and then the concentration of electrons n can be calculated from the following formula:

$$n = (2K_{red}(T))^{1/3}.p(O_2)^{-1/6} \qquad \textbf{Eq. 2-36}$$

This equation demonstrates that a straight line with slope equal to −1/6 is obtained for plots of n versus $p(O_2)$ in a logarithmic scale, at very low $p(O_2)$.

2.1.3.7 Planar defects: Grain boundaries

Up to this point, the discussion has focused on point defects of crystal with a perovskite structure. However, defect concentrations may also be influenced by planar defects, such as grain boundaries. Grain boundaries are usually considered to be two dimensional, but actually possess a finite thickness, of approximatly 2-10 atomic distances [85]. A grain boundary represents an interface between two single crystalline regions of different orientations (Figure 2-20). The different arrangement (misalignment) of the neighboring grains give rise to the various types of grain boundaries with individual physical properties. There are also other factors that influence the properties of grain boundaries, for instance grain boundary symmetry, and the presence of segregated impurity ions.

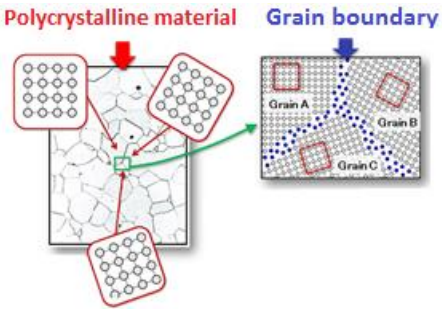

Figure 2-20: Schematic representation of grains and grain boundaries. The atoms in the grain interior have a crystalline periodic arrangement, while the atomic arrangement within the grain boundary is more disordered [86].

In perovskites grains can range in size from nanometers to millimeters by controlling the partial pressure of oxygen, cooling rate, calcination and sintering temperature. As found

in own experiments, the lower calcination temperature, the smaller grains (more grain boundary area) is achieved. Grain boundaries are the fundamental defect in polycrystalline ceramic materials, which play an important role in their electrical properties [73]. Therefore, characterization of grain boundaries is of great interest. In a broad range of ceramics, grain boundaries act as barriers for electric cross transport and increase resistivity. A double-Schottky-barrier model describes such interfaces. In these models, generally, the majority charge carriers are trapped in the grain boundary core region, which gives rise to a negative or positive net-charge of the grain boundary core. The net-charge of the interface is compensated by an opposite space charge in a depletion layer on both side of the boundary [87]. There are different suggestions defining the formation of space-charge layers. According to some reports in the literature, space-charge layers may be formed due to electronic defects being trapped at interface states [88]. Some other authors describe that, it forms because of different formation energies of anionic and cationic vacancies [89]. However, recently, the formation of space-charge layers is defined based on a generalized thermodynamic treatment of defects segregating to or away from an interface [90, 91]. Figure 2-21 schematically shows the formation of a space charge layer in a donor-doped polycrystalline ceramic.

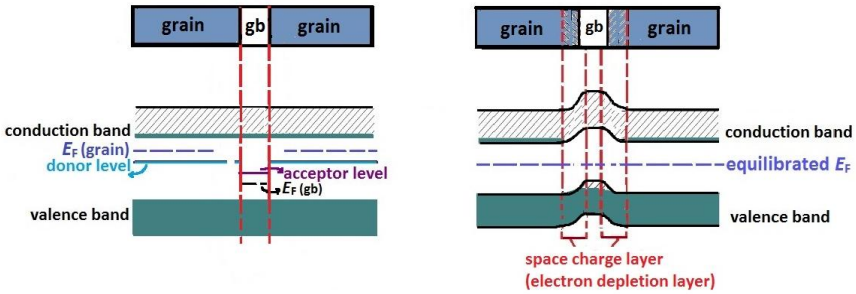

Figure 2-21: Schematic illustration for polycrystalline ceramics consisting of donor-doped grains, an acceptor state grain boundary (gb), i.e. negatively charged with electron or cation vacancies (left side), and the space charge layer, which prevents excess amount of negatively charge carriers after equilibration of Fermi level (right side).

During the sintering of a polycrystalline ceramic at very high temperatures, cationic and anionic vacancies may be formed through Schottky disorder. In the case of slow cooling, the concentration of oxygen vacancies decreases near the grain boundary, since oxygen

ions have a larger diffusivity than the other ions. This leads to the formation of cationic vacancies along the grain boundary. They act as acceptor-dopant and trapping areas of electrons [92]. The Fermi level of the grain boundary region is then depressed from the Fremi level in the grain. Therefore, a potential barrier is created between a donor-doped (n-type) grain and acceptor state (p-type) grain boundary. Negative charges (e.g. electrons) flow from the higher-level n-type grain "down" into the p-type grain boundary and thus the grain boundary is negatively charged. This proceeds until equilibrium is reached and both Fermi energies are at the same level. Equilibration of the Fermi levels results in band bending. The electrons that want to diffuse from the grain into the grain boundary encounter a potential barrier near the interface. Only a certain fraction of them has enough energy to overcome the barrier and to diffuse into the grain boundary. On the other hand, there are only a few electrons in the conduction band of p-type grain boundary. They have been thermally excited into this band by intrinsic effects. These few electrons in the grain boundary can easily diffuse "down" the potential barrier into the next n-type grain. Accordingly, in the equilibrium state, the identical number of electrons crossing the interface in both directions. By applying an electrical bias the height of the barrier is decreased, until the break down voltage is reached. Afterwards, electrons conduct across the boundary without hindering [93].

2.2 Emerging applications

Besides the rather traditional applications such as catalysts, sensors, solid electrolytes e.g. for fuel cells, actors, and membranes for gas separation, two innovative potential applications for rare earth manganites have emerged in the literature and stimulated intense scientific interest: non-volatile memories based on resistive switching [94, 95, 96] and high temperature ceramic thermoelectric generators [97,98,99].

2.2.1 Non-volatile memories based on resistive switching

A capacitor-like MIM structure, composed of an insulator or resistive material 'I' sandwiched between two electron conductors 'M', often different for the two sides, can make a resistive (switching) random access memory (RRAM) cell. In many memory cells, the first switching cycle is different from the following cycles, which is known as the "electroforming" cycle [100]. After an initial electroforming cycle, these MIM cells can be electrically switched between at least two different resistance states. A cell in its high-

resistance (OFF) state can be SET to a low-resistance (ON) state or RESET back into the OFF state, by applying voltage [74, 101].Generally, regarding to electrical polarity required for resistively switching cells, two schemes are considered which are known as unipolar switching and bipolar switching, as demonstrated in Figure 2-22.

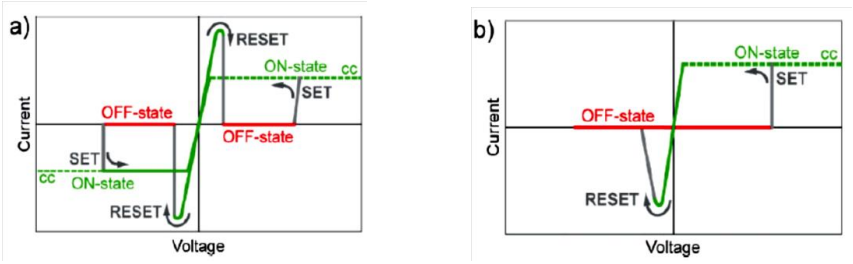

Figure 2-22: Two possible switching directions. Dashed lines indicate that the real voltage at the system will differ from the control voltage because of the compliance current (CC) in action. a) Unipolar switching. The SET voltage is always higher than the RESET voltage, and the RESET current is always higher than the CC during SET operation. b) Bipolar switching. The SET operation occurs on one polarity of the voltage or current, the RESET operation requires the opposite polarity [74].

When the switching procedure does not depend on the polarity of the voltage and current signal, switching is called unipolar (or symmetric). A system in its high-resistance state (OFF) is switched ('set') by a threshold voltage into the low-resistance state (ON) as shown in Figure 2-22-a. During the SET process, the current is typically limited by the current compliance of the control circuit. RESET into the OFF-state occurs at a higher current and a voltage below the SET voltage. When the SET to an ON-state occurs at one voltage polarity and the RESET to the OFF-state on the reversed voltage polarity, the switching operation is called bipolar (Figure 2-22-b).

After the first reports on oxide insulators by Hickmott [102] in 1962, a wide variety of materials in MIM configuration have been studied to show hysteretic resistance switching [103, 104, 105]. A new era in the research activity started in the late 1990s by Asamitsu et al. [94] Kozicki et al. [106]and Beck et al, [107]and has recently been reviewed by Waser and Aono [101]and Sawa [108]. Asamitsu et al. [94] showed that the resistivity in $Pr_{0.3}Ca_{0.7}MnO_3$ can be switched between a high and a low resistance state by the application of an electrical voltage or field. This behavior is referred to as resistive switching and shown in Figure 2-23.

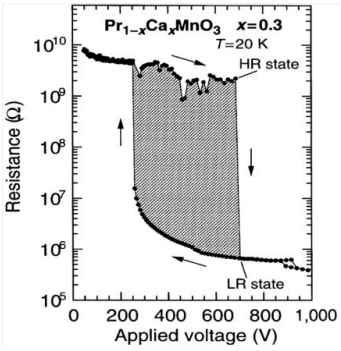

Figure 2-23: Change of resistance of a melt grown single crystal of $Pr_{0.3}Ca_{0.7}MnO_3$ at 20 K as a function of an external voltage applied. If this voltage reaches approximately 700 V (Electric field strength E≈780 kV/mm) the material switches from a high resistivity state (HR) into a more conducting one (LR). This drop in resistance amounts over three orders of magnitude. Conductivity first gradually and then abruptly changes back to the HR-state upon reducing the external electric voltage down to about 220 V (E≈245 kV/mm) [23].

In 2011 Park et al. reported [109] that phase pure but partially oxygen deficient $Pr_{0.3}Ca_{0.7}MnO_3$ based memory devices showing the effect of resistive switching may have a great potential for future non-volatile memory applications. For the origin of the phenomenon initially Asamitsu et al. supposed that an electrical current and by implication a static electric field triggers the collapse of the low temperature, electrically insulating charge-ordered state to a metallic ferromagnetic one. Meanwhile several models explaining the mechanism of resistive switching have been proposed in the literature [74, 101, 108, 110], still however it is not clear, whether the responsible effects take place in the bulk of the material or in confined regions close to the electrodes. Some authors report about the formation of highly conducting filamentary paths upon reduction growing gradually from the anode towards the cathode. Others describe that the change in resistivity is due to an interface type-conducting path (oxygen vacancy or charge carrier). Anyhow, at least for $SrTiO_3$ acceptor-doped with Cr, a titanate also showing the effect of resistive switching for which the defect chemistry is well established [10, 14, 15], the formation of oxygen vacancies seems to play an important role upon realizing the electrically well conducting state [111, 112]. For the system $RE_xCa_{1-x}MnO_3$ (RE is rare earth cation) the point defect chemistry, nevertheless, is much less acceptably understood. One reason for this lack of information relies certainly also in the complexity of this material making it difficult to assess experimentally and systematically since two cations in the quaternary oxide Mn as well as RE, such as Praseodymium, may exist in several valence states.

2.2.2 High temperature ceramic thermoelectric generators

Investigations on thermoelectric generators are becoming more important recently for solving (at least partially) today's energy challenges [113,114]. Generally, there are three well-known major effects involved in thermoelectric phenomena: the Peltier effect (a temperature difference created by applying a voltage between two electrodes connected to a sample), the Thomson effect (indicating a reversible thermal gradient and electric field in a homogeneous conductor), and the Seebeck effect. In 1821, Thomas Johann Seebeck discovered that a temperature gradient produces a voltage, which can drive an electric current in a closed circuit. This phenomenon is known as the Seebeck effect and thermoelectric generators work on its base (Figure 2-24).

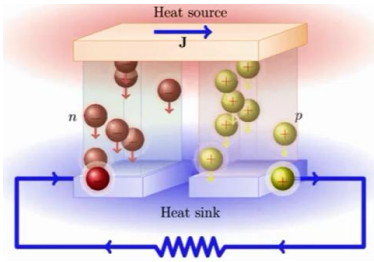

Figure 2-24: A thermoelectric circuit composed of materials of different Seebeck coefficients (*p*-type and *n*-type semiconductors), configured as a thermoelectric generator based on the Seebeck effect, defined as the formation of an electric field at an applied temperature gradient [117].

This effect can be expressed as, $V = \alpha \Delta T$, where V is thermoelectric voltage, ΔT is temperature gradient, and α is the Seebeck coefficient [115]. The Performance of a thermoelectric material can be characterized by a figure of merit defined as $ZT = S^2T/\rho\kappa$ [116] which is a function of the Seebeck coefficient S, electrical resistivity ρ, thermal conductivity κ and the mean operating temperature T.

Common high performing thermoelectric materials that may be used for the generation of electrical power out of thermal waste energy should generally have a high Seebeck coefficient and should possess as well enhanced electrical conductivity whereas thermal conductivity should be low. Since S, σ, and κ are related to each other, improving the figure of merit (ZT) is not always simple. In other words, for large Seebeck coefficient S, a low carrier concentration is needed, which makes the electrical conductivity σ smaller. On the other hand, the increase of electrical conductivity is not possible without

increasing the thermal conductivity. All of this parameters are also strongly dependent on the material's crystal structure, electronic structure and carrier concentration [115].

There are three different classes of materials, metals, semiconductors, and insulators which can be characterized by zero, small and large band gaps, respectively, or alternatively, by free-charge-carrier. Table 2-4 describes the different thermoelectric properties of these three types of materials. Large amounts doped semiconductors with carrier concentration of 10^{19} to 10^{21} carriers/cm^3 are good thermoelectric materials typically.

Table 2-4: Comparison of thermoelectric properties of metals, semiconductors and insulators at 300 K [115].

	electrical conductivity/ $\Omega^{-1}cm^{-1}$	**thermal conductivity/ k^{-1}**	**Seebeck coefficient/ μVK^{-1}**	**figure of merit Z/ K^{-1}**
Metals	very high ($\approx 10^6$)	Large	very low (≈ 5)	not very desirable $\approx 3\times10^{-6}$
Semiconductors	10^3	Low	200	$\approx 2\times10^{-3}$
Insulators	extremely low ($\approx 10^{-12}$)	Very low	large (≈ 1000)	small ($\approx 5\times10^{-17}$)

At present, the most efficient thermoelectric materials consist of intermetallic compounds containing environmentally questionable elements like Sb, Te, Bi or Pb. Additionally their use is for reasons of chemical and physical stability restricted to applications at rather low temperatures. Increasing the operation temperatures, however, offers the opportunity to improve noticeably the thermodynamic efficiency (Carnot efficiency) of thermoelectric elements. In this context, the development of semiconducting thermoelectric ceramic-based materials is discussed presently as a very promising prospect. In particular ceramics based on the perovskite phases, $SrTiO_3$ and $CaMnO_3$ are recently debated in the scientific literature [118]. Materials based on both these compounds show an interesting thermoelectric performance and can be optimized in a wide range regarding their electrical conduction behavior. The reduction of thermal conductivity, on the other hand, is believed to be tunable by realizing nanostructured morphologies in which phonon scattering is enhanced due to the introduction of internal imperfections such as solid-solid interfaces, precipitations or

lattice point defects, just to specify a few of the possibilities. “Phonon-glass-electron crystal” materials which posses both glass like phonon thermal conductivity and crystalline electrical conductivity probably have efficient thermoelectric effects [119].

In any case, however, defect chemistry plays a crucial role for electrical conduction being quite well comprehended for titanate based perovskites [10, 14, 15, 72, 74, 76, 83] lattice disorder in $CaMnO_3$ derived ceramics is far less well understood.

The oxide $CaMnO_3$ is very suitable for energy conversion. These types of materials can be used for long-time at high temperature in air. The electrical transport properties of $CaMnO_3$ and therefore its thermodynamic properties could be intensively influenced by doping and oxygen deficiency [116]; however, detailed reports in terms of electronic structure, as well as relationship between electronic structure and thermoelectric properties are currently missing.

3 Theory of electrical transport and polarization

Generally, isolated atoms are characterized by distinct energy levels of electronic states. As individual atoms approach to form a solid, the strong interactions between atoms in a crystal, causes a widening of energy levels into energy bands. Electrons fill some parts of these energy bands. The qualitative and quantitative extend of this filling defines whether a material behaves electrically as a metal, a semiconductor or as an insulator. Partially filled valence bands characterize metals: the electrons in these bands give rise to electrical conduction. On the other hand, in insulators electrons completely fill the valance bands. Finally, Semiconductors have, at low temperatures, a completely filled valance band and a narrow energy gap ≈ 1 eV (in comparison to the wide band gap > 9 eV in insulators) between valance band and the unfilled conduction band.

3.1 Metallic conductors

Metallic conductors are materials that due to the free mobility of electrons within the lattice do conduct the flow of an electric current. “Free” means here that charges can enter and leave a system in contrast to bound charges or polarization charges which can only be displaced to a lesser extent within a system [120]. The specific electrical conductivity σ is a characteristic property measured in Siemens per meter ($S \cdot m^{-1}$). Applying an electric field E provides an electric driving force $e \cdot E$, which accelerates the electrons (having a charge e) in the direction from the cathode to the anode. The drift of the electrons was modeled by Drude to be counteracted by collisions with atoms. A Newtonian-type equation (force equals mass times acceleration) of such a free electron motion model can be expressed as:

$$m\frac{dv}{dt}+\gamma v=e\cdot E \qquad \textbf{Eq. 3-1}$$

where m is the electron mass, γ is a constant which takes into account collisions between atoms and electrons (called damping strength) and v is the average drift velocity of the electrons. Conductivity can then be formulated as:

$$\sigma=\frac{N_f.e^2.\tau}{m} \qquad \textbf{Eq. 3-2}$$

where $\tau = m/\gamma$ is related to a relaxation time, i.e., the average time between two

consecutive collisions and N_f is the concentration of free electrons with respect to volume in the material.

Conductivity can also be calculated according to the following quantum mechanical equation:

$$\sigma = \frac{1}{3} e^2 v_F^2 \tau N(E_F) \qquad \textbf{Eq. 3-3}$$

where v_F is the velocity of the electrons at the Fermi energy (called the Fermi velocity) and $N(E_F)$ is the density of filled electron states, called the population density, at the Fermi energy.

The Fermi energy is the electrochemical potential of the electrons in a material and in this way it represents the averaged energy of electrons in the material. The probability that a certain energy level is occupied by electrons is given by Fermi function F(E):

$$F(E) = \frac{1}{\exp((E - E_F)/k_B T)} \qquad \textbf{Eq. 3-4}$$

This is shown in Figure 3-1 for different temperatures.

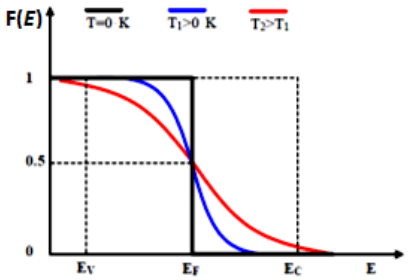

Figure 3-1: Fermi distribution function F(E), versus energy E, for different temperatures. For T = 0 K, all allowed states bellow the Fermi level are completely occupied by electrons. At T > 0 K not all states below the Fermi level are occupied and there are some states above the Fermi level that are occupied [121].

Metals contain a large number of free electrons. Therefore they have a large conductivity. In addition, in metals, with increasing temperature the number of free electrons N_f essentially does not change. Likewise, $N(E)$, i.e. the population density of the electrons near the Fermi surface changes very little [122]. However, due to an increasing rate of collisions between the drifting electrons and vibrating lattice atoms, the mean free path and relaxation time decrease with increasing temperature. As a

result, according to Eq.3-2 referring to the classical model and Eq.3-3, which describes the quantum mechanical model, conductivity σ for metals decreases with increasing temperature.

3.2 Semiconductors

Semiconductors contain generally two electron bands. The valence band is at a temperature of 0 K completely filled with valence electrons. A relatively narrow gap ≈ 1eV separates the valence band from the conduction band, which contains no electrons, at 0 K. With increasing temperature, a part of the electrons may be thermally excited across the band gap and occupy the conduction band, where they contribute to conduction. The number of electrons in the conduction band N_e increases exponentially with temperature T. This portion also depends on the size of the energy gap E_g. Therefore, it can be calculated from the equation below:

$$N_e = \frac{1}{4}\left(\frac{2m_0 k_B}{\pi\hbar^2}\right)^{3/2}\left(\frac{m_e^*}{m_0}\right)^{3/2} T^{3/2}\exp[-(\frac{E_g}{2k_B T})] \qquad \textbf{Eq. 3-5}$$

where $\frac{m_e^*}{m_0}$ presents effective mass ratio of electrons, averaged over different directions to take anisotropy into account. k_B is the Boltzmann constant. The value of the constant factor $\frac{1}{4}\left(\frac{2m_0 k_B}{\pi\hbar^2}\right)^{3/2}$ is $4.84\text{x}10^{15}$ $cm^{-3}K^{-3/2}$.

The current density, which can be expressed as $j=\sigma \cdot E$ or $j=Nve$ combined with the charge carrier mobility expression (i.e. the velocity v per unit electric field E expressed as $\mu=\frac{v}{E}$) results in a formula for conductivity:

$$\sigma = \frac{N_e v e}{E} = N_e e \mu_e \qquad \textbf{Eq. 3-6}$$

In principle, the thermal excitations of some electrons across the band gap result in the formation of electron holes in the valence band and may cause a hole current. The total conductivity in intrinsic semiconductors, i.e. pure semiconductors without impurities, is a sum of both contributions:

$$\sigma = N_e e \mu_e + N_h e \mu_h \qquad \textbf{Eq. 3-7}$$

by substituting Eq. 3-5 into the Eq. 3-7 ,the expression for conductivity can be formulated as:

$$\sigma = 4.84\text{x}10^{15}(m^*/m_0)^{3/2}\, T^{3/2}\, e(\mu_{e+}\mu_h)\exp\,[-(E_g/2k_BT)] \qquad \textbf{Eq. 3-8}$$

where the subscripts e and h stand for electrons and holes, respectively.

In the case of intrinsic semiconductor, with increasing temperature the mobility of the electronic carriers decreases due to lattice vibrations or phonon scattering ($\mu \propto T^{-3/2}$) [123]. However, the number of electrons excited from the valence band into the conduction band increases. Hence, the number of current carriers N_e and N_h strongly increases. According to Eq. 3.8, the conductivity in semiconductors, not only depends on the number of charge carriers N, but also on their mobility, whereby N is dominating [122].

On the other hand, in extrinsic semiconductors, i.e. doped semiconductors, the conduction band contains electrons or holes from two sources, the amount of which depends on temperature, (i) the doping level and (ii) electrons excited from the valence band into the conduction band in an intrinsic manner.

Electrons that have been excited from donor levels into the conduction band are free and can be accelerated in an electric field. Since in semiconductors with donor impurities negative charge carriers (electrons) represent the majority carriers, these materials are called n-type semiconductors. A similar consideration may be done with acceptor impurities, in which semiconductors are predominated by positive carriers (holes) which are introduced into the valence band. These types of materials are called p-type semiconductors.

In an intrinsic semiconductor at temperatures above 0 K the same amount of current carriers can be found in the valence as well as in the conduction band. Therefore, the Fermi energy is situated around the center of the gap. The band structure of extrinsic semiconductors is essentially the same as for intrinsic semiconductors. However, it is common to introduce the presence of the impurity atoms by the donor or acceptor levels, as shown in figure 3-2.

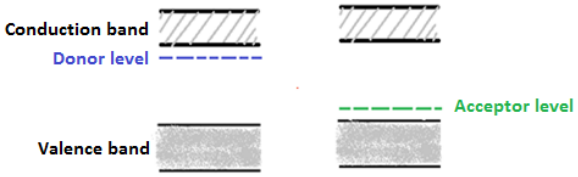

Figure 3-2: Band structure of extrinsic semiconductors, with specified donor (left side) and acceptor (right side) levels.

- **Temperature dependence of conductivity**

At a temperature of 0 K excess electrons originating from donor impurities do not contribute to electric conduction. The binding energy of donor electrons is relatively low. The distance between the donor level and the conduction band is around 0.01 eV. Therefore, an increase in thermal energy results in the dissociation of donor electrons from their nuclei and to an excitation into the conduction band. According to Eq. 3-5 the number of electrons in the conduction band increases exponentially and in the same way the amount of electrons situated in donor level is progressively reduced, until the donors are completely ionized. At higher temperatures, intrinsic effects may considerably contribute to conduction and create additional electrons. A similar consideration holds for acceptor-doped semiconductors in which acceptor levels, situated slightly above the valence edge, are progressively occupied with increasing thermal excitation, leaving behind free electron holes in the valence band. Figure 3-3 illustrates the temperature dependence of the band diagram for intrinsic and extrinsic semiconductors.

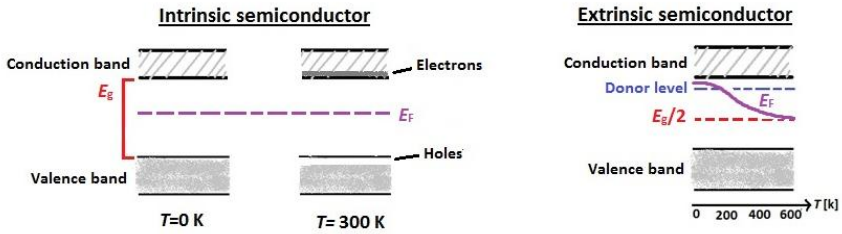

Figure 3-3: Band diagram for an intrinsic and an extrinsic semiconductor at different temperatures.

Consequently, above room temperature an increase in the number of electrons may increase conductivity σ, and on the other hand, a decrease of σ may occur due to a decrease in mobility. Furthermore, when impurity atoms are added to a semiconductor the mobility of electrons or holes also decreases slightly [122], because the concentration of charge carriers increases. For high doping levels, the mobility is low since the number of carriers is high, and therefore the temperature dependence of conductivity is less pronounced.

3.3 Insulators

3.3.1 Ionic conductors

Atoms in materials with ionic bonds, such as perovskite type oxides considered in this thesis, tend to take the noble gas configuration in order to obtain maximal stability. The ions possess very strong electrostatic binding forces, and only few free electrons are formed. Therefore, in these chemical compounds electrical conduction is usually small. Principally, in insulators only very few electrons can be excited from the valence into the conduction band due to their wide band gap. Thus, the main contribution to electrical conduction in ionic crystals is "ionic conduction". Under the influence of an electric field some negatively or positively charged ions may hop from one lattice site to another lattice site. This mechanism yields to the ionic conductivity, expressed as:

$$\sigma_{ion} = N_{ion} e \mu_{ion} \qquad \textbf{Eq. 3-9}$$

where N_{ion} is the number of ions per unit volume which can change their position by applying an electric field and μ_{ion} is the mobility of these ions.

Ions are able to move through a crystalline solid and change their positions if they have sufficient energy to pass over an energy barrier. In order to migrate to a neighboring equivalent lattice site this site must be unoccupied. Therefore, N_{ion} in Eq. 3-9 depends on the vacancy concentration in the crystal. The relationship between the mobility of the ions, in Eq. 3-9, with the diffusion coefficient D, for one unit of transported charge per atom, yields in the Einstein relation,

$$D = \mu_{ion} k_B T \qquad \textbf{Eq. 3-10}$$

According to the Arrhenius equation, the diffusion coefficient depends on temperature and can be written as:

$$D=D_0\exp(-\frac{E_a}{k_BT}) \qquad \textbf{Eq. 3-11}$$

where D_0 is a pre-exponential factor which depends on the vibrational frequency of the atoms and some structural parameters and E_a is the activation energy. An expression for ionic conductivity can be obtained by substituting the diffusion coefficient (Eqs.3.10 and 3.11) in the Eq. 3.9:

$$\sigma_{ion}=\frac{N_{ion}e^2D_0}{k_BT}\exp(-\frac{E_a}{k_BT}) \qquad \textbf{Eq. 3-12}$$

This can be simplified by inserting σ_0 as pre-exponential constant:

$$\sigma_{ion}=\sigma_0\exp(-\frac{E_a}{k_BT}) \qquad \textbf{Eq. 3-13}$$

Consequently, the ionic conduction increases exponentially with increasing temperature, similarly to semiconductors. In additions, ionic conductivity depends on the number of ions that can change their position, activation energy and on the vacancy concentration.

Eq. 3-14 can be obtained by taking the natural logarithm from both sides of Eq. 3-13:

$$\ln\sigma_{ion}=\ln\sigma_0-\left(\frac{E_a}{k_B}\right)\frac{1}{T} \qquad \textbf{Eq. 3-14}$$

where E_a and T indicate an activation energy and absolute temperature, respectively. Accordingly, the graphical representation of $\ln\sigma_{ion}$ versus 1/T results in a so called Arrhenius plot. The negative slope of the linear relationship in Arrhenius plots equals E_a/k_B and this can be utilized to calculate the activation energy of the processes under consideration. The constant σ_0 can be obtained from the intercept with the y-axis.

3.3.2 Dielectrics

Dielectrics are materials with a rather typically low density of free charge carriers. They have the ability to store electric energy when an external field is applied.

Considering two parallel metal electrodes separated by a distance L that are filled by a dielectric material under the influence of a momentary electric voltage. Electric charges can be stored even after the external voltage has been switched off. This ability is called capacitance C, with the SI unit of coulombs per volt (farad), and can be calculated as:

$$C=\frac{q}{V} \qquad \textbf{Eq. 3-15}$$

Where q and V represent charge and applied voltage, respectively.

It has been observed experimentally that the capacitance is increased with enhanced electrode area A and with reduced interelectrode spacing L. Furthermore it can be increased by introducing a material with enhanced dielectric permittivity:

$$C = \varepsilon\varepsilon_0 \frac{A}{L} \qquad \textbf{Eq. 3-16}$$

The permittivity of empty space ε_0 has a constant value of 8.85×10^{-12} F/m. The unitless material constant ε equals to C/C_{vac}, which determines the magnitude of the added storage capability compared to the vacuum case. It is called the dielectric constant or occasionally relative permittivity ε_r.

3.3.2.1 Polarization

The application of an external electric field to a dielectric material generally results in a displacement of the negatively charged atomic electron clouds with respect to the positively charged atomic nucleus. This process induces a local atomic electric dipole moment which is proportional to the displaced charge and the displacement itself. The formation of dipoles or alignment of already existing dipoles under influence of an electric field is called polarization. Charge redistribution causes dielectric material surface get the opposite charges with respect to the charge of the nearest capacitor electrode. Therefore, the orientation of the electric field created within a dielectric material is opposite to the direction of the external field. Accordingly, inserting a dielectric between two capacitor plates gradually reduces the external electric field.

Each free charge can cause dielectric displacement D (electric flux density). If an external electric field E is applied, the total charge neutrality of the material is then described by:

$$D = \varepsilon_0 E + P \qquad \textbf{Eq. 3-17}$$

The vacuum contributions to the displacement D are defined by the terms $\varepsilon_0 E$ and P, that is the induced electric dipole moment per unit volume which represents electrical polarization of the material in the system. A schematic representation of this process is shown in Figure 3-4.

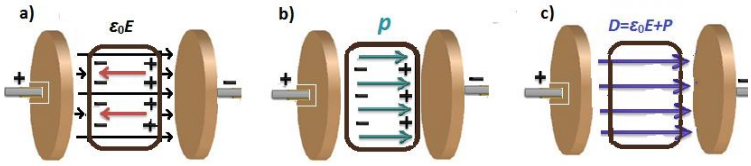

Figure 3-4: Schematic illustration of two identical electrodes applied to the opposing faces of a dielectric material: a) the vacuum contribution to the displacement *D* (the red vectors indicate electric field created within a dielectric oppositely oriented to the direction of the external electric field) b) induced dielectric polarization vector and c) the direction of the dielectric displacement *D*.

Typically, polarization can be categorized in four types [120], as shown in Figure 3-5 and summarized in table 3-1.

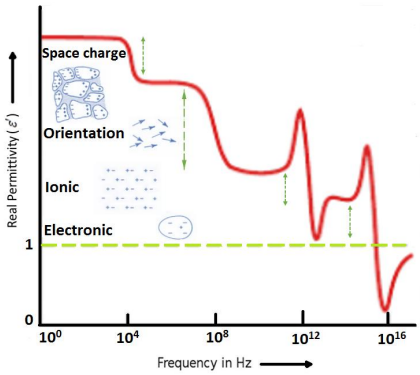

Figure 3-5: Four polarization mechanisms illustrated by the frequency dependence of permittivity [120].

Table 3-1: Polarization mechanisms with respect to relaxation time and frequency range.

Process	Relaxation time /s	Frequency / Hz
Electronic polarization	10^{-14} - 10^{-16}	10^{14} - 10^{16}
Ionic polarization	10^{-11} -10^{-13}	<10^{13}
Orientation polarization	10^{-6}	10^3Hz- 10^6Hz
Space charge polarization	<10^{-6}	10^3Hz- 10^6Hz

- **Electronic polarization:**

The already above exemplarily mentioned polarization process describes the displacement of the negatively charged atomic electron shell with respect to the positively surrounded charged nucleus. This relative tendency of charge distribution is referred to as electronic polarizability α_{el}. Larger atoms possess a correspondingly larger electronic polarizability. Generally the temperature dependence of α_{el} can be neglected because the atomic radius is usually approximately temperature independent. The electronic polarization is a relatively fast polarization process, which typically occurs between 10^{-14} and 10^{-16} s. It takes places at optical frequencies in the range from 10^{14} to 10^{16} Hz [124]. The corresponding dielectric constant contributing to electronic polarization may be determined by measuring the refractive index at optical frequencies.

- **Ionic polarization:**

Ionic polarization occurs in ionic crystals when neighboring ions of opposite charges are displaced from their equilibrium positions under an applied electric field. Generally, due to thermal expansion of the lattice the temperature dependence of ionic polarizability α_{ion} is weakly positive. Ionic polarization usually takes place for frequencies below 10^{13} Hz. This is within times of approximately 10^{-11} to 10^{-13} s which is slower than the electronic polarization but faster than space charge and orientation polarization [124], which will be described below.

- **Orientation polarization:**

Molecules are usually formed by the combination of individual atoms that covalently bound to each other by sharing some of their valence electrons. An imbalance in charge distribution because of this arrangement of electrons may cause the formation of a permanent dipole moment. In the case of the absence of an electric field, these moments are randomly oriented. By the application an external electric field *E*, however, a torque moment may act on such electric dipoles. Therefore, dipoles will rotate in order to align with the electric field direction. This process is called orientation polarization [125]. Orientation polarization hence strongly depends on temperature, because thermal movement and agitation of atoms counteract the ordering alignment. This is

described by the Langevin-function theory (Paul Langevin, 1900) [126]. The average polarizability α_{or} originating from permanent dipole moment *p* is given by [120]:

$$\langle \alpha_{or} \rangle = \frac{p^2}{3k_B T} \qquad \textbf{Eq. 3-18}$$

where *T* represents the absolute temperature and k_B the Boltzmann constant.

Generally, orientation polarization occurs in polar molecules between radio (≈10^3 Hz) and microwave (≈10^6 Hz) frequencies [124]. Electronic and ionic polarization are faster than this mechanism, but space charge polarization is slower than it.

- **Interfacial or space charge polarization:**

This type of polarization takes place in dielectric materials with spatial inhomogeneous distribution of charge carrier densities. It is important in ceramics with electrically relative well conducting grains and rather insulating grain boundaries separating them. The mechanism is referred to Maxwell-Wagner polarization. By imposing an electric field charge carriers migrate over a certain distance through the material until they are blocked at a potential barrier, such as an electrically charged grain boundary or phase boundary [127]. The migrating charges then become trapped within the environment of the respective interface, leading to a space charge polarization. Such accumulation of charges locally distorts the field, and increases the overall capacitance as well as real permittivity of a dielectric material [125, 128]. The space charge mechanism is one of the slowest polarization processes in this context. It depends on local conductivity and may occur over a wide frequency range from mHz up to MHz [120].

3.3.2.2 The complex dielectric function theory

Electric dipoles created due to polarization in a material can bind a certain portion of electric charge at the electrode interfaces of a capacitor. Polarization mechanisms allow storage of charge. The quantification of this ability to store energy is referred to as real permittivity ε'. The larger the polarization the larger the real permittivity. Since charges are displaced during polarization and because this process does not have to be static but might be dynamic ε' depends on frequency. If the external stimulating electric field oscillates, the charges move back and forth on a small scale [129]. At certain frequencies dielectric loss ε'' occurs, where a substantial amount of the excitation energy is absorbed and transformed into heat.

Moving charges cause a frequency-dependent phase shift between an applied alternating electric filed and charge displacement. The relative dielectric permittivity (Eq.3-19) and the electrical susceptibility (Eq.3-20) are therefore written as complex functions:

$$\varepsilon = \varepsilon' + i\varepsilon'' \qquad \textbf{Eq. 3-19}$$

$$\chi_e = \chi_e' + i\chi_e'' \qquad \textbf{Eq. 3-20}$$

where *i* indicates imaginary unit. The displacement of the charges is described by the real part of permittivity ε_r' and the dielectric loss is represented by the imaginary part ε_r''. The loss tangent or dissipation factor $\tan\delta$ is often used to characterize the dielectric loss of a material and is given by:

$$\tan\delta := \frac{\varepsilon''}{\varepsilon'} \qquad \textbf{Eq. 3-21}$$

In the case of orientation polarization, the conduction losses on the non-perfect dielectric $(\tan\delta)_{Conduction}$ should be added to the loss tangent of the dipole polarization $(\tan\delta)_{Dipole}$. Therefore, the sum of both contributions should be considered for the total tanδ (Eq.3-22) [120]:

$$\tan\delta = (\tan\delta)_{Dipole} + (\tan\delta)_{Conduction} \qquad \textbf{Eq. 3-22}$$

The term $(\tan\delta)_{Conduction}$ is frequency dependent. Its individual contributions can be determined experimentally.

3.3.2.3 Resistance and impedance

The terms resistance and impedance both indicate an opposition to the flow of electrons or electric current in general. The inverse of the conductivity is called resistivity *ρ*. The resistance *R* is proportional to resistivity and to the length *L* of a conducting material and is inversely proportional to its cross-sectional area *A*. It can be expressed as:

$$R = \rho\frac{L}{A} \qquad \textbf{Eq. 3-23}$$

In direct current (DC) circuits only resistors produce this effect. DC theory is a special case of alternation current (AC) theory where the frequency equals 0 Hz. Resistance is defined by Ohm's Law: $V = I R$. Potential values *V*, are measured in Volts (*V*), current value *I*, in Amperes (*A*), and resistance in Ohms (Ω). However, in AC circuits two other possible circuit elements, capacitors and inductors, influence the flow of electrons.

Impedance can be expressed as a complex number Z^*, where the resistance is the real component and where the combined capacitance or inductance form the imaginary component [130]. In the case of AC theory, where the frequency is non-zero, the analogous equation is: $V = I Z^*$.

3.3.2.4 Maxwell-Wagner relaxation

Maxwell developed the theory of dielectric properties of multiphase systems. Wagner expanded this for the case of AC, and Volger simplified it in order to be feasible for ceramic systems [128]. In both cases for external electrode-sample interfaces on a macroscopic scale or for inhomogeneous dielectric materials, such as some polycrystalline electroceramics containing highly insulating grain boundary regions separating rather conducting grains, the relaxation is defined by the Maxwell-Wagner formalism [120]**.** In either case this leads to a separation of charges. Real dielectric permittivity ε' represents the intrinsic property that each material has to maintain charges separated. The charges are often separated over a significant distance, compared to the ionic diameter, and therefore contribute to the dielectric loss ε'', which is intrinsic property that each material allows charge to move.

3.3.2.5 Relaxation time

In the case of electric circuits with alternating currents, dipoles require a certain time to reorient under a rapidly changing electric field and to align to the orientation of the external field. The corresponding characteristic time constant is called relaxation time, which critically depends on the respective mechanism and the underlying interaction forces. When an external electric field is applied dipoles in condense materials such as liquids or solids move. This leads to permanent collisions and internal friction. Therefore, molecules approach their final state of orientation after a certain relaxation time τ. This occurs gradually. The relaxation time is inversely related to the critical relaxation frequency f_c and expressed as [125]:

$$\tau = \frac{1}{\omega_c} = \frac{1}{2\pi f_c} \qquad \textbf{Eq. 3-24}$$

At low frequencies at which relaxation can fully develop, external stimulating and alternating electric fields are slow enough and hence atomic dipoles have time to align completely with the field variations. While, at higher frequencies not all polarization

mechanisms respond fast enough to fully react to the alternating external electric field. In other words, high frequency causes a phase shift between the dipole alignment and the electric field and therefore dipoles are not able to align fully.

The frequency dependence of permittivity is shown in Figure 3-6. As frequency increases the dielectric constant decreases, since dipole alignment for some of the polarization mechanism will not occur completely. Therefore, the high dielectric loss values at low frequencies (below relaxation frequency), are mainly caused by macroscopic distortion and space charge polarization. Essentially, larger polarization will result in a larger dielectric loss (Section 3.3.2.4). If the electric field oscillates too fast above the relaxation frequency, it influence the dipole rotation, and thus the orientation polarization disappears [127, 128]; therefore, both ε'' and ε' decrease as frequency increases.

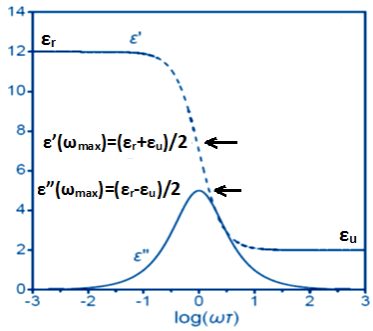

Figure 3-6: Schematic diagram of real permittivity (i.e., the ability to store energy, ε') and dielectric loss (ε'') for a material with single-relaxation-time (Debye-type).

3.3.2.6 Debye relaxation

Debye relaxation indicates a system with a single relaxation time τ, which is defined as exponential shift of the relaxation frequency with temperature [120]. The corresponding equation can be expressed as:

$$\tau = \tau_0 . e^{E_a / k_B T} \qquad \textbf{Eq. 3-25}$$

The quantities τ_0 and E_a represent the reciprocal frequency factor and the activation energy, respectively.

3.3.2.7 Poisson's equation

Poisson's equation is derived from Coulomb's law and Gauss's theorem [131]. One of Maxwell's equations is Gauss's law in differential form, expressed as:

$$\nabla \cdot D = \rho_{free} \qquad \textbf{Eq. 3-26}$$

where ∇ is the divergence operator, D indicates the electric flux density vector, and ρ_v represents the scalar function of electric volume charge density. If the substance is supposed to be homogeneous, the electric electric flux density can be formulated as:

$$D = \varepsilon E \qquad \textbf{Eq. 3-27}$$

where ε and E are the permittivity of the substance and the electric field, respectively.

Eq. 3-28 can be obtained by substituting Eq.3-27 into Eq. 3-26. It is assumed that ε is locally constant at the specified part of the substance.

$$\nabla \cdot E = \frac{\rho_v}{\varepsilon} \qquad \textbf{Eq. 3-28}$$

According to the Faraday's law of induction, in the absence of a changing magnetic field B, Eq.3-29 can be formulated, where t is time.

$$\nabla x E = -\frac{\partial B}{\partial t} = 0 \qquad \textbf{Eq. 3-29}$$

Due to the zero value for the curl of the electric field $\nabla x E = 0$, E is defined by a scalar electric potential field φ,

$$E = -\nabla \varphi \qquad \textbf{Eq. 3-30}$$

Substituting the potential gradient for the electric field in Eq.3-28 leads to the Poisson's equation, expressed as:

$$\nabla \cdot E = \nabla \cdot (-\nabla \varphi) = -\nabla^2 \varphi = \frac{\rho_v}{\varepsilon_r}$$

$$\nabla^2 \varphi = -\frac{\rho_v}{\varepsilon_r} \qquad \textbf{Eq. 3-31}$$

3.3.2.8 Ohmic contact

In order to allow electrons to flow in all directions of a semiconductor device an ohmic contact is needed. In the case of ohmic contacts as shown in Figure 3-7a the current increases linearly with increasing voltage. The corresponding I-V curves are symmetric with respect to the origin and follow Ohm's law.

If a metal is brought into contact with a n-type semiconductor, the flow of electrons depends on the work function of both the semiconductor (ϕ_S) and the metal (ϕ_M). The energy, which is necessary to transport an electron from Fermi energy to infinity, is characterized by the work function ϕ. For an ohmic contact it is necessary to use metallic electrodes with a work function lower than that of the semiconductor. As shown in figure 3-7 (b), it is assumed that $\phi_M < \phi_S$. Essentially, the electrons take the lowest possible energy. Therefore, electrons charge the metal positively by flowing from the metal into the semiconductor. The band of the semiconductor is bended "downwards" and no barrier exists for the flow of electrons in either direction (Figure 3-7c). In other words, under the influence of a positive bias in the metal part these electrons, without experiencing any barrier, flow back from the semiconductor into the metal. On the other hand, if a negative bias is applied, electrons are forced to flow from the metal to the semiconductor seeing a relatively small barrier. A similar situation exists for a p-type semiconductor and $\phi_M > \phi_S$.

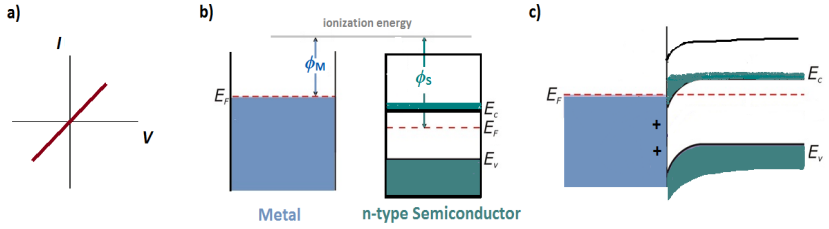

Figure 3-7: a) Current- voltage plot which follows Ohm's law, b) band diagram for metal and n-type semiconductor before contact, $\phi_M < \phi_S$, c) ohmic contact between metal and n-type semiconductor after contact.

3.3.2.9 Schottky barrier contacts

Schottky barriers may be formed through the connection of an electrode with a work function (ϕ_M) larger than the work function of a n-type semiconductor ($\phi_{n.S}$) or lower than a p-type semiconductor ($\phi_{p.S}$). In the first case, $\phi_M > \phi_{n.S}$, the Fermi energy of the metal is lower than the Fermi energy of the semiconductor. Electrons then start to flow from the semiconductor into the lowest possible energy levels in the metal until both solids reach equal Fermi energies. Therefore, the metal and thus the surface of the semiconductor will be charged negatively. The negative charge repels any free electrons

that drift toward the surface and leaves positively charged donor ions. Accordingly, the region near the surface contains a smaller number of free electrons than the interior of the crystal. Generally, this kind of region is called depletion layer or in some other cases space-charge region. Essentially, electrons assume the lowest possible energy state. Therefore, an upward curve of the electron bands near the surface is drawn to show a potential barrier for the external negative charges. As shown in Figure 3-8 and 3-8b, a potential barrier with height of $\phi_M - \chi$ is formed from the metal side, where χ is the electron affinity measured from the bottom of the conduction band into the ionization level. The height of the potential barrier from the semiconductor into the metal is $\phi_M - \phi_{n.S}$.

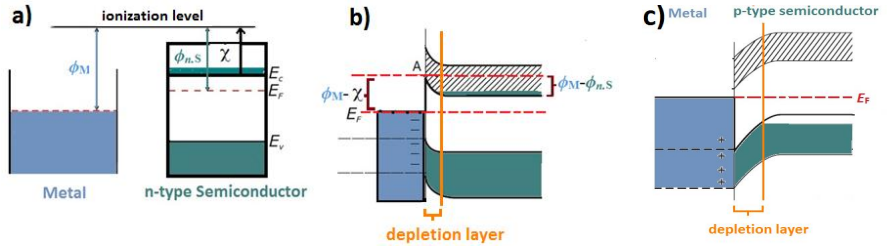

Figure 3-8: Band diagram for metal and n-type semiconductor with $\phi_M > \phi_{n.S}$, a) before contact, b) after Schottky contact, c) metal and p-type Schottky contact for $\phi_M < \phi_{p.S}$.

The conduction band of a semiconductor contains a relatively small number of free electrons. On the other hand, the metal contains more free electrons, which have to overcome a higher potential barrier than the electrons in the semiconductor. Consequently, the identical numbers of electrons diffuse in both sides across the potential barrier and produce a diffusion current in the equilibrium state. Analogously, in the case of p-type semiconductors connected with a low work function metal, i.e., $\phi_M < \phi_{p.S}$ electrons diffuse from the metal into the semiconductor. As illustrated in Figure 3-8c, since holes assume the highest possible energy state, the band edges are drawn downward and thus indicate the potential barrier for holes.

The total current across a junction is the sum of drift and diffusion components. Drift currents occur when electron-hole pairs are thermally created in or near the depletion layer. Then the electron in the conduction band is swept down the barrier and the hole in the valance band is swept up the barrier. This drift current is usually very small [122].

Diffusion currents, however, are a process by which charge carriers in a semiconductor move from a region of higher concentration into a region of lower concentration.

3.3.2.10 Brick-wall model and equivalent circuit

Impedance data analysis of dielectric materials, as they are considered in this thesis, can be performed according to the so called brick-wall model. In this model, resistive or capacitive contributions from impedance spectra can be simulated and thus extracted. Grains are assumed to have a cubic shape and identical dimensions. Furthermore, grain boundary layers of a thickness $\delta_{g.b}$ are postulated to separate all grains. The total number of grains can then be assumed to have a resistance R_{grain} and a capacitance C_{grain}. The respective contributions of the grain boundaries can be represented by $R_{g.b.\parallel}$, $C_{g.b.\parallel}$, $R_{g.b.\perp}$ and $C_{g.b.\perp}$, where the symbol ∥ denotes grain boundaries running parallel to the path of electric conduction. The symbol ⊥ indicates grain boundaries that extend in the direction perpendicular to this path. Additionally external influences such as the resistance of ceramic-electrode interfaces $R_{interface}$ and their capacitance $C_{interface}$ as well as inductive effects, represented by $L_{artifacts}$ arising from the measuring equipment and the connections to the sample have to be taken into account. The Brick-wall model for an idealized microstructure of a polycrystalline electronic ceramic and the corresponding equivalent circuit for this model are shown in Figure 3-9.

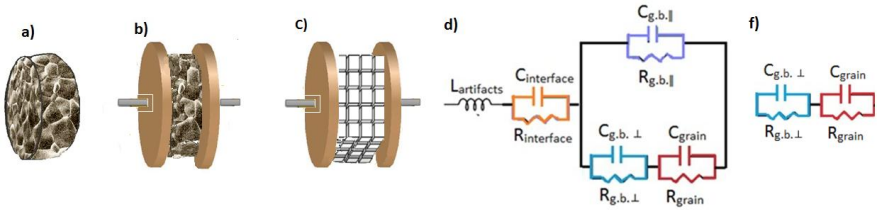

Figure 3-9: a) Ceramic pellet, b) two identical electrodes applied to the faces of a sample c) idealized brick-wall microstructure consisting of identically cubic shaped grains, d) the equivalent circuit for the brick-wall model, f) Simplified equivalent circuit.

Often the resistance value for grain boundaries running parallel to the path of electric current can be neglected, since $R_{g.b.\parallel}$ is much higher compared to $R_{g.b.\perp}$ separating two grains. It is assumed that most of the current preferentially flows through the semiconducting grains and the grain boundaries parallel to the electrode planes.

Generally, in impedance analysis, the use of low work function electrodes is preferable, since the transfer of electrons out of the metal into the ceramic is enhanced. Therefore, electrode materials with a work function as shallow as possible are needed in order to minimize the contact resistance to the ceramic layers. In the ideal case, this contact should be ohmic. In the present thesis an In-Ga alloy, which has a quite low work function of around 4 eV, has been used. The In-Ga electrodes formed an ohmic contact and showed a linear current-voltage relationship. Thus, the contact resistance and capacitance can be neglected. Under this assumption of little resistive contribution of the external interfaces, the generalized equivalent circuit given in Figure 3-9d can be further simplified as two *RC* elements; one for the grains and one for the grain boundaries perpendicular to the path of electric flow, as shown in Figure 3-9(f).

The parallel *R* and *C* connection yield in impedance Z^* for each *RC* element, which generally can be expressed as Eq.3-32. According to the Eq. 3-33, the impedance Z^* can be separated into a real Z' and imaginary Z'' part, containing the imaginary unit represented by $j=\sqrt{-1}$ and angular frequency $\omega=2\pi f$.

$$\frac{1}{Z^*}=\frac{1}{R}+j\omega C \longrightarrow Z^* = \frac{R}{1+j\omega RC} \qquad \textbf{Eq. 3-32}$$

$$|Z^*| = \sqrt{Z'^2 + Z''^2} \begin{cases} Z' = \dfrac{R}{1+(\omega RC)^2} \\ Z'' = \dfrac{-\omega R^2 C}{1+(\omega RC)^2} \end{cases} \qquad \textbf{Eq. 3-33}$$

The impedance of grains and grain boundaries (g.b⊥) can be calculated separately according to the equations above. Consequently, the total impedance Z^*_T can be written as:

$$Z^*_T = Z^*_{grain} + Z^*_{g.b.\perp} = (Z'_{grain} + Z''_{g.b.\perp}) + j(Z''_{grain} + Z''_{g.b.\perp}) \qquad \textbf{Eq. 3-34}$$

To evaluate electrochemical impedance data, Z^*_T is plotted in the complex plane with minus the imaginary part against the real part which is known as Nyquist plot or complex impedance plane plot. Each point on the Nyquist plot represents the

impedance at specific frequency. Apparent response to Z_T^* is often a combination of two or more semicircles (locii) that describe the contribution of different elements such as grain and grain boundaries with different relaxation frequencies. Each semicircle can be fully observed on the impedance diagram only if the relaxation frequency that ascribes each semicircle differs at least by two or three orders of magnitude otherwise semicircles present some degree of overlapping, based on a response very close at similar frequencies. This overlapping increases with decreasing magnitude of the difference between the individual relaxation time values [132]. The maximum value of the imaginary part of the total impedance Z_T^* is obtained for the case of relaxation, where the reciprocal angular frequency of the exciting electrical field just corresponds to the relaxation time τ of the circuit:

$$\tau = RC = (\rho \frac{d}{A})(\varepsilon_0 \varepsilon_r \frac{A}{d}) = \rho \varepsilon_0 \varepsilon_r \qquad \textbf{Eq. 3-35}$$

where A represents the cross-sectional area, d the distance between the two electrodes and ε_0 vacuum permittivity. Therefore, the relaxation time only depends on the product of the materials resistivity ρ and relative dielectric permittivity (dielectric constant) ε_r, which is separated into a real and an imaginary part as expressed in Eq. 3-36 and Eq. 3-37 respectively.

$$\varepsilon_r' = \frac{Z''}{\omega C_0 |Z|^2} \qquad \textbf{Eq. 3-36}$$

$$\varepsilon_r'' = \frac{Z'}{\omega C_0 |Z|^2} \qquad \textbf{Eq. 3-37}$$

Modern computer controlled impedance analyzer systems calculate automatically the dielectric constant ε' (relative permittivity) by the ratio of measured capacitance C and C_0. The geometrical capacitance C_0, is given by the vacuum permittivity ε_0.

Complex impedance analysis allows modeling of the compounds in terms of an electrical equivalent circuit. In the present thesis, the circuit with two, three, and four *RC*-elements [*R*1|*C*1+*R*2|*C*2+*R*3|*C*3+*R*4|*C*4] was used for the evaluation of all impedance spectra by complex nonlinear least squares fitting (WinFit-Software, Novocontrol). *R* and *C* indicate resistance and capacitance. Depending on the temperature the best fit has been chosen. Typically, components at low frequencies indicate grain boundary

contributions to the electric response and the specific properties of the grain or bulk are represented at high frequencies. Figure 3-10 demonstrates that experimental data are describe and fit well with four series of parallel *RC* circuit elements. Values of resistance, *R* and capacitance *C* can be derived for the grain and grain boundary according to the suitable electrical equivalent circuits.

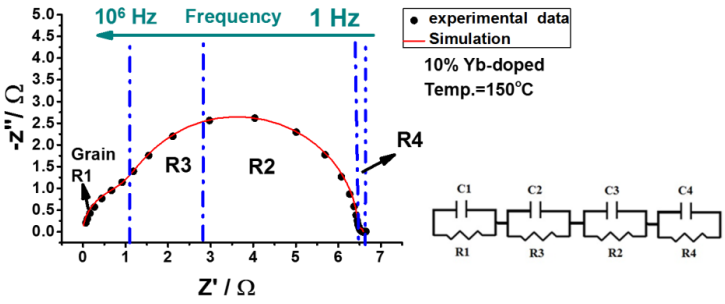

Figure 3-10: Complex impedance diagram obtained experimentally for 10 at. % Yb-doped (symbols), in which the negative imaginary part *Z″* is plotted against the real part *Z′* within the frequency range of 1 Hz to 1 MHz at 150°C. Theoretical curve (solid line) calculated based on the respective equivalent circuit using WinFit-Software, Novocontrol. Four series of parallel *RC* circuit elements are in excellent agreement with experimental data.

In some cases, in particular for polycrystalline ceramics, capacitance *C* is not ideal which means different relaxation times are present that lead to a depression phenomenon of the corresponding semicircle. To model the electrical response a phase constant element can be used by replacing *RQ* circuit instead *RC* circuit. *Q* indicates non-ideal capacitance which is physically determined by two parameters: Y_o with exponent *n* (*n*<1). Y_o tends to an ideal capacitance *C*, when the exponent *n* tends to a value of 1 and is expressed as [133,134]:

$$C_i = R_i^{(1-n_i/n_i)} Y_{oi}^{(1/n_i)} \qquad \textbf{Eq. 3-38}$$

In the present dissertation, however, a small depression of the semicircle is observed for all the investigated compounds, using *RQ* circuit did not fit well the experimental data. All the measurements were fit well with equivalent electrical circuits, i.e. the *RC* circuit in serie combination of electrical resistor in parallel with a capacitor.

4 Experimental

The system $Yb_xCa_{1-x}MnO_3$ is considered in the present thesis. The standard synthesis method known as solid state reaction was applied for the preparation of ceramic powders, which consists of the intense blending and milling of mixed oxides and carbonates by ball milling followed by calcination treatments, at elevated temperatures for phase formation. This method is environmentally friendly as the product is synthesized directly from metal oxides without releasing toxic gases. Regarding the preparation of ceramic bodies, the following issues were studied systematically:

(i) the result of changes in the partial pressure of oxygen $p(O_2)$ and / or in temperature T during the calcination and sintering processes for both pure and Yb-doped $CaMnO_3$,

(ii) the effect of the doping or substitution level x (The concentration of the Yb-addition was varied from 0.1 to 10 at.-%),

(iii) the consequences of cationic nonstoichiometry (Ca-excess and Mn-excess).

These powders were intensively characterized with respect to the particle size distribution (Laser scattering), phase purity (XRD diffraction), crystallographic parameters (XRD in combination with Rietveld refinements), microstructure inspection by electron microscopy (SEM), Energy-dispersive X-ray spectroscopy (EDX) regarding the grain size and morphology of eventual foreign phases and sintering activity (Dilatometry of compressed green bodies). In addition, Iodometric titration and Thermogravimetric analysis (TGA) were used to quantify the average valence of Mn-cations and oxygen-deficiency. With this whole range of polycrystalline materials the effect of internal interfaces were studied systematically. The main focus, however, was devoted to electrical measurements of the electrical DC-conductivity at different temperatures T and in oxidizing as well as in reducing ambient of different oxygen concentrations $p(O_2)$. In order to understand the role of bulk conductivity contributions and the effect of internal interfaces (grain boundaries) these studies were conducted by impedance spectroscopic measurements of the electrical complex AC-resistivity.

4.1 Materials synthesis and ceramic processing

4.1.1 Powder preparation and calcination process

The synthesis of bulk perovskite oxide has been conducted by environmentally friendly solid state reaction method. Figure 4-1 shows the summary of ceramic preparation process.

Figure 4-1: The process of ceramic preparation.

The first step consists of the preparation of an aqueous $Yb_xCa_{1-x}MnO_3$ suspension. MnO_2 (Manganese (IV) oxide, 99.9%-Chempur-Germany) and $CaCO_3$ (Calcium carbonate, 99.9% - Chempur- Germany) were blended with isopropanol in a polyethylene bottle. A half of the volume of bottle was filled with zirconia balls (YTZ, Japan) of 2 and 3 mm in diameter. The resulting slurry was mixed by roller bench, and then concentrated by evaporation in a rotary evaporator (Rotavapor R-134 with water bath B-480, Buchi, Switzerland) until a spongy solid was obtained. The spongy solid was ground by hand with an agate mortar. Isopropanol was added and the mixture was ball milled for 12 hours and concentrated again. After measuring the particle size distribution by laser light scattering (Mastersizer, Malvern, UK), the fine powders were calcined typically at temperatures between 1000-1200 °C in 20% O_2 + 80% Ar and/or 100% oxygen in a tube furnace (Thermal technology GmbH- Germany).

4.1.2 Ceramic preparation and sintering process

The calcined powder were mixed with 3 wt. % of polyvinyl acetate (PVAc) as a binder. These powders were then pelletized by cold uniaxial pressing, applying a pressure of 184 MPa in a cylindrical steel die (diameter: 10-14 mm) that contained the powder. After compaction the green bodies were further compacted with a cold isostatic press

(Paul-Otto Weber, KIP40ES, Germany) in pressure of 40 MPa for 30 minutes. In order to remove the binder, decarbonisation at 600°C was performed by using a muffle furnace (HT L9\SH, Nabertherm, Germany). These pellets were then sintered at 1350°C in a gas-tight Al_2O_3 tube furnace using various gas compositions.

All ceramic compositions as well as their calcination and sintering conditions studied in the present thesis are summarized in tables 4-1. The density of pellets, determined by Archimedes method, was more than 98% except samples sintered in pure Ar with 90% density.

Table 4-1: Ceramics compounds, calcination and sintering conditions studied in the present thesis.

Symbol	composition	Calcination and sintering conditions
B1 B2 B3 B4	$CaMnO_3$ (different calcination conditions)	Calcination Temperature: • 1000 - 1200°C Calcination Atmosphere: • 20% O_2+Ar • 100% O_2 Sintering Temperature: • 1350°C Gas composition during sintering: • 100% O_2 • 20% O_2+80% Ar • 1% O_2+ 99%Ar • 100% Ar
F	$Ca_{1.01}MnO_3$	
W	$CaMn_{1.01}O_3$	
Yb-0.1%	$Yb_{0.001}Ca_{0.999}MnO_3$	
Yb-0.5%	$Yb_{0.005}Ca_{0.995}MnO_3$	
Yb-1%	$Yb_{0.01}Ca_{0.99}MnO_3$	
Yb-5%	$Yb_{0.05}Ca_{0.95}MnO_3$	
Yb-10%	$Yb_{0.1}Ca_{0.9}MnO_3$	

The sintered pellets with a diameter of 10-12 mm were cut with a diamond saw and grinded with SiC sandpaper and diamond suspensions (6-1 µm).

4.2 Crystallographic, microstructural, and analytical characterization

4.2.1 Particle size distribution (Laser scattering)

The determination of the particle size distribution is one of the most important parameters involved in powder characterization. It influences the physical and chemical properties of materials, such as reactivity of solids participating in chemical reactions. Generally, smaller particle size may lead to the presence of smaller grain size in ceramics after solidification. Therefore, particle size distribution needs to be controlled in many industrial products such as the manufacturing of ceramics.

In the present thesis, laser light scattering (Mastersizer, Malvern, UK) was used to assess the size of particles in the range from 0.1 to 50 µm. A very small amount of powder is added to an aqueous solution with a dispersant, which consists of distilled water mixed with tetra-sodium diphosphate decahydrate powder, $Na_4P_2O_7x10H_2O$ (1g/l). An optical instrument records the spectrum of the light scattered from the prepared sample. A part of the instrument includes a series of individual detectors. Each collects scattered light at a certain angle. One recording collected on the detectors shows the spectrum of scattered light when particles pass through the laser beam over a certain period of time. When the measurement is completed, a software using defined optical parameters, analyzes the data and calculates the diameter of the particles expressed in microns.

4.2.2 X-ray diffraction

X-ray diffraction (XRD) measurement is a non-contact and non-destructive characterization method. This method identifies the crystal structure that can be confirmed by comparing with the standard database of powder diffraction file (ICDD data base PDF card). Bragg's law is the basis for the XRD analysis. According to this law, a crystal has parallel planes of atoms separated by distance d_{hkl} labeled by Miller indices (hkl). When a beam of X-ray is incident on the sample, with the wavelength λ and the angle θ, X-rays are scattered by each atom or ion. If the Braggs' law is satisfied for a periodic crystal structure, the radiation diffracted from successive planes interfere constructively (Figure 4-2). It can be expressed as:

$$2d_{hkl}.\sin\theta_{hkl} = n\lambda \qquad \textbf{Eq. 4-1}$$

where n is an integer. For certain θ value, the reflection from all parallel planes gives a strongly diffracted beam, presented as a Bragg peak in XRD pattern. The position and intensities of characteristic peaks are related to the crystal structure.

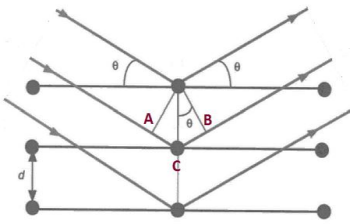

$$\overline{AC} = d\sin\theta$$

$$\overline{ACB} = 2d\sin\theta$$

$$n\lambda = \overline{ACB}$$

Figure 4-2: Braggs' law for a periodic crystal structure. The constructive interference of the radiation diffracted from successive crystallographic planes, separated by distance d [135].

Doped and undoped calcium manganite powder was characterized by means of X-ray diffraction (XRD) which presents information about phase purity and crystallographic characterization. A small amount of the powder was pressed between two sample's supports (Mylar Polyester film), and then fixed on the circle holder. The source and detector with its associated optics lie on the circumference of focusing circle and the sample stage at the center of the circle. The measurement performed using a diffractometer (Huber Imaging Plate Guinier Camera G670, Germany) equipped with CuK-radiation, λ= 1.540590 in Transmission Geometry, scanning 8 loops, which results the detected X-ray intensity as a function of the doubled incident angle (2θ) range with respect to crystal planes of the investigated sample. To determine the lattice parameters, and identify the deviation from the ideal structure Rietveld refinement of the XRD pattern has been done using FullProf software package (CEA-CNRS, France). In some cases, to get the best statistics results for the Rietveld refinement, longer measurement times were considered using the STOE diffractometer (STOE STADI P Transmission, RÖNTGENLABOR, Reinheim, Germany).

4.2.3 Scanning electron microscopy (SEM)

SEM is a type of electron microscope that produces images of a sample by scanning it with a focused beam of high-energy electrons. The electrons interact with atoms in the sample and generate a variety of signals at the surface of solid specimens. The signals that derive from electron-sample interactions contain information about the surface

topography of the specimen. In the present thesis a HITACHI SEM (model SU8000, Japan) was used. A small amount of powder was directly deposited on a piece of sticky carbon tape that could be mounted on a sample holder. A special cylindrical holder with a hole in the center to hold ceramic pellets was used for microstructural analysis. Samples were kept in a high vacuum chamber and an electron acceleration voltage of 3 kV was applied.

4.2.4 Energy-dispersive X-ray spectroscopy (EDX)

This technique depends on the interaction of the X-ray excitation source and a sample. Every element shows distinctive peak sets within X-ray spectrum due to its distinct electronic structure of atoms or ions. The maximum energy of the X-ray is limited by the maximum energetic electrons (20-40 Kev normally). Therefore, this method can be used for chemical characterization and elemental analysis of certain samples (Figure 4-3). Initial EDX analysis usually involves the emitting of an X-ray spectrum from the entire scan area of the SEM. It is also possible to have a spot measurement by keeping the electron beam stationary on a spot or series of spots and generate spectra that will provide more localized elemental information [136, 137]. One or more maps are recorded simultaneously using image brightness intensity as a function of the local relative concentration of the elements present.

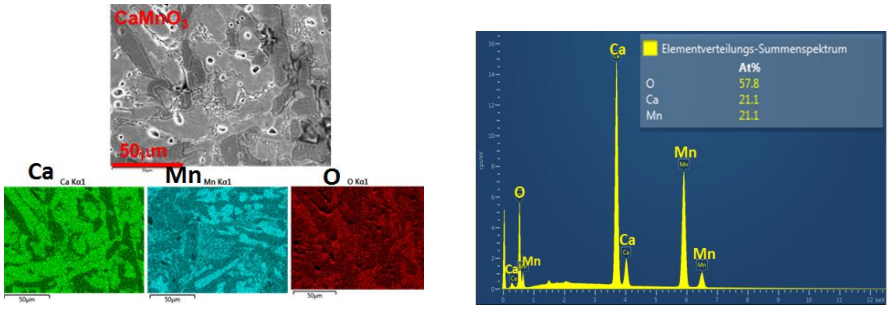

Figure 4-3: EDX spectrum of a thermally etched calcium manganite ceramic (right side). Calcination at 20%O_2 and 1200°C, dilatometry at 100% Ar; and elemental mapping (left side): bright colors indicate local concentration of the specific element and dark colors represent the lack of that element.

4.2.5 Raman Spectroscopy

Raman spectroscopy is a spectroscopic technique based on inelastic scattering of monochromatic light, usually from a laser source, and analyzes chemical composition and structure of materials. Inelastic scattering means that the frequency of photons in monochromatic laser light changes upon interaction with a sample. This shift provides information about vibrational, rotational and other low frequency transitions in molecules or crystallographic structures. Raman spectroscopy can therefore be used to study solid, liquid and gaseous samples. Upon interaction of a laser beam with a sample a electric dipole moment maybe $p = \alpha E$ induced and the molecules or crystallographic unit in locally deformed; where α and E are polarizability and electric field, respectively. Molecules start vibrating with characteristic frequency υ_1, due to periodical deformation. The amplitude of vibration is called a nuclear displacement. In other words, monochromatic laser light with frequency υ_0 excites molecules and transforms them into oscillating dipoles. Such oscillating dipoles may emit light of three different frequencies (Figure 4-4): Rayleigh scattering, Stokes, and Anti-Stokes frequency [138, 139].

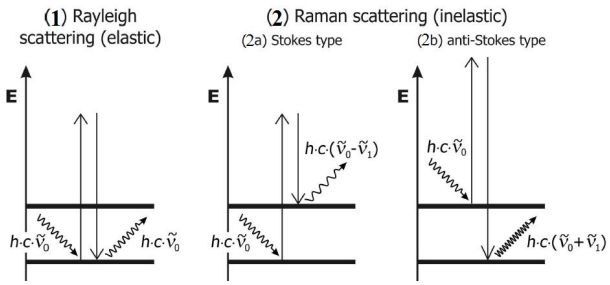

Figure 4-4: Clarification of the light-molecule interaction using a simplified energy level diagram [138].

Figure 4-4 (1), demonstrates “Rayleigh scattering”. A molecule with no Raman-active modes absorbs a photon with the frequency υ_0. The excited molecule returns back to the same basic vibrational state and emits light with the same frequency υ_0 as an excitation source. “Stokes frequency” is shown in Figure 4-4 (2a). A photon with frequency υ_0 is absorbed by Raman-active molecule which at the time of interaction is in the basic vibrational state. Part of the photon’s energy is transferred to the Raman-

active mode with frequency υ_1 and the resulting frequency of scattered light is reduced to $\upsilon_0 - \upsilon_1$. In "Anti-Stokes" frequency (Figure 4-4 (2b)), a photon with frequency υ_0 is absorbed by a Raman-active molecule which at the time of interaction is already in the excited vibrational state. Excessive energy of excited Raman active mode is released and then molecule returns to the basic vibrational state and the resulting frequency of scattered light goes up to $\upsilon_0 + \upsilon_1$.

In the present thesis, Raman measurements were performed with 488 nm excitation (Argon ion laser, Coherent), using confocal Raman spectrometer T64000 (Horiba Jobin Yvon) equipped with 1800 grooves/mm grating and a CCD camera cooled to -128°C. The laser beam was focused with a 50x objective lens (NA 0.75). The laser power at the sample was 5.5±0.5 mW. The exposure time was 120 s with 30 repetitions.

4.2.6 Dilatometry

Dilatometry is a thermoanalytical technique used to measure the expansion or shrinkage of solids, powders, pastes and liquids under negligible load when subjected to a controlled temperature/time program. A precise understanding of this behavior can provide insight into the firing processes, the influence of additives and raw materials, densification and sintering properties, reaction kinetics, phase transitions, and thermal shock. Figure 4-5 shows Horizontal Pushrod Dilatometer.

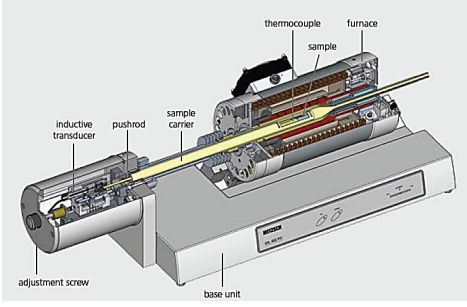

Figure 4-5: Horizontal Pushrod Dilatometer of the ceramic [140].

Wide temperature range, easy handling, high accuracy, homogeneous temperature profile, flexible sample geometry, and low risk of contamination are advantages of this instrument.

- **Method and Principle of Operation**

The powdered component are pressed into pellets and then heated to high temperatures for extended times. This process causes the surface ions to diffuse into the empty spaces between the particles. Concomitantly, vacancies diffuse into the grain boundaries and are annihilated there. Therefore, the pores eventually close up and the pellet shrinks, and becomes dense [141].

In Pushrod dilatometry the sample go through a controlled temperature program to determine dimensional changes versus temperature or time. The material's coefficient of expansion (α) is the degree of expansion divided by the change in temperature.

$$\alpha = \frac{1}{L_0}(\Delta L/\Delta T) \qquad \textbf{Eq. 4-1}$$

In which α, L_0, ΔT and ΔL indicate the coefficient of expansion, the initial sample length, the change in temperature and change in length, respectively. To perform a dilatometry analysis, a sample is inserted into a special holder within a movable furnace. A pushrod is positioned directly against the sample and transmits the length change to a linear variable displacement transducer (LVDT). As the sample length changes during the temperature program, the LVDT core is moved and an output signal proportional to the displacement is recorded. The temperature program is controlled using a thermocouple located either next to the heating element of the furnace or next to the sample.

In the present research, dilatometry (DIL.) analysis was performed to investigate the shrinkage behavior of the pellets (DIL402C, Netzsch, Germany).The applied temperature profile was from 25°C to 1400°C and held for 6 hours with a heating and cooling rate of 5K/min. DIL was carried out in four different gas compositions: 100% O_2, 20% O_2 + 80% Ar, 1% + 99% Ar and 100% Argon. The gas composition was kept constant during the experimental series.

Additionally during the dilatometry measurements in pure argon the release of O_2-gas was monitored by ZrO_2 oxygen sensor, simultaneously. The argon flow must be open in whole measurements, otherwise the driving force at the end of experiment would be very small which results in undesirable oxidation. This analysis can detect the altered number of oxygen vacancy concentration present in the sample with respect to the temperature from 25 to 1400 °C. It shows at which temperature a sample starts losing

oxygen. The amount of oxygen released can be calculated by the Nernst formula, which is derived from standard changes in the Gibbs free energy, accompanied with electrochemical transformations. The cell reaction is the transfer of oxygen from one side to the other. Using the Kröger-Vink notation for point defects this can be written as [142]:

$$O_O \rightleftharpoons 1/2O_2(g) + V_O^{\bullet\bullet} + 2e' \qquad \textbf{Eq. 4-2}$$

The electrochemical potential E associated with electrochemical reactions is defined as the decrease in Gibbs free energy per Coulomb of charge transfer, expressed as $\Delta G = -zFE$. In standard conditions, it is formulated as $\Delta G^0 = -zFE^0$, where F indicates Faraday constant which is unit conversion factor ($F=N_A q$ where N_A is Avogadro's number and q presents fundamental electron charge) and z denotes the number of electrons transferred in the reaction. According to thermodynamics the actual free energy ΔG is related to the energy change under standard conditions ΔG^0 by the $\Delta G = \Delta G^0 + RT\ln Q$, where Q is the reaction quotient. In chemistry, a reaction quotient is a function of product divided by reactant. In the special case where the reaction is in equilibrium the reaction quotient is constant and equal to a equilibrium constant that appears in the expression of the law of mass action [143]. Therefore, the equation below can be formulated.

$$-zFE = -zFE^0 + RT\ln Q \qquad \textbf{Eq. 4-3}$$

In the case of an electrochemical equilibrium, dividing both sides of the formula by (-zF) leads to a Nernst equation expressed as:

$$E = E^0 - \frac{RT}{zF}\ln\frac{p(O_2)_{Exhaust}}{p(O_2)_{Reference}} \qquad \textbf{Eq. 4-4}$$

Where $p(O_2)_{Reference}$ in the present dissertation refers to a constant flow of air $p(O_2)$ = 0.2064 bar. Accordingly, $p(O_2)_{Exhaust}$ can be formulated as:

$$p(O_2)[\text{bar}] = 0.2064 \cdot \exp(-46.42\frac{U_N[\text{mV}]}{T[\text{K}]}) \qquad \textbf{Eq. 4-5}$$

where U_N indicates the Nernst voltage and T represents the temperature in Kelvin.

4.2.7 Thermogravimetric analysis (TGA)

The TGA technique (NETZSCH TG 439-Germany) is used to characterize materials (grinded powder) that exhibit mass loss due to loss of volatiles, decomposition and

oxidation. This instrument measures the amount and rate of change in the mass of a sample as a function of temperature and time in a controlled atmosphere.

4.2.8 Quantification of Oxygen-deficiency by iodometric titration

The resistivity of manganite depends on several factors including the valence states of Mn cations and oxygen non-stoichiometry [22]. The oxidation state of B-site metal cation can be titrated by the so called iodometric method. According to the principle of electroneutrality, the relationship between the number of oxygen vacancy generated and the oxidation state of B-site metal cation can be defined in theory. Some essential definitions are collected in table 4-2.

Table 4-2: List of terms and definitions for the titration method [144]:

Titrant	It is a solution of known concentration which is added (titrated) from a burette to a measured quantity of another solution to determine the concentration of a second chemical species. Synonyms: titrator, the reagent, or the standard solution. In the present thesis $Na_2S_2O_3$ solution is used as a titrant.
Titration	Quantitative chemical analysis. The amount of titrant is determined which reacts quantitatively with the sample compound to be analyzed. From this volume (titrant consumption) the amount of sample compound is calculated. The calculation is based on the stoichiometry of the assay reaction. Synonyms: volumetry, titrimetry.
Indication	Procedure to follow the reaction and to detect the end of the titration, e.g. potentiometry (electrodes), or use of color indicators (e.g. starch).
End of titration	The titrant is added until the end of the reaction is observed, e.g. by a color change of an indicator.
Analyte	Specific chemical species of which the content in the sample can be determined by titration.
Stoichiometry	Mole/mass relationships between reagents and products. The reagents always react according to fixed relationships.

Titration is based on a complete chemical reaction between the analyte and a reagent (titrant) of known concentration which is added to the sample. In order to be suitable for a determination the end of the titration reaction has to be observable easily. Potential measurement with a sensor (Potentiometry) or color indicators are appropriate techniques to indicate reaction. Based on the stoichiometry of the chemical reaction, the analyte content is calculated by the measurement of the distributed titrant volume. The reaction involved in a titration must be fast, complete, unambiguous and observable [144]. According to the indication principles and chemical reactions occurring, titrations can be classified in to: Acid-base, Redox, Gas phase,

Complexometric, Zeta potential and Assay titration. In the present thesis redox titration has been performed. The redox titration endpoint is determined by the first iodine excess that is complexed with starch, giving a deep blue-violet color [145].

4.2.8.1 Specific detection for stoichiometric and Yb-doped $CaMnO_3$

Since in direct titration for $CaMnO_3$ the end-point is very difficult to observe, back titration was used in the present thesis. 20 mg $CaMnO_3$ with excess of Potassium iodide (KI) was mixed with degassed and purified HCl in a glass ampoule. The glass ampoule was sealed. Heating the mixture leads to the dissolution of $CaMnO_3$, and afterwards Iodine (I_2) was liberated by the following reaction.

$$Mn^{\alpha+} + (\alpha-2)I^- \rightarrow Mn^{2+} + 1/2(\alpha-2)I_2$$

$$1/2(\alpha-2)I_2 + (\alpha-2)S_2O_3^{2-} \rightarrow (\alpha-2)I^- + 1/2(\alpha-2)S_4O_3^{2-} \qquad \textbf{Eq. 4-6}$$

The solution was titrated in Ar with a $Na_2S_2O_3$ solution using starch as an indicator. The titrant ($Na_2S_2O_3$) is added until the end of the reaction is observed (colorless solution). The precise volume of the used $Na_2S_2O_3$ was noted. Several measurements for each compound were carried out and the average of the results was used for determining the average Mn valency and corresponding oxygen content of the sample.

4.3 Electrical characterization

4.3.1 Complex impedance spectroscopy

This type of characterization applied to ceramics allows an understanding the different electronic and ionic contributions of conductivity arising from the bulk and from internal and external interfaces. The electrochemical behavior of electrodes and/or electrolyte materials is usually evaluated with cells having two identical electrodes applied to the faces of a sample in the form of a circular or rectangular coating. Theory was described in chapter 3. Here practical aspects of the measurements were discussed. In the present study dielectric properties of $Yb_xCa_{1-x}MnO_3$ (0 to 10% concentration of Yb-dopant) were investigated. Measurements were taken from -100 to 300°C in 25°C steps at a heating rate equal to 1.0 K min^{-1}, in the frequency range of 1 Hz to 1 MHz. To obtain clear information about the transport and dielectric properties of these materials, an impedance analyzer (Alpha analyzer, Novocontrol System GmbH, Germany) was used. This system is based on the alternating-current (AC) dielectric method. An AC voltage

amplitude of 0.1 *V* was applied to the sample and the impedances at different frequencies were recorded automatically. An electrode diameter of ϕ = 9 mm and a sample thickness d = 2 mm were typically selected. Before each measurement and before applying electrodes both sides of the pellets were polished in order to remove eventual resistive outer surface layers.

For such electrical measurements, the selection of the electrode material is crucial with respect to the investigated temperature and the type of conductivity. Often applied electrodes consist of platinum, palladium, gold, indium-gallium (In-Ga) or silver. At high temperatures (*T* > 600°C) platinum and gold electrodes can be used, but at temperatures below 600°C they are relatively blocking to oxygen [146]. If the measurement temperature is lower than this, silver and In-Ga (T < 300°C [147]) electrodes are preferable, as they generally have lower electrode impedances. In the present thesis, in order to form ohmic contact and minimize the contact resistance to the $CaMnO_3$ ceramic layer (work function: 4.8-5.3 eV [148, 149]) In-Ga alloy with work function of 4.1-4.2 eV was selected as an electrode. Liquide In-Ga electrodes which are brushed on both sides of the polished ceramic are quick and easy to assemble.

A schematic of the representation impedance analyzer used is shown in figure 4-6.

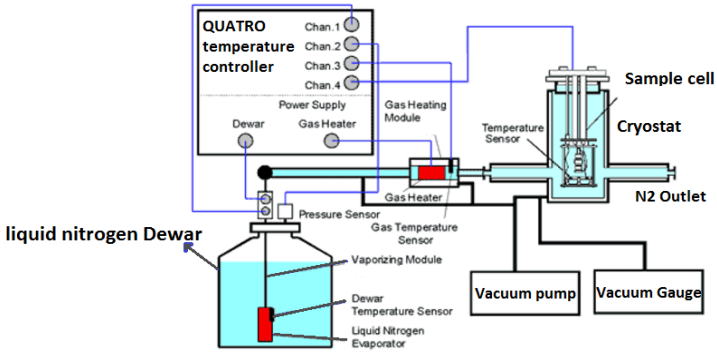

Figure 4-6: Schematic representation of the impedance analyzer used [150].

After using suitable electrodes, the sample was mounted between two brass (Cu-Zn alloy) plates and placed inside a vacuum isolated heatable cryostat recipient. The atmosphere surrounding the ceramic sample during data acquisition consists of dry N_2, which is supplied by a Dewar flask with liquid N_2. Impedance values can be measured

within the limits from 10^{-3} to 10^{15} Ω with 0.1% of accuracy. To create a cold gas stream cold nitrogen gas is evaporated from nitrogen Dewar. After that, it is heated by an additional gas heater to adjust the sample temperature. The sample temperature range can be from -160 to 400 °C. Depending on the sample temperature setpoint, the heating element of the evaporator module builds up a specified pressure in the liquid nitrogen Dewar and hence creates a constant flow of cold nitrogen gas within the gas heater module. The pressure and temperature in the Dewar are measured by two channels of a QUATRO controller. In order to keep the measurement conditions constant, the sample is placed in the Cryostat connected to the vacuum pump.

4.3.2 DC-conductivity measurement

In order to measure the ceramic resistivity, in the present thesis, the four-point probe method was applied. As illustrated in Figure 4-7, two inner wires (Pt-probes) separated by a distance of typically 5 mm sense the voltage *V* and two other probes carry the current *I*.

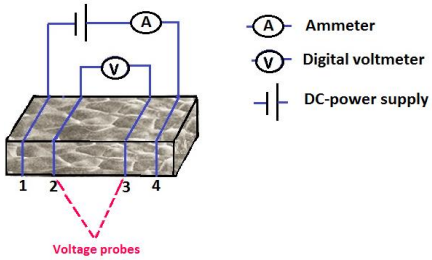

Figure 4-7: Schematic representation of the four point probe method for DC-measurement.

Polished ceramic samples with dimensions 4 x 0.7 × 10 mm^3 were firmly connected to a voltmeter (PM2534, Philips, The Netherlands) and a current source (6220, Keithley, USA) by using 100 µm Pt wires. To hold the wrapped wire on the sample four small slits are cut into the sample on each side using a diamond wire saw. The points of contact were sputtered as Pt-electrode through a shadow mask in order to reduce the contact resistance in comparison to the resistance of the sample. Therefore the contact resistance can be ignored in the further evaluation. A potential drop (voltage) shows that the sample has resistance to the flow of electrical current. The resistance of the sample between probes 2 and 3 is the ratio of the voltage measured by a digital

voltmeter to the value of the output current of the power supply. Hence, the resistivity of the ceramic sample was calculated according to the Eq.4-4.

$$\rho = \frac{V}{I} \cdot \frac{A}{d} \qquad \textbf{Eq. 4-7}$$

where A denotes the cross area, and d represents the distance between the voltage sensing electrodes. The ceramic samples were fixed in a gas-tight quartz tube. A schematic image of the DC-conductivity measurement system is illustrated in Figure 4-8. A variable gas mixture stream of defined $p(O_2)$ was guided through the quartz tube. An oxygen pump (SEMG5, Zirox GmbH, Germany) and sensor (YSZ cell, Zirox GmbH, Germany), that were made of a solid ceramic electrolyte based on yttrium stabilized zirconia, were connected to the quartz tube. An oxygen pump was used to control the $p(O_2)$ at the side of gas inlet. At the opposite side (gas outlet) the sensor was used to monitor the real $p(O_2)$ via the electromotive force. In order to stabilize the measurement conditions (e.g. temperature and gas) during analysis, the quartz-tube with the containing ceramic sample was installed into a tubular furnace.

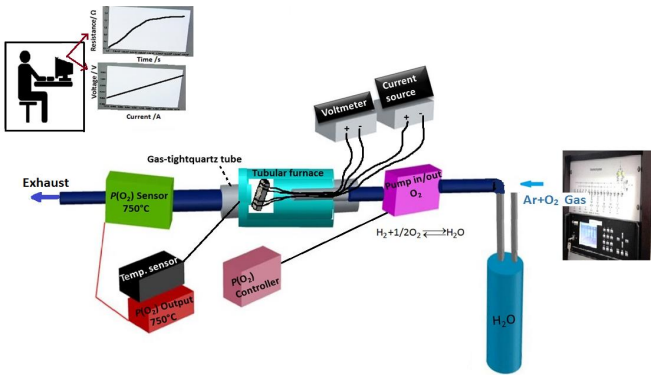

Figure 4-8: Schematic representation of the experimental set-up for DC-measurement. The experimental set up consists of probe (Pt-wire) arrangement, gas-tight quartz tube, tubular furnace (25-1000°C), sample, oxygen pump and sensor, constant current generator, power supply and digital panel meter (measuring voltage and current).

In the oxidizing regime oxygen $p(O_2)$ was controlled by pumping O_2 out of dry Ar using an oxygen electrolytic pump. The $p(O_2)$ within the reducing region was adjusted using a mixture of moist Ar and a hydrogen that was saturated with water at 23°C ($p(H_2O)$ = 2.8 × 10^{-3} MPa) by guiding the gas through a washing bottle filled with water before setting the $p(O_2)$ within the electrolytic Y:ZrO_2 cell. In this case, the oxygen partial pressure at

the sample in the furnace can be calculated from the high temperature equilibrium between oxygen, hydrogen and water gas [83]. The measured values of oxygen partial pressure are determined at 750°C by a sensor. According to the previous report by Katsu [83] in the reducing regime, only at this furnace temperature the relation between the calculated and experimentally monitored oxygen partial pressure is linear. Therefore, in the present dissertation all the measurements where performed at 750°C.

Defect associates between hydroxide ions $(OH^{\bullet})$ and acceptors (e.g. $SrTiO_3$ and $BaTiO_3$ ceramics) are reported in literatures [151, 152]. According to the research performed by Waser [151] for $SrTiO_3$ single crystal, the incorporation/desorption reaction based on the dependence of the solubility on the acceptor concentration and the water vapor pressure $p(H_2O)$ is expressed as: $H_2O + V_O^{\bullet\bullet} + O_O \rightleftharpoons 2(OH)_O^{\bullet}$. For each water molecule dissolved, one oxygen vacancy vanishes and two protons are formed. The protons are bound to oxygen ions on regular sites forming hydroxide ions. The hydrogen defects can be regarded as interstitial protons $H^{\bullet}$. It is reported that the proton solubility as well as the associate formation is not affected by a variation of $p(O_2)$ in the wide range between 10^5 Pa and approx. 10^{-16} Pa (at 875 K). If hydroxide ions are minority species compare to oxygen vacancies, no further cross reactions have to be considered in the defect structure of proton dissolution in compound and it is completely determined by the individual incorporation reactions of $O_O \rightleftharpoons 1/2O_2(g) + V_O^{\bullet\bullet} + 2e'$ and $H_2O + V_O^{\bullet\bullet} + O_O \rightleftharpoons 2(OH)_O^{\bullet}$. Compare to undoped and acceptor-doped materials the oxygen vacancy concentration is several orders of magnitude lower in donor-doped $BaTiO_3$ ceramics and thus hydrogen defects are not detected. In fact, metal ion donors, which are immobile in contrast to oxygen vacancy donors, cannot be replaced by hydrogen defects [152]. In the case of compounds like n-type $CaMnO_{3-\delta}$ and donor-doped $Yb_xCa_{1-x}MnO_3$ there is not any clear statement about the behavior of hydrogen defects and thus further investigations are needed. The author believe that, in contrast with acceptor-doped compounds, the n-type $CaMnO_{3-\delta}$ and Yb-ions do not act as Coulomb attractors for protons and probably no driving force for associate formation exists. Consequently, the defect structure of $CaMnO_{3-\delta}$ can be regarded as completely determined by the reactions $O_O \rightleftharpoons 1/2O_2(g) + V_O^{\bullet\bullet} + 2e'$ and $H_2^{(g)} + 1/2O_2^{(g)} \rightleftharpoons H_2O^{(g)}$.

5 Optimization of powder and ceramic preparation

Before studying the role of the thermodynamic parameters temperature *T* and partial pressure of oxygen $p(O_2)$ on the defect chemistry of $Yb_xCa_{1-x}MnO_3$, this chapter aims to elucidate the influence of these parameters during the calcination and sintering ceramic process on:

- consolidation behavior
- density
- microstructure
- phase purity
- crystallography
- thermal expansion
- O_2 deficiency
- average valency

Since crack formation turned out to be one of the main problems in ceramic processing and electronic measurements, a careful study was required to solve this difficulty in the system under consideration. Besides, some elements affect the electrical analysis such as morphology of the sample, secondary phases, etc. Hence, calcination and sintering experiments were carried out on both powders and ceramics at different temperatures *T* and gas composition types.

5.1 Calcination with respect to temperature and oxidizing atmosphere

To achieve precise results and the best condition for calcination, at first, four samples of pure $CaMnO_3$ (CMO) were prepared at two different temperatures (1000 and 1200°C) and two oxidizing atmospheres (20%O_2+80%Ar and 100% O_2). The average particle size of the respective powders before sintering was obtained by evaluation of SEM micrographs. Details are given in table and Figure 5-1. It is observed as expected that smaller particle size (fine powder) and narrower particle size distribution can be prepared by calcination at lower temperature. In addition, calcination in pure oxygen seems to result in a slightly reduced particle size.

Table 5-1: Average particle size for different calcination conditions.

Symbol	Calcination Temp. / °C	Calcination atmosphere	Average Size of Particles before sintering	
			Min (nm)	Max (µm)
B1	1200	20%O_2 + 80% Ar	100	1.3
B2	1200	100%O_2	80	1.2
B3	1000	20%O_2 + 80% Ar	50	0.7
B4	1000	100%O_2	40	0.6

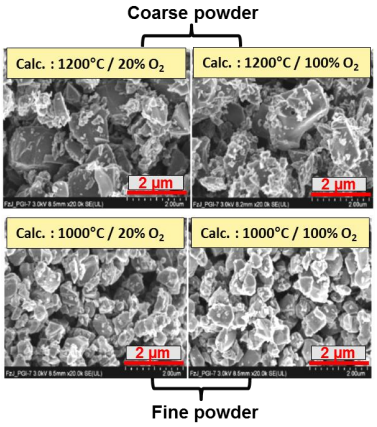

Figure 5-1: SEM images of four samples of pure $CaMnO_3$ calcined at various temperatures (1000 and 1200°C) and oxidizing atmospheres (20%O_2+80%Ar and 100% O_2). The lower calcination temperatures are expected to yield in a smaller particle size.

The next step is to understand the effect of different calcination conditions on the phase purity and the crystallography. The powders structural characterization was carried out for all compounds at room temperature by X-ray powder diffractometer (XRD). Full profile fitting refinements of the final powder diffraction data in the range $20° \leq 2\theta \leq 100°$ were performed using the program FULLPROF, based on the Rietveld method. As shown in Figure 5-2, the characterizations of all samples show a single phase with perovskite structure after calcination (Calc.), except for sample B3 (Calc.: 1000°C, 20%O_2 + 80% Ar). After precise refinement it is observed that this sample contains of three phases: $CaMnO_3$, $CaMn_2O_4$ and Ca_2MnO_4, as demonstrated in Figure 5-3. This means that calcination at lower temperature must be carried out at high partial pressure of oxygen in order to obtain phase pure $CaMnO_3$.

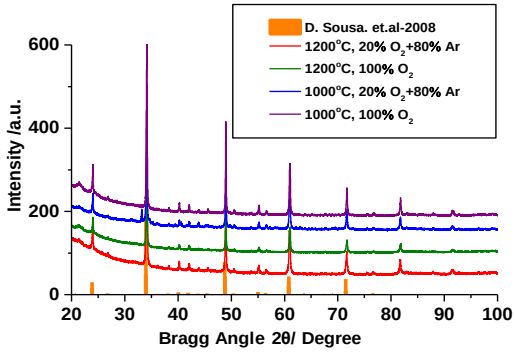

Figure 5-2: XRD after calcination at different temperatures and oxidizing atmospheres. All the XRD patterns represent a single phase of $CaMnO_3$, however there are some small impurity peaks for the sample calcined at 1000°C in 20%O_2 + 80% Ar.

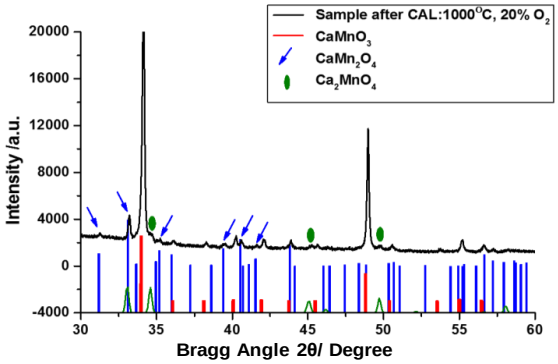

Figure 5-3: XRD pattern for pure $CaMnO_3$, calcined at 1000°C in 20%O_2+80%Ar, contains three phases: $CaMnO_3$, $CaMn_2O_4$, and Ca_2MnO_4.

In fully oxidized pure $CaMnO_3$ the valency of all Mn cations should be 4+ (Mn^{4+}). Calcination at lower temperature and at low partial pressure of oxygen leads to appearance of Mn^{3+} cations, which means that the compound is not completely oxidized and thus $CaMn_2O_4$ phases are formed.

5.2 Sintering with respect to different gas composition types

In order to investigate the shrinkage behavior in dimension of the pellets dilatometry analysis (DIL.) was performed for pure $CaMnO_3$ samples B1, B2, B3 and B4 with different calcination temperatures and oxidizing atmospheres (details were given in Table 4-1). Four samples of each type of pellets (B1-B4) were prepared and dilatometry was carried

out at 1350°C with a heating and cooling rate of 5 K/min in four different gas composition types respectively:

- High $p(O_2)$ with oxygen concentration of : a) 100% O_2 and b) 20% O_2 +80% Ar
- Low $p(O_2)$ with oxygen concentration of: c) 1% O_2 +99% Ar and d) 100% Ar.

The density of all pellets after sintering was determined by the Archimedes method. Theoretical density for calcium manganite composition which is fully reacted is expected to be 4.58 g/cm^3 [64]. The results approved that no open porosity was contained in all cases, because the densities of all samples were above 98% of the theoretical value; except for compounds which were sintered in dilatometer in 100% argon, with a density of only around 90%.

The following sections reveal the important effects of different calcination and sintering conditions on the physical and chemical properties of the investigated compounds.

5.3 Stoichiometric Calcium manganite

5.3.1 Microstructure, phase purity and crystallography

Scanning electron microscopy (SEM) reveals that even after sintering with the same conditions the average grain size reduces with respect to the decrease of the calcination temperature. This reduction is observed for sintering at high $p(O_2)$ gas compositions (20% O_2 + 80% Ar and 100% O_2) from around 14 to 9 µm and at low $p(O_2)$ gas composition (1% O_2 + 99% Ar) from around 16 to 12 µm.

Regarding to the different sintering conditions the results listed below are obtained:

(i) For sintering at high $p(O_2)$ gas compositions polygonal grains are visible very clearly (Figure 5-4a). (ii) At low $p(O_2)$ all pellets were cracked, except for samples that were calcined at low temperature ≈1000°C and in 100% O_2. Only these ceramic pellets contain needle-like shaped crystallites (Figure 5-4b). (iii) Compounds sintered in 100% Ar do not possess any polygonal grain on the surface but only needle shaped crystallites (Figure 5-4c), and their structure morphology are totally different from the other sintering conditions.

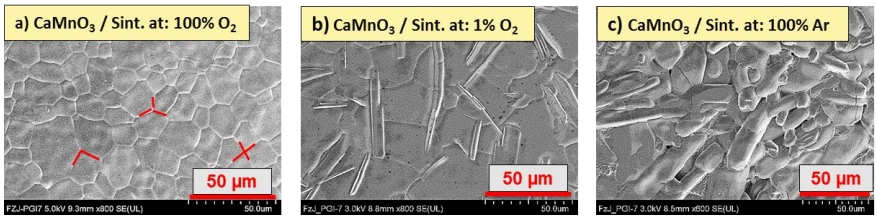

Figure 5-4: SEM images after sintering in dilatometer at 1350°C in different gas composition types. a) High $p(O_2)$ (sintering at: 100% O_2): polygonal grains are visible clearly. The grain boundaries may form in angles between around 90° and 120°, b) Low $P(O_2)$ (sintering at: 1% O_2 + 99% Ar): contain needle shaped crystallites. c) Sintering at: 100% Ar: no polygonal grain visible but only needle shaped crystallites.

Microstructural characterizations confirm the significant effect of the different calcination conditions on the surface morphology of the ceramics even after sintering at the same condition. As an example the different SEM and EDX analysis after polishing and thermal etching of stoichiometric $CaMnO_3$ calcined at various conditions (B4, calcined at 100% O_2 and 1000°C, and B3, calcined at 20% O_2 and 1000°C) and sintered in the same environment of 100% Ar are illustrated in Figure 5-5. Pores are observable on the surface of all the compounds. Three maps are recorded simultaneously for each compounds using image brightness intensity as a function of the local relative concentration of the elements, calcium (Ca), manganese (Mn), and oxygen (O). For instance, bright green colors indicate more local concentration of calcium than manganese and dark colors represent the lack of calcium.

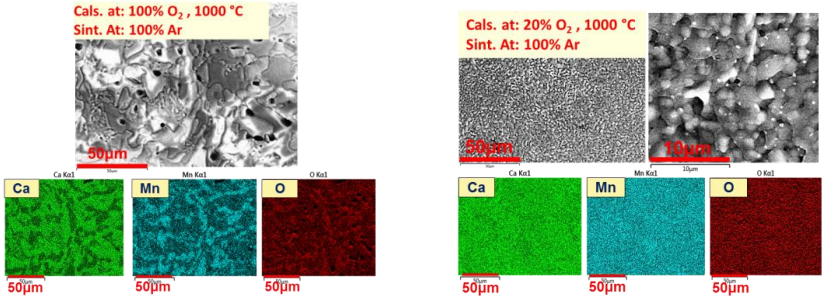

Figure 5-5: SEM and EDX images after polishing and thermal etching for compounds B4, calcined at 100% O_2 and 1000°C (left side), and B3, calcined at 20% O_2 and 1000°C (right side). Both compounds sintered in the same condition at 100% Ar, however show a different surface morphology. EDX measurement demonstrates clearly the local concentration of the specific element by brightness intensity.

To clarify the localized elemental information of the needles as well as other surface area of the ceramic samples, EDX measurement was performed after polishing and thermal etching. A series of local point analysis was concluded. The relative atomic percentage of each element is shown in Figure 5-6. Spectrum 3 on the needle indicates more calcium (Ca) relative concentration than manganese (Mn). Besides, spectrum 7 demonstrates more atomic percentage of Mn than Ca, and spectrum 10 shows equal amount of Ca and Mn.

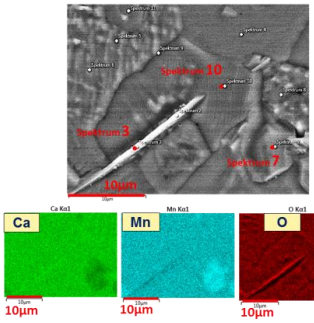

Spectrum 3	At %
O	68.7
Ca	17.2
Mn	14.1

Spectrum 7	At %
O	58.0
Ca	17.6
Mn	24.4

Spectrum 10	At %
O	57.1
Ca	21.5
Mn	21.4

Figure 5-6: EDX images after polishing and thermal etching of compound B4, calcined at 1000°C in 100% O_2, after sintering in dilatometer in 1% O_2 + 99% Ar. The electron beam stationary was kept on series of spots and generated spectra that provided localized elemental information.

In order to find more information about phase purity and crystallography of these compounds XRD measurements were carried out, as shown in Figure 5-7.

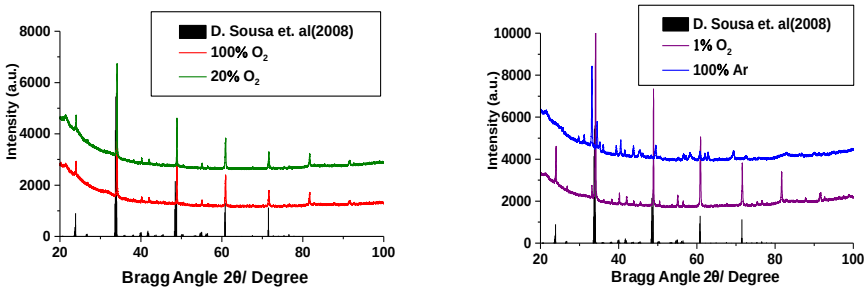

Figure 5-7: XRD patterns for $CaMnO_3$ compounds sintered: at high oxygen concentration (100% O_2 and 20% O_2 + 80% Ar) reveal orthorhombic single phase $CaMnO_3$ (left side), and at low oxygen concentration (1% O_2 + 99% Ar) illustrate small extra peaks and in 100% Ar show phase transition to Ca_2MnO_4 and $CaMn_2O_4$ (left side). The black pattern shows the reference data [64].

The XRD patterns index to a single phase $CaMnO_3$ and an orthorhombic system, Pnma space group for compounds sintered in high $p(O_2)$. The lattice parameters for samples

sintered in pure oxygen are a = 5.2872(8) Å, b = 7.4640(16) Å and c = 5.2709(7) Å which is refined based on PDF card (#40-16-2215). For compounds sintered at low oxygen concentration (1% O_2 + 99% Ar) XRD pattern represents small extra peaks. For sintering in pure Ar phase transition is observed to Ca_2MnO_4 and $CaMn_2O_4$.

A comparison of the results obtained from EDX (Figure 5-6) and XRD measurement (Figure 5-7) confirm the existence of three phases on the compounds sintered at low oxygen concentration and 100% Ar, including Ca_2MnO_4 phase as needle shaped crystallites and two other phases of $CaMn_2O_4$ and $CaMnO_3$ on the other parts of the surface.

Raman spectra in complementarity with XRD were carried out (Figure 5-8) in order to investigate the local crystal structure for $CaMnO_3$ ceramics which were calcined in 1000°C and sintered in different gas composition types.

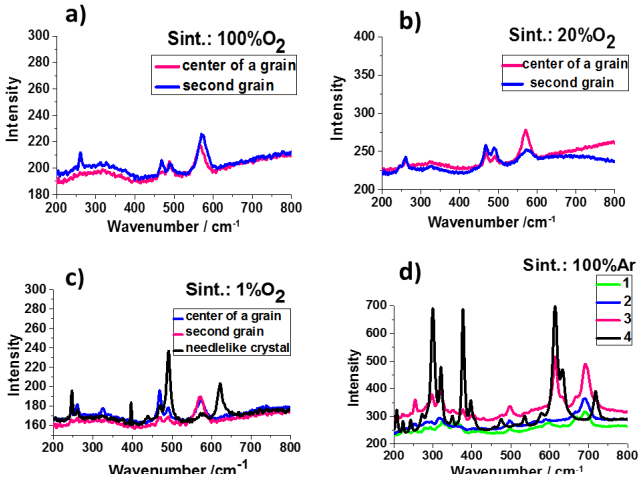

Figure 5-8: Raman spectra recorded at room temperature obtained from the series of spots on the surface of $CaMnO_3$ ceramic, sintered in: a) pure oxygen , b) 20% O_2 + 80% Ar, c) 1% O_2 + 99% Ar, and d) 100%Ar.

(i) Compounds which were sintered in high $p(O_2)$ correspond to the single phase of $CaMnO_3$ [153]. However (ii) for compounds sintered in 1% O_2+99%Ar, the spectrums of the needle shaped crystals are different from the spectrum of $CaMnO_3$ (Figure 5-8c black curve). According to the reference data [154] (iii) the black spectrum of compounds sintered in pure Argon can be assigned to $CaMn_2O_4$ (Figure 5-8d). Differences in relative intensities depend on sample orientation as expected for oriented crystals.

5.3.2 Dilatometry and thermal expansion

Figure 5-9 shows the shrinkage rate in dimension of the $CaMnO_3$ ceramic pellets calcined at different conditions using dilatometry. It is clear that the extend of shrinkage for compounds containing fine powders (calcined at lower temperature) is 1.5 times larger than for pellets with coarse powder (calcined at higher temperature). As shown in Figure 5-10 (left side), the temperature (T_{max}) of maximum shrinkage rate per minute observed for fine powder is around 1100°C, while this value increase to around 1200°C for coarse powders.

Regarding to the different sintering conditions the results listed below are obtained:

(i) Compounds sintered at high oxygen concentration (100% O_2 and 20% O_2 + 80% Ar) start to shrink at around 960°C which is higher than for compounds sintered at lower oxygen concentration (1% O_2 + 99% Ar and 100% Ar) with start shrinkage temperature around 900°C. This could be due to the release of more amount of oxygen from compound during sintering at low oxygen concentration.

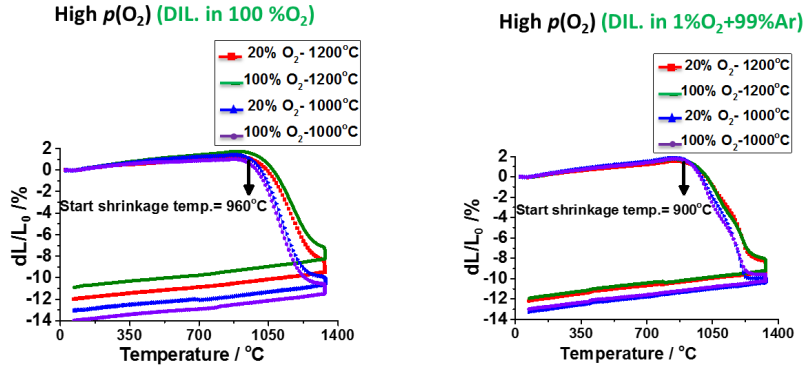

Figure 5-9: The shrinkage behavior in dimension of the pellets, calcined at different conditions, using dilatometry analysis (DIL). Pellet samples sintered in 100 %O_2 (left side) start to shrink at higher temperature T_{start} ≈ 960°C, than samples sintered in 1% O_2 + 99% Ar T_{start} ≈ 900°C (right side).

(ii) At high $p(O_2)$ only one maximum shrinkage peak is observed at around 1100°C (Figure 5-10 left side). However, the compounds sintered at lower $p(O_2)$ contain two maximum shrinkage rates at temperatures around 1000 and 1200°C respectively (Figure 5-10 right side).

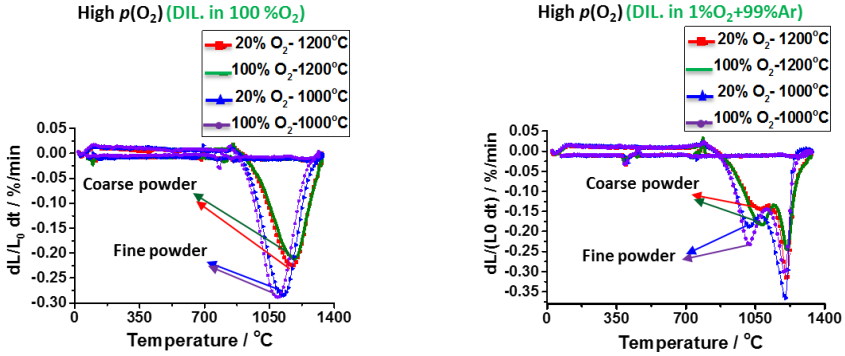

Figure 5-10: Temperature dependence of shrinkage rate per minute using dilatometry analysis (DIL) for stoichiometric $CaMnO_3$ compounds calcined at different conditions, includes compounds sintered in 100% O_2 (left side) and in 1% O_2 + 99% Ar (right side). Differential sintering is observable in the latter case. For both sintering conditions, the maximum shrinkage rate per minute for samples contain fine powders is larger than the shrinkage rate for samples contain coarse powder.

In order to understand the reason of such behavior of the curves, the release of oxygen is monitored precisely by ZrO_2 oxygen sensor during the dilatometry measurements in pure argon simultaneously, as shown in figure 5-11.

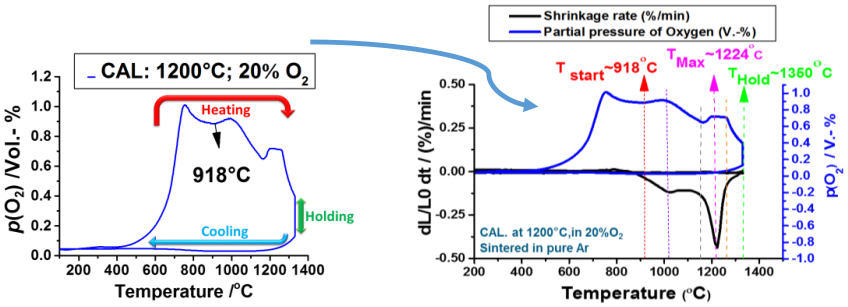

Figure 5-11: The release of oxygen monitored precisely by ZrO_2 oxygen sensor from room temperature to 1350°C for compound calcined at 1200°C and 20%O_2+80%Ar, and sintered in dilatometry in 100% Argon (left side). Comparing two diagrams of shrinkage rate (black curve) and the rate of released partial pressure of oxygen (blue curve). The start shrinkage temperature (T_{start}), temperature of maximum shrinkage rate (T_{max}), and temperature of holding sample before cooling down (T_{hold}) are specified.

This analysis can detect the altered number of oxygen vacancy concentration present in the sample with respect to the temperature from 25 to 1350 °C. As demonstrated in figure 5-11 (left side), compound heated up and was kept in 1350°C for 6 hours and then cooled down. It shows that in which temperature a sample start losing oxygen. The

amount of oxygen released can be calculated with the equation 4-2. In order to find out the relation between shrinkage and oxygen vacancy, the figure mentioned above is also represented in combination with shrinkage rate at the same plot, as shown in Figure 5-11 (right side). Comparing the diagrams of shrinkage rate and the rate of released oxygen reveals that as the temperature increases the oxygen released from the sample with variable rate influence the rate of shrinkage. After starting shrinkage at around 918°C, as the amount of released oxygen increases shrinkage rate also increases and vice and versa. This measurement was carried out for all the other investigated compounds and the same trend is observed.

Consequently, from these results and from phase purity and crystallography measurements (Figure 5-6, 5-7, and 5-8) it is concluded that during sintering in 100% Ar $CaMnO_3$ decompose to Ca_2MnO_4 and $CaMn_2O_4$. Therefore, with increasing temperature relatively larger amount of oxygen release from the compounds and thus the second maximum shrinkage peak occurs.

5.3.3 Thermogravimetric analysis (TGA)

TGA measurements were performed for grinded-sintered stoichiometric $CaMnO_3$ ceramics in a wide $p(O_2)$ range from 10^{-18} up to 10^{-1} MPa at a constant elevated temperature of 750°C. As shown in figure 5-12, weight of the compound increases by increasing $p(O_2)$. The reasons of this enhancement are discussed below.

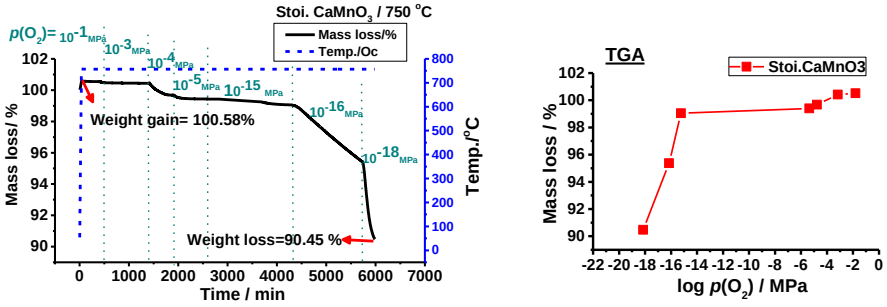

Figure 5-12: Thermogravimetric measurement for stoichiometric $CaMnO_3$ which demonstrates increase in oxygen vacancy concentration with decreasing $p(O_2)$ from 10^{-1} to 10^{-18} Mpa. The $p(O_2)$ values are indicated between cyan doted lines.

- **High $p(O_2)$: $>10^{-6}$ MPa**

At sufficiently high $p(O_2)$, the major source of defects is the oxidation reaction. In the case of active schottky disorder, this reaction can increase the number of holes while the concentration of oxygen vacancies decreases, as formulated below.

$$\frac{3}{2}O_2 \rightleftarrows 3O_O^X + V_{Mn}''' + V_{Ca}'' + 6Mn_{Mn}^{\bullet} \qquad \textbf{Eq. 5-1}$$

Accordingly with increasing $p(O_2)$ above 10^{-6} MPa the weight of the compound increases gradually because of up taking oxygen.

- **Intermediate $p(O_2)$: $10^{-14} < p(O_2) < 10^{-6}$ MPa**

In intermediate region, from around 10^{-6} down to to 10^{-14} MPa the exact value of oxygen partial pressure cannot be controlled, however it seems to be approximately plateau.

As described in previous sections, the XRD-measurements demonstrate orthorhombic structure $CaMnO_3$ phase after sintering in pure oxygen at 1350°C. However, two phases of Ca_2MnO_4 and $CaMn_2O_4$ are observed after sintering at $p(O_2)$ lower than 10^{-2} MPa (1% O_2 + 99% Ar and pure Ar).

It seems with decreasing $p(O_2)$ positions of oxygen anions in the lattice might be shifted, therefore the secondary phases Ca_2MnO_4 and $CaMn_2O_4$ are formed. Probably the secondary phases which are concentrated near the grain boundaries temporarily form barriers to oxygen migration. Accordingly, mass loss (oxygen released) is reduced from grain to grain boundaries and thus to the atmosphere in the intermediate region.

- **Low $p(O_2)$: $<10^{-14}$**

With decreasing $p(O_2)$ down to 10^{-16} MPa, compound releases more amount of oxygen in order to maintain equilibrium and thus mass of compound decreases slightly. In the $p(O_2)$ around 10^{-16} MPa another phase ($CaMnO_{2.5}$) is formed. This phase possesses the same atomic arrangement as $CaMnO_3$ except the oxygen defect-sites in the crystal structure. The $CaMnO_{2.5}$ phase which is also known as $Ca_2Mn_2O_5$ contains five coordinated square pyramid subunit between Mn and oxygen which all five oxygen atoms are linked with adjacent subunit through corner oxygen atoms. This structure could facilitate ion transport for oxygen evolution reaction via oxygen vacancies [155]. Therefore, in further reduction region lower than 10^{-16} MPa drastic mass loss is

attributed to the release of higher amount of oxygen which causes a change in structure from orthorhombic to cubic symmetry in $CaMnO_2$ phase.

XRD-measurements successfully confirm this suggestion with detecting a main phase of $CaMnO_2$ after TGA measurement in the highly reduction region of $p(O_2) \approx 10^{-18}$ MPa. This compound is also known as $Ca_{0.5}Mn_{0.5}O$ with cubic crystalline structure and lattice parameter of a = 4.622±0.002 Å. The structure of $CaMnO_2$ is characterized by oxygen vacancies generated by the reduction of Mn^{4+} in $CaMnO_3$ to Mn^{3+} in $CaMnO_{2.5}$ and then at highly reduction region reduced to Mn^{2+} in $CaMnO_2$ [156].

The crystallographic data for $CaMnO_3$ after sintering and after TGA measurement are listed in tables 5-2 and 5-3, respectively.

Table 5-2: Crystallographic data of $CaMnO_3$ after sintering in pure oxygen at 1350°C.

Crystalline structure	Space group	a/ Å	b/ Å	c/ Å	Volume/ Å^3
$CaMnO_3$ Perovskite/ orthorhombic	Pnma 62	5.2870(4)	7.4640(11)	5.2705(5)	207.99(3)

Table 5-3: Crystallographic data of $CaMnO_3$ after TGA measurement at 750°C in $p(O_2) \approx 10^{-18}$ MPa.

Crystalline structure		Refrence
$Ca^{2+}_{0.5}Mn^{2+}_{0.5}O^{2-}$ ($CaMnO_2$)	Main phase (rock-salt - Cubic)	PDF #4-7-8378
$Ca^{2+}Mn^{4+}O_3$	very low amount	PDF #4-16-2215
$Mn^{3+}_2O^{2+}_3$	very low amount	PDF #31-825
$Mn^{2.67}_3O^{2-}_4$	very low amount	PDF #4-18-7078

After achieving fundamental results for pure $CaMnO_3$, the following purpose was to study the surface morphology and crystallography of non-stoichiometry and doped-$CaMnO_3$, which is explained in detail in the following sections.

5.4 Non-stoichiometric calcium manganite: Ca- & Mn-excess

5.4.1 Microstructure, phase purity and crystallography

Scanning electron microscopy of the two non-stoichiometric calcium manganite compositions $Ca_{1.01}MnO_3$ and $CaMn_{1.01}O_3$ was studied after sintering in different gas compositions. Figure 5-13 shows only the case of Ca-excess, since the respective micrographs for Mn-excess are qualitatively comparable and show a similar grain size.

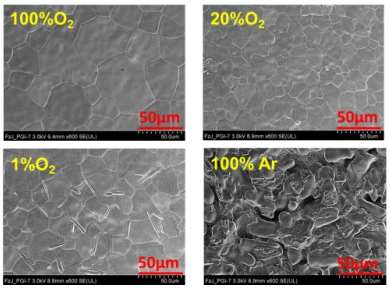

Figure 5-13: SEM images of sample with calcium excess ($Ca_{1.01}MnO_3$) after sintering in 100% O_2, 20% O_2 + 80% Ar, 1% O_2 + 99% Ar or 100% Ar.

It is observed that both of the non-stoichiometric samples have approximately the same behavior as stoichiometric $CaMnO_3$ (Figure 5-4). The results show polygonal grains for compounds sintered in high oxygen concentrations (100% O_2 and 20% O_2 + 80% Ar), needle shaped crystallites mixed with polygonal grain for sintering in low oxygen concentration (1% O_2 + 99% Ar) and only needle shaped crystallites for sintering in pure Ar. However, the average grain size for non-stoichiometric compounds (≈17 µm) is around 1.7 times larger than stoichiometric $CaMnO_3$ (≈ 10 µm). Therefore it can be concluded that both Ca-excess and Mn-excess only have a very minor but existing effect on the microstructure slightly promoting grain growth.

The investigation of crystallography for the samples was carried out by X-ray powder diffraction, before and after sintering in pure oxygen (Figure 5-14). The results show identical peaks for both non-stoichiometric samples with no detectable trace of any other phases.

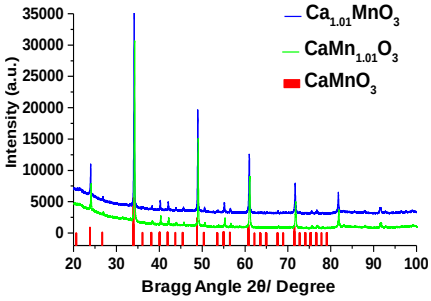

Figure 5-14: X-ray powder diffraction of non-stoichiometric samples, $Ca_{1.01}MnO_3$ and $CaMn_{1.01}O_3$, present identical single phase with orthorhombic Pnma space group, for both compounds sintered in 100% O_2.

All peaks index in the orthorhombic Pnma space group. The determined lattice parameters basing on the orthorhombic phase $CaMnO_3$ (PDF #4-16-2215) are listed in table 5-4.

Table 5-4: Determined lattice parameters based on the orthorhombic phase $CaMnO_3$.

Sample	a / Å	b / Å	c / Å	V / Å^3
$CaMnO_3$	5.2872(8)	7.4640(16)	5.2709(7)	208.00(8)
$Ca_{1.01}MnO_3$	5.2869(11)	7.4609(24)	5.2734(23)	208.01(10)
$CaMn_{1.01}O_3$	5.2879(10)	7.4620(30)	5.2718(30)	208.01(14)

The EDX results after thermal etching (Figure 5-15) show that, the needle shaped crystallites on the surface of the samples sintered in low oxygen concentration (1% O_2 + 99% Ar) mostly contain calcium and have lower amount of manganese. Comparing EDX results with XRD measurement at low $p(O_2)$, which are the same as stoichiometric samples (Figure 5-7), demonstrates the Ca_2MnO_4 phase as needle shaped crystallites.

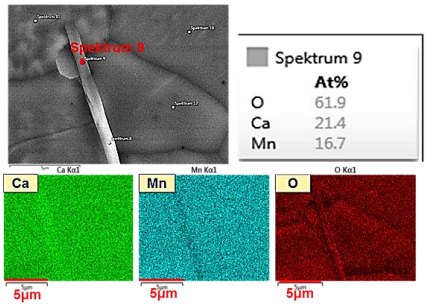

Figure 5-15: EDX-spectroscopy of $Ca_{1.01}MnO_3$ sintered in 1%O_2+99%Ar, after polishing and thermal etching.

5.4.2 Dilatometry and thermal expansion

Shrinkage behavior in dimension of the non-stoichiometric compounds $Ca_{1.01}MnO_3$ and $CaMn_{1.01}O_3$ was performed in different gas compositions, as shown in figure 5-16. The results reveal approximately identical behavior for both Ca- and Mn-excess compounds in comparison to the stoichiometric $CaMnO_3$. Differential sintering is observed for all samples sintered at low $p(O_2)$. More details are listed in table 5-5.

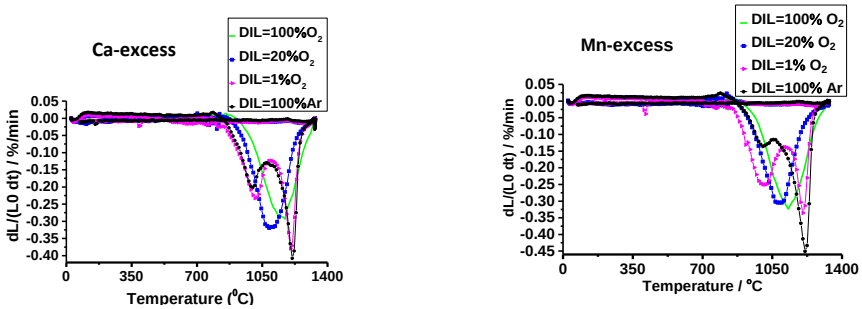

Figure 5-16: Temperature dependence of shrinkage rate per minute for $Ca_{1.01}MnO_3$ (left side) and $CaMn_{1.01}O_3$ (right side). Differential sintering is observed for both compounds sintered in low oxygen concentration ≈ 1%O_2 +99%Ar and 100%Ar.

Table 5-5: Dilatometry analysis: comparison of stoichiometric $CaMnO_3$ with non-stoichiometric compounds $Ca_{1.01}MnO_3$ and $CaMn_{1.01}O_3$.

	Start shrinkage temp. / °C		**Temp. of Max. shrinkage rate / °C**	
Gas conc. in DIL.	High $p(O_2)$	low $p(O_2)$	High $p(O_2)$	low $p(O_2)$ (two peaks)
Stoi. $CaMnO_3$	≈960 °C	≈ 900 °C	≈ 1100	≈1000 & 1200
Ca-excess & Mn-excess	≈ 980 °C			

For non-stoichiometric compounds sintered at high $p(O_2)$ the temperature at which shrinkage starts is T_{start} ≈980°C. The maximum shrinkage rate amounts to $Sh.R._{max}$ ≈ 0.30 %/min and a maximum shrinkage peak is at 1100°C observed. Sintering at lower $p(O_2)$ results in a lower value of T_{start} ≈ 900°C, due to the release of more amount of oxygen at low oxygen concentration, and thus causes a slightly higher value of $Sh.R._{max}$≈ 0.40 %/min. Also two maximum shrinkage rate peaks at 1000 and 1200°C appear. The reason of possessing second maximum shrinkage peak is revealed by monitoring the release of oxygen using ZrO_2 oxygen sensor. Approximately the same behavior is observed for both Ca- and Mn-excess compounds. As illustrated in figure 5-17, similarly to the stoichiometric case of $CaMnO_3$, the second maximum shrinkage peak occurs at around 1200°C. This is possibly due to the existence of secondary phases Ca_2MnO_4 and $CaMn_2O_4$, as confirmed by XRD measurements after dilatometry in 1% O_2+99% Ar and pure Ar.

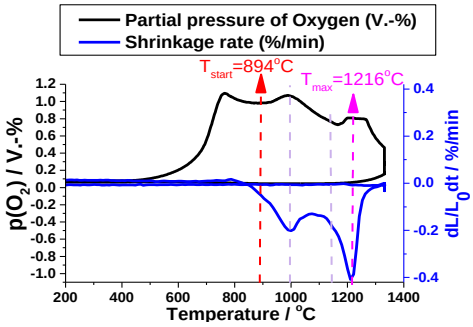

Figure 5-17: The released oxygen monitored by ZrO_2 oxygen sensor from room temperature to around 1400°C for the compound $Ca_{1.01}MnO_3$ (black curve). Shrinkage is associated with increasing the amount of released oxygen from the compounds (blue curve). Start shrinkage temperature (T_{start}) and maximum shrinkage temperature (T_{max}) are specified.

5.4.3 Thermogravimetric analysis (TGA)

Mass loss curves are shown in figure 5-18 for grinded-sintered non-stoichiometric $CaMn_{1.01}O_3$ (Mn-excess) and $Ca_{1.01}MnO_3$ (Ca-excess) in wide range of $p(O_2)$, from 10^{-1} to 10^{-19} Mpa.

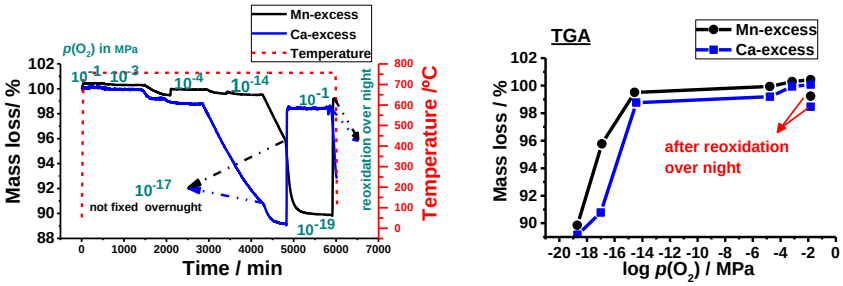

Figure 5-18: Comparison of weight loss (oxygen loss) of $CaMn_{1.01}O_3$ (Mn-excess) and $Ca_{1.01}MnO_3$ (Ca-excess) with decreasing $p(O_2)$ from 10^{-1} to 10^{-19} Mpa.

As the case of stoichiometric compositions, weight loss (oxygen loss) is observed for both non-stoichiometric compounds with decreasing $p(O_2)$. In an intermediate region, from 10^{-5} to 10^{-14} MPa, the plot seems to be approximately plateau. At $p(O_2)$ around 10^{-14} to 10^{-16} MPa weight of the compounds decrease slightly (i.e. gradual increase in oxygen vacancy). The results demonstrate significant increase in oxygen vacancy concentration at lower than $p(O_2)\approx10^{-16}$ with 10.92% mass loss at 10^{-19} MPa. This trend is similar to stoichiometric compounds $CaMnO_3$. As discussed in section 5.3.3, the drastic

mass loss at high reduction region $p(O_2) < 10^{-16}$ is due to the decomposition into the $Ca_{0.5}Mn_{0.5}O$ phase. Such a change in structure from orthorhombic to cubic symmetry causes drastic increase in oxygen vacancy concentration.

In addition, both samples represent weight gain (oxygen gain) around 99% after reoxidization in $p(O_2) \approx 10^{-1}$ MPa.

5.5 Donor doping: Yb-doped calcium manganite

5.5.1 Microstructure, phase purity and crystallography

Ytterbium doped calcium manganite compounds $Yb_xCa_{1-x}MnO_3$ (0 to 10% Yb-doped) were investigated at different sintering gas compositions including 100% O_2, 20% O_2 +80% Ar, 1% O_2 +99% Ar and 100% Ar.

The SEM images of Yb-doped $CaMnO_3$ (Figure 5-19) demonstrate that, grain size only slightly decreases by increasing the doping concentration from 11 µm for 0.1 % to 10 µm for 1% of dopant concentration. Above 5 at. % of Yb addition the grain size decreases continuously down to 3 µm at 10 at. % of Yb.

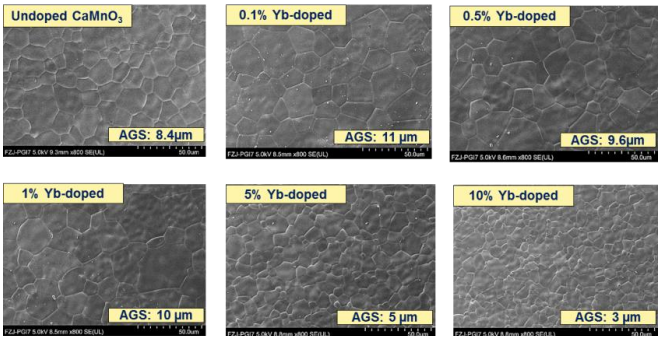

Figure 5-19: SEM images for compounds sintered in 100% O_2 with different doping concentration. The average grain size (AGS) is calculated for each sample.

The SEM images for 5 at. % Yb-doped $CaMnO_3$, shown in figure 5-20, indicate visible polygonal grains for sintering in high oxygen concentration (100%O_2 and 20%O_2+80% Ar) while a few needle shaped crystallites also are observed for sample sintered in 1% O_2. Compounds sintered in pure Ar do not possess any polygonal grain on the surface but only needle shaped crystallites. The effect of different sintering gas compositions on the microstructure is similar for all other investigated compounds.

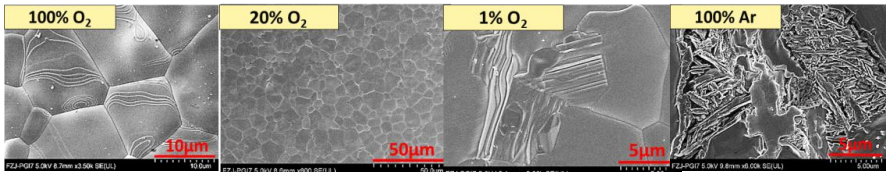

Figure 5-20: 5% Yb-doped $CaMnO_3$ compounds sintered in high oxygen concentration (100%O_2 and 20% O_2 + 80% Ar) show visible polygonal grains clearly, for sintering in low oxygen concentration (1% O_2 + 99% Ar) there are a few needle shaped crystallites, and for compounds sintered in pure Ar only needle shaped crystallites are observable.

To obtain information about crystallography of the compounds $Yb_xCa_{1-x}MnO_3$ (x = 0 to 0.1) XRD measurements were performed. Figure 5-21 shows the XRD-patterns for 10%Yb-doped $CaMnO_3$ sintered in different gas compositions. All the other samples represented the same behavior.

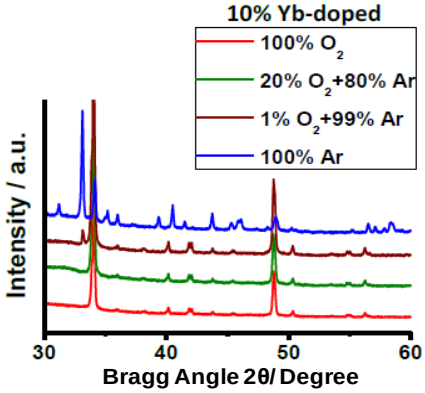

Figure 5-21: The XRD patterns of compounds $Yb_{0.1}Ca_{0.9}MnO_3$ after sintering in different gas compositions, reveal phase transition from orthorhombic single phase to Ca_2MnO_4 and $CaMn_2O_4$ by decreasing $p(O_2)$.

Compounds which were sintered in high oxygen concentration (100% O_2 and 20% O_2 + 80% Ar) turn out to be single phase of the orthorhombic perovskite structure. Table 5-6 represents the determined lattice parameters basing on the orthorhombic phase $CaMnO_3$ (PDF #4-16-2215). With increasing Yb-dopant concentration volume of unit cell increases slightly by approximately 0.5% up to 209.02 (10) $Å^3$ at 10 at. % Yb. Donor doping results in reduction of Mn^{4+} to Mn^{3+}. The ionic radius of Mn^{3+} (0.64 Å) is larger than that of Mn^{4+} (0.53 Å) [42] which causes slight increase in the lattice parameters.

Table 5-6: Lattice parameters for $Yb_xCa_{1-x}MnO_3$ (x = 0 to 0.1) sintered in 100% O_2.

Sample	a / Å	b / Å	c / Å	V / Å^3
$CaMnO_3$	5.2872(8)	7.4640(16)	5.2709(7)	208.00(8)
$CaMnO_3$ + 0.1% Yb	5.2863(10)	7.4607(19)	5.2668(12	207.71(12)
$CaMnO_3$ + 0.5% Yb	5.2883(9)	7.4597(23)	5.2692(10)	207.86(12)
$CaMnO_3$ + 1% Yb	5.2886(12)	7.4579(30)	5.2741(30)	208.02(17)
$CaMnO_3$ + 5% Yb	5.2877(17)	7.4693(30)	5.2714(24	208.20(21)
$CaMnO_3$ + 10% Yb	5.3105(9)	7.4662(17)	5.2716(10)	209.02(10)

All compounds sintered in low oxygen concentration (1% O_2 +99% Ar) show additional reflections. The XRD patterns of all the doped and undoped compounds after sintering in 100% Ar are different from the other sintering conditions. As shown in figure 5-22, phase transition is observed from Ca_2MnO_4 to $CaMn_2O_4$ by increasing Yb-concentration. Yb seems to stabilize preferentially $CaMn_2O_4$ instead of Ca_2MnO_4 under reducing condition.

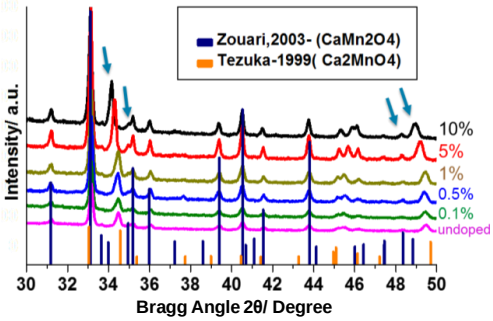

Figure 5-22: The XRD pattern of compounds $Yb_xCa_{1-x}MnO_3$ (x= 0 to 0.1) after sintering in 100% Ar. Phase transition from Ca_2MnO_4 to $CaMn_2O_4$ by increasing Yb-concentration.

In summary, it is found that different sintering conditions, in this case different gas compositions, significantly affect the microstructures, crystallization and phase changes of compound. In the next section a systematic study was carried out in order to understand the effect of different sintering condition on the expansion or shrinkage of pellet samples. Besides, the eventual formation of oxygen vacancy during sintering was investigated.

5.5.2 Dilatometry and thermal expansion

Since electrical measurements of ceramic compounds are performed after sintering, an accurate investigation on the behavior of the sintered compounds in dependence of

temperature is important. Therefore different compounds $Yb_xCa_{1-x}MnO_3$ (0 to 10 at. % concentration of Yb-dopant) were sintered first and then investigated by dilatometry analysis in a wide temperature range from room temperature to around 1400°C. This accurate investigation on the behavior of the sintered compounds in particular regarding to behavior of oxygen release in dependence of temperature is extremely important also with regard to electrical behavior.

As shown in figure 5-23, (i) for compounds containing 0 to 1 at. % Yb-addition the temperature at which shrinkage starts T_{start} is about 1000°C. The maximum shrinkage peak for these compounds is at $T_{max} \approx 1150$°C (Figure 5-23 right side). (ii) Increasing Yb-concentration up to 5% has negligible effect on T_{start} however T_{max} increases to around 1200°C. (iii) In the case of 10% Yb-doped shrinkage starts at higher temperature around 1100°C. T_{max} also enhances to around 1300°C. Details are listed in table 5-7.

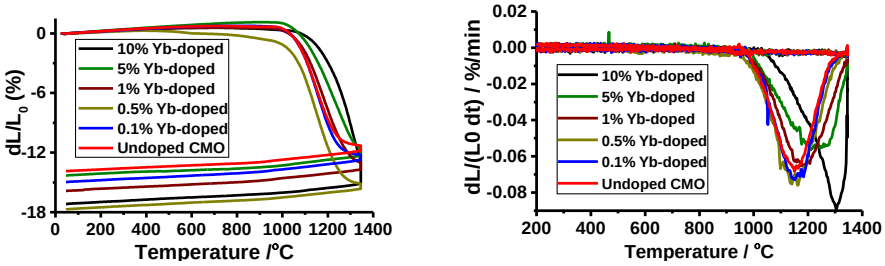

Figure 5-23: Temperature dependence of shrinkage in dimension (left side) and Yb-doped concentration dependence of shrinkage rate per minute from room temperature to around 1400°C (right side), for $Yb_xCa_{1-x}MnO_3$ (0 to 10% Yb-doped) sintered in 100% O_2.

Table 5-7: Dilatometry analysis: comparison of compounds $Yb_xCa_{1-x}MnO_3$ with 0 to 10% concentration of Yb-dopant.

DIL.in 100% O_2 / Yb-doped conc.	Start shrinkage temp. / °C	Temp. of Max. shrinkage rate / °C
0% to 1 %	≈ 1000 °C	≈ 1150
5 %	≈ 1000 °C	≈ 1200
10 %	≈ 1100 °C	≈ 1300

According to figure 5-24, the dependence of the maximum shrinkage rate from the Yb-concentration is variable for $Yb_xCa_{1-x}MnO_3$ (0 to 10% Yb-doped) sintered in 100% O_2. Compared with stoichiometric $CaMnO_3$, maximum shrinkage rate slightly increases up to 0.5 at. % of Yb addition, while it decreases by adding more Yb concentration up to 5%.

The highest maximum shrinkage rate per minute is observed for compounds containing 10 at. % Yb dopant (≈ 0.09 %/min).

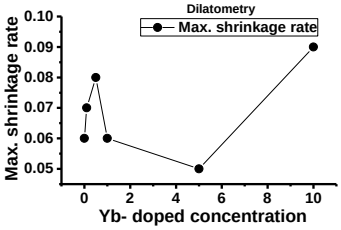

Figure 5-24 : Dependence of the maximum shrinkage rate from the Yb-concentration for $Yb_xCa_{1-x}MnO_3$ (0 to 10 at. % Yb-addition) sintered in 100% O_2.

The variable trends in maximum shrinkage rate (Figures 5-24) could be due to the individual amount of oxygen released from each sample.

To prove this issue, the release of O_2-gas was monitored by a ZrO_2 oxygen sensor during sintering in the dilatometer using pure argon (Figure 5-25).

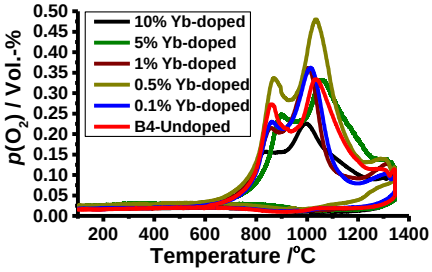

Figure 5-25: Temperature dependence of oxygen release for compounds $Yb_xCa_{1-x}MnO_3$ (0 to 10 at. % Yb-addition) using dilatometer in pure Argon.

Increasing temperature up to around 1100 °C enhances the amount of oxygen released. Further increase in temperature up to 1200 °C results in release of a lower amount of oxygen. However, at temperatures above 1200°C a slight increase is observed again. Compounds were kept at 1350 °C for 6 hours and then cooled down. As demonstrated in figure 5-25, the volume percentage of oxygen released is variable for the different Yb-doped concentrations. This measurement does help to understand the relation between the amount of released oxygen and variable amount of shrinkage rate. Compared with stoichiometric $CaMnO_3$, the maximum volume of oxygen released slightly increases up to 0.5 at. % Yb-doped, while it decreases by adding more Yb

concentration up to 10 at. %. This experimental evidence confirms that increase in shrinkage rate is attributed to the increase in the amount of oxygen release. Generally, the additional charge of the substituent trivalent Yb for bivalent Ca is compensated by increasing Mn^{3+}, which perhaps increases the amount of oxygen released up to 0.5 at. % Yb-doped. Since ionic radius of Mn^{3+} cations are larger than Mn^{4+} cations, tolerance factor *t* deviated from unity which facilitates oxygen released. However compounds with Yb concentration above 10 at. % shows different behavior. This issue is investigated further by the Iodometric titration method (Section 5.6).

The magnification of Figure 5-25 reveals that all ceramic compounds start to release oxygen at temperature more than 100°C, as illustrated in figure 5-26. This is an important experiment which demosntrates contribution of oxygen vacancies in bulk conductivty properties, as discussed in chapter 6.

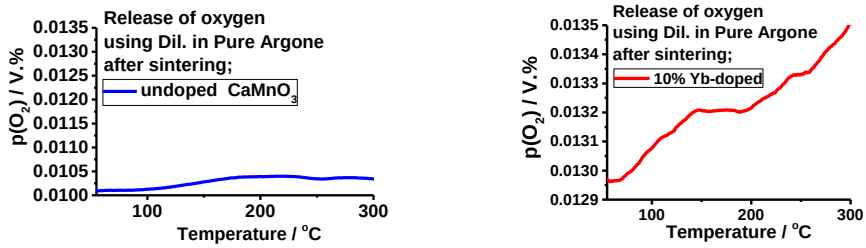

Figure 5-26: Release of O_2-gas, monitored by ZrO_2 oxygen sensor, increases at temperature above 100 °C for all compounds.

5.5.3 Thermogravimetric analysis (TGA)

A comparison of the mass loss for grinded sintered stoichiometric $CaMnO_3$ and $Yb_xCa_{1-x}MnO_3$ ceramics (0 to 10 at. % Yb-addition) in a wide $p(O_2)$ range from 10^{-1} down to 10^{-19} MPa at a constant temperature of 750°C is shown in figure 5-27. In all investigated compounds mass loss increases gradually by decreasing $p(O_2)$. Details are discussed further below.

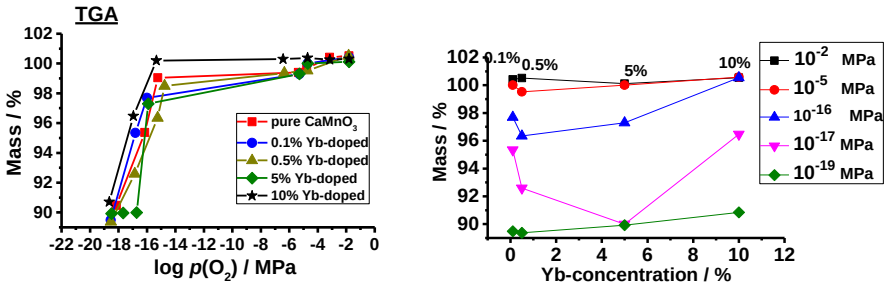

Figure 5-27: TGA experiment as a function of $p(O_2)$ in the range from 10^{-1} to 10^{-19} MPa for 0 to 10 at. % Yb-doped $CaMnO_3$ (left side) and comparison of the mass loss in dependence of donor level in different $p(O_2)$ region (right side).

- ***p*(O$_2$) >10^{-16} MPa**

Figure 5-27 (right side) demonstrates that the mass loss gradually increases with decreasing $p(O_2)$ for compounds with 0.1 at % and 0.5 at. % of Yb addition. However the compound with 5 at % Yb-content shows a relatively smaller decrease and 10 at. % is almost constant down to 10^{-16} MPa.

In the case of pure $CaMnO_3$, as discussed in section 5.3.3, it seems that oxygen vacancies increase at $p(O_2)$-values lower than 10^{-2} MPa . With further reduction, oxygen anions are shifted from their initial sites and form secondary phases Ca_2MnO_4 and $CaMn_2O_4$. The secondary phases which are accumulated in grain boundaries form barriers temporarily. As a result relatively lower concentration of oxygen will be released as gas phase from grain to grain boundaries and to the atmosphere. Accordingly, mass loss is negligible in the intermediate region ($10^{-14} < p(O_2) < 10^{-6}$ MPa) for pure $CaMnO_3$.

On the other hand, the Yb-doped compositions contain more amount of Mn^{3+} cations (0.645 Å) which have relatively larger ionic radius compared to Mn^{4+} cations (0.53 Å) in $CaMnO_3$. This results in a low tolerance factor *t* deviating from unity. The low *t* value results in more distorted structure and larger cell volume for this oxygen deficient perovskite structure than that from pure $CaMnO_3$. Accordingly, perhaps relatively larger amount of secondary phases such as $CaMn_2O_4$ and Ca_2MnO_4 are formed at even higher $p(O_2)$ (> 10^{-6} MPa) compared to pure $CaMnO_3$. These two phases are observed after sintering in 1%O_2+99%O_2 and in pure Ar ($\approx p(O_2) < 10^{-2}$), as discussed in section 5.5.1. Therefore, the composition with 10 at. % Yb shows relatively constant mass loss even at high $p(O_2)$.

- **$p(O_2) < 10^{-16}$ MPa**

The effect of oxygen released is more pronounced at much lower volume of $p(O_2)$ (e.g. < 10^{-16} MPa). The compound with 5 at. % Yb possesses the highest mass loss in 10^{-17} MPa. This indicates that the compound lost the largest oxygen concentration compare to the others. The mass loss due to oxygen deficiency also increases up to 9 wt.% for 10 at.% Yb-addition in 10^{-19} MPa.

In order to find the origin of this effect, XRD-measurements were carried out after TGA experiments in the highly reducing regime of $p(O_2) \approx 10^{-19}$ MPa. Details are listed in table 5-8. All of the investigated compounds contain the main phase of $Ca_{0.5}Mn_{0.5}O$ with cubic crystalline structure which is also known as $CaMnO_2$. The structure of $CaMnO_2$ is characterized by oxygen vacancies generated by the reduction of Mn^{4+} in $CaMnO_3$ to Mn^{3+} in $CaMnO_{2.5}$ [156]. Further reduction forms Mn^{2+} cations in $CaMnO_2$. Accordingly, the drastic mass loss at high reduction region is due to the phase change and thus structure change from orthorhombic to cubic symmetry ($CaMnO_2$).

Table 5-8: X-ray determination of the structural changes of 10% Yb-doped sample after TGA in $p(O_2)_{end} = 10^{-19}$ MPa.

Sample after TGA	Crystal structure	Amount	PDF Card
$Yb_{0.1}Ca_{0.9}MnO_3$	$Ca_{0.5}Mn_{0.5}O$ ($CaMnO_2$) /cubic	main phase	PDF #4-7-8378
	Yb_2O_3	low amount	PDF #4-14-9540
	Mn_3O_4	very low amount	PDF #4-18-7078

It can be concluded that, in the $p(O_2)$ around 10^{-16} MPa another phase ($CaMnO_{2.5}$) is formed. This phase possesses the same atomic arrangement as $CaMnO_3$ except the oxygen defect-sites in the crystal structure. The oxygen vacancies could facilitate ion transport [155, 8]. Therefore, in further reduction region lower than 10^{-16} MPa a drastic mass loss is attributed to the release of higher amount of oxygen which causes a change in structure from orthorhombic to cubic symmetry in $CaMnO_2$ phase.

Further study was carried out in the next section by means of iodometric titration in order to investigate the effect of different Yb-doping concentrations and stoichiometric $CaMnO_3$ compounds on the behavior of oxygen vacancy formation as well as on Mn-valence.

5.6 Determination of the average Mn-valence-state by iodometric titration

5.6.1 Stoichiometric and Yb-doped $CaMnO_3$

In the present thesis, iodometric titration experiments were performed in order to determine the average Mn valency and corresponding oxygen content of the compounds $Yb_xCa_{1-x}MnO_{3\pm\delta}$ (0 to 10 at. % Yb-addition). Experimental details were described in section 4.2.8. All compounds before iodometric titration were sintered in pure oxygen in 1350°C and then grinded into powder. The amounts of average Mn-valance, corresponding oxygen content and a comparison of different Mn-valency states for investigated compounds are listed in tables 5-9 and 5-10.

Table 5-9: Results of iodometric titration for the compounds $Yb_xCa_{1-x}MnO_3$ (0 to 10 at. % Yb-addition) after sintering at 1350°C in pure oxygen.

Yb-doped concentration / %	Molar Mass/ (g/mol)	powder/mg	NaS_2O_3 (EXP.)	Mn-valence	Oxygen content
0	143.014	20.333	28.650	4.015	3.0075
0.1	143.147	20.167	28.017	3.989	2.9951
0.5	143.679	20.000	26.500	3.904	2.9547
1	144.344	20.100	28.650	4.057	3.0337
5	149.662	21.000	29.200	4.080	3.0651
10	156.310	20.267	24.803	3.913	3.0064

Table 5-10: Developed formula after iodometric titration for $Yb_xCa_{1-x}MnO_3$ (zero to 10% Yb-doped) at the sintering in pure oxygen and 1350°C.

Yb-doped concentration / %	Developed formula after iodometric titration
0	$Ca^{2+}\left(Mn^{4+}_{0.985}Mn^{5+}_{0.015}\right)O^{2-}_{3.0075}$
0.1	$Yb^{3+}_{0.001}Ca^{2+}_{0.999}\left(Mn^{4+}_{0.9893}Mn^{3+}_{0.0107}\right)O^{2-}_{2.9951}$
0.5	$Yb^{3+}_{0.005}Ca^{2+}_{0.995}\left(Mn^{4+}_{0.9045}Mn^{3+}_{0.0955}\right)O^{2-}_{2.9547}$
1	$Yb^{3+}_{0.01}Ca^{2+}_{0.99}\left(Mn^{4+}_{0.9425}Mn^{5+}_{0.0574}\right)O^{2-}_{3.0337}$
5	$Yb^{3+}_{0.05}Ca^{2+}_{0.95}\left(Mn^{4+}_{0.9198}Mn^{5+}_{0.0801}\right)O^{2-}_{3.0651}$
10	$Yb^{3+}_{0.1}Ca^{2+}_{0.90}\left(Mn^{4+}_{0.9128}Mn^{3+}_{0.0872}\right)O^{2-}_{3.0064}$

Iodometric titration resulted in 98.5 at. % for the concentration of tetravalent manganese Mn^{4+} and 1.5 % for Mn^{5+} in undoped $CaMnO_3$ compound. Accordingly, the composition of the sample is $Ca^{2+}\left(Mn^{4+}_{0.985}Mn^{5+}_{0.015}\right)O^{2-}_{3.0075}$.

In the close-packed $CaMnO_3$ perovskite structure at temperatures at which crystal growth (sintering) takes place, a Schottky equilibrium between the concentrations of

cation and anion vacancies is established. Schottky-type disorder reaction is expressed as:

$$nil \rightleftarrows V''_{Ca} + V'''_{Mn} + 3V^{\bullet\bullet}_{O} \qquad \textbf{Eq. 5-2}$$

Its mass-action expression is formulated as follows:

$$[V''_{Ca}][V'''_{Mn}][V^{\bullet\bullet}_{O}]^3 = K_S \qquad \textbf{Eq. 5-3}$$

Where K_S is the mass-action constant.

Accordingly, if mobile cation vacancies are present in relevant amounts the Schottky equilibrium strongly suppresses the oxygen vacancy concentration [6] in order to maintain equilibrium.

In addition, at $p(O_2)$ above that at the stoichiometric composition, compounds take up an excess of oxygen to maintain equilibrium [8, 157]. Since cation vacancies are one of the preferred intrinsic ionic defects in close packed structure $YbCaMnO_3$ they are expected to be a product of the oxidation reaction during sintering in pure oxygen:

$$\frac{3}{2}O_2 \rightleftarrows 3O^{X}_{O} + V'''_{Mn} + V''_{Ca} + 6Mn^{\bullet}_{Mn} \qquad \textbf{Eq. 5-4}$$

where $Mn^{\bullet}_{Mn}$ denotes Mn^{5+}_{Mn} with one hole.

As listed in table 5-9, increasing Yb-dopant concentration from 0 at. % to 0.5 at. % reduces both Mn-valence from 4.015 to 3.904 and oxygen content from 3.0075 to 2.9547, respectively. This reveals the increase for Mn^{3+} cations. In fact, substituent trivalent Yb for bivalent Ca (i.e. donor doping) is compensated by increasing cation vacancy concentration of Mn^{4+}.

For doped compounds with 1 at. % and 5 at. % of Yb-addition strange behavior is observed. Iodometric titration shows Mn-valency above 4+ and also oxygen content of the mentioned compounds increases from 2.9547 to 3.0651, respectively. This reveals that mobile cation vacancies reach to the critical amount where the Schottky equilibrium occurs (Eq. 5-2). Therefore compound must reduce the oxygen vacancy concentration in order to maintain equilibrium. Hence, according to Eq. 5-4 maybe compounds uptake oxygen and thus Mn^{5+} causes the iodometric titration shows Mn-valence more than 4+ ($Mn^{4+\alpha}$).

It is observed that at 10 at. % Yb-doped the Mn-valence and oxygen content both decrease slightly down to 3.913 and 3.0064, respectively. The oxygen vacancy of this compound is approximately similar as pure calcium manganite, while its Mn^{3+}-valence is much larger. It seems large Yb-content causes the concentration of Mn^{3+} cations significantly increase and thus enhances the oxygen vacancy concentration. Besides, at sintering in oxidizing regime the Schottky equilibrium (Eq. 5-2) suppresses some of the oxygen vacancy concentration with up taking oxygen. Therefore, totally the oxygen content is at stoichiometric state and the value for δ equal zero approximately.

The results obtained from the iodometric titration (Figure 5-28) are in excellent agreement with dilatometry (Figure 5-24). It confirms that the behavior of shrinkage rate depends on the amount of oxygen loss. In other words, increase or decrease in shrinkage rate is due to the amount of oxygen that is lost or taken up by compounds, respectively. It is also observed that the variation in oxygen loss depends on the Yb-dopant concentration and Mn-valance.

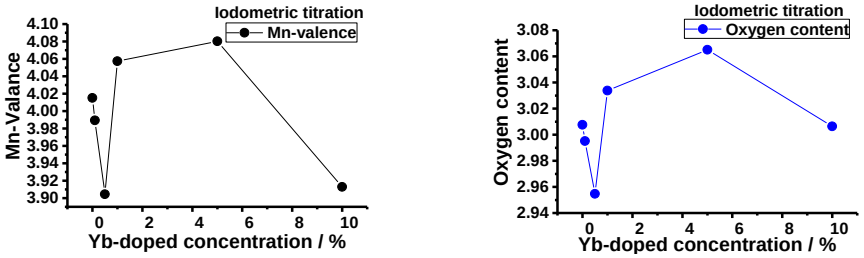

Figure 5-28: Average Mn-valance (left side) and corresponding oxygen content (right side) for $Yb_xCa_{1-x}MnO_3$ (0 to 10% Yb-doped) calculated from iodometric titration method.

5.6.2 Non-stoichiometric $CaMnO_3$: Ca- & Mn-excess

Iodometric titration measurements were performed for non-stoichiometric compounds $CaMnO_3$ structured at 1350C in pure oxygen with manganese and calcium excess, respectively. The amounts of average Mn-valance, corresponding oxygen content, and the other details used for iodometric titration are listed in tables 5-11.

Table 5-11: Results of iodometric titration for $CaMnO_3$, $CaMn_{1.01}O_3$, $Ca_{1.01}MnO_3$.

compound	Molar Mass (g/mol)	powder/mg	NaS_2O_3 (EXP.)	Mn-valence	Oxygen content
Stoichiometric	143.014	20.333	28.650	4.015	3.0075
Mn-excess	143.562	21.050	29.525	4.014	3.0271
Ca-excess	143.414	21.100	31.875	4.164	3.0921

The developed formula for compounds with Mn-excess and Ca-excess is determined respectively as:

Mn-excess: $Ca^{2+}(Mn^{4+}_{0.9859}Mn^{5+}_{0.141})_{1.01}O^{2-}_{3.0271}$

Ca-excess: $Ca^{2+}_{1.01}(Mn^{4+}_{0.8359}Mn^{5+}_{0.1641})O^{2-}_{3.0921}$

According to the iodometric measurement, oxygen content of compound contain Mn-excess is slightly lower than that of compound with Ca-excess. Therefore as mentioned in previous section the amount of shrinkage for Mn-excess compound should be larger. The dilatometry measurements (Figure 5-16) confirms this and shows the shrinkage of compound $CaMn_{1.01}O_3$ is about 9% larger than $Ca_{1.01}MnO_3$.

5.7 Conclusions

Comprehensive study on the effect of different calcination and sintering conditions in dependence of temperature *T* and partial pressure of oxygen $p(O_2)$ for stoichiometric, non-stoichiometric (Ca-excess and Mn-excess) and 0 to 10 at. % of Yb-doped $CaMnO_3$ ceramics were performed for the first time.

The results reveal that calcination conditions have an important role on the physical properties such as, surface morphology and shrinkage behavior of the ceramic even after sintering under identical conditions. For instance, the SEM images (Figure 5-29) show compounds calcined in pure O_2 and different temperatures (1000 and 1200 °C). Both compounds were sintered at the same condition in low $p(O_2)$ gas compositions (1% O_2 + 99% Ar). It is observed that samples which were calcined at higher temperature often cracked while the other samples are relatively stable.

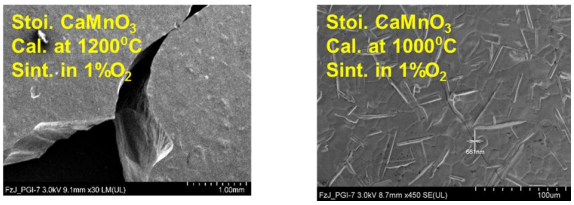

Figure 5-29: The significant effect of calcination conditions on the ceramic preparation for two compounds of $CaMnO_3$ calcined in 100% O_2 at different temperatures (1000 and 1200 °C). Ceramic pellets were sintered at the same condition in 1% O_2 + 99% Ar and at 1350°C. Compound calcined at higher temperature broke into pieces while at lower temperature only contains smaller cracks of around 600 nm in width.

The average grain size of compounds calcined at lower temperatures is about half of the compounds calcined at higher temperatures, which are referred to as fine powders and coarse powders in present thesis, respectively. This is one of the most important parameters for a good densification of ceramic pellet.

One of the most important achievements in this chapter is the finding the way for reducing crack formation that occurs during sintering. In some cases, crack-free ceramics could be prepared by adding a sufficient required amount of dopant, by adjusting the lower calcination temperature (as mentioned above), gas composition types, and heating/cooling rates. It is found that, the gas composition used for the sintering process is a main factor to obtain ceramics with a high density. Specially high partial pressure of oxygen is favorable which results in densities of more than 98% of the theoretical value only. While, the density of compounds sintered in 100% argon has 90% of theoretical value. It is observed that compounds that were cooled down at higher rate contains cracks on the surface, while the other one with lower cooling rate shows crack free ceramic, as illustrated in figure 5-30.

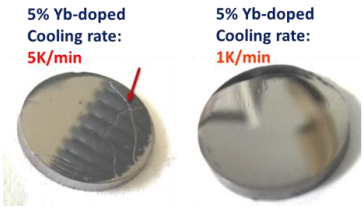

Figure 5-30: The importance of cooling rate in sintering process. Compound cooled down slowly shows crack-free ceramics.

SEM-experiments show that grains are visible clearly for the compounds sintered at high $p(O_2)$ gas compositions (100% O_2), while at low $p(O_2)$ gas compositions (1% O_2 + 99% Ar) some needle-like shaped crystals also formed in the ceramic pellets. However, compounds sintered in 100% Ar do not possess any polygonal grain on the surface but only needle shaped crystals. The grain size was determined by the intercept method from SEM-images. The average grain size of the non-stoichiometric compounds $Ca_{1.01}MnO_3$ and $CaMn_{1.01}O_3$ estimated from SEM measurement are around 17 µm and are slightly larger than the stoichiometric one (≈ 8 µm). The average grain size of the Yb-doped compounds decreases from 11µm for 0.1 at. % Yb-content to 3µm for 10 at. % of Yb dopant concentration.

Characterization results obtained by EDX, XRD, and Raman spectroscopy are in excellent agreement. These experiments enlighten that sintering at low $p(O_2)$ gas compositions (1% O_2+99% Ar) and pure argon causes a phase decomposition from $CaMnO_3$ to Ca_2MnO_4 which manifests itself in the appearance of needle-like shaped crystals precipitating on the surface and of $CaMn_2O_4$ and $CaMnO_3$ for the matrix around these precipitates. Such phase decomposition is observable for all the investigated compounds sintered under low $p(O_2)$.

Dilatometry analysis shows that the physical properties of compounds depend on different calcination temperatures and gas compositions. A reduction of the onset temperature for sintering and shrinkage by around 60 K occurs for compounds sintered at lower $p(O_2)$ in comparison to those sintered at higher $p(O_2)$. This could be due to the release of more amount of oxygen from compound during sintering at low oxygen concentration. Furthermore, it is found that compounds sintered at lower $p(O_2)$ gas composition (1%O_2 + 99%Ar) and 100% Ar show two peaks for maximum shrinkage rate at temperatures around 1000 and 1200°C respectively (differential sintering). Consequently, from dilatometry results and from phase purity and crystallography measurements it is concluded that the origin of the second peak is attributed to decomposition of $CaMnO_3$ into two phases Ca_2MnO_4 and $CaMn_2O$ during sintering at low $p(O_2) < 10^{-2}$ MPa.

Regarding non-stoichiometric samples, the experiments demonstrate that the structure, surface morphology of the compounds and dilatometry results are substantially

dependent on the gas composition during the sintering process. However, Ca- or Mn-excess does not have any significant effect. The measurement of oxygen release during sintering in the dilatometer by monitoring the partial pressure of oxygen in dependence of temperature shows approximately the same behavior for Ca- and Mn- excess.

With respect to ceramics $Yb_xCa_{1-x}MnO_3$ (0 to 10 at. % Yb-content) all the compounds were sintered in a furnace first and then investigated by dilatometry analysis in wide temperature range from room temperature to around 1400°C. This accurate investigation on the behavior of the sintered compounds in particular regarding to behavior of oxygen release in dependence of temperatures is extremely important for electrical measurements. It is observed that at high $p(O_2)$ by increasing the doping concentration from 0 to 10 at. % Yb the temperature where shrinkage starts increases gradually from 960 to 1100°C and the maximum shrinkage temperature enhances from 1100 to 1300°C, respectively. However, the maximum shrinkage rate only shows a negligible variation from around 0.07 to 0.09%/min. Moreover, measuring the ambient gas composition with regard to the oxygen content using a ZrO_2 oxygen sensor during annealing in the dilatometer from room to elevated temperatures up to around 1400°C reveals that samples start to release O_2-gas from 100°C upwards.

A comparison of iodometric titration and dilatometry experiments confirms that increase or decrease in shrinkage rate is due to the amount of oxygen that is lost or taken up by the compounds, respectively. It is also observed that the variation in oxygen loss depends on the Yb-doped concentration and Mn-valency.

Iodometric titration reveals that increasing the Yb-dopant concentration from 0 at. % to 0.5 at. % reduces both Mn-valency and oxygen content. In fact, substitution of Yb^{3+} for Ca^{2+} (i.e. donor doping) is compensated by increasing cation vacancy concentration of Mn^{4+}. This increase the concentration of Mn^{3+} cations. However, by adding more amount of Yb above 0.5 at. % up to 5 at. % the cation vacancy concentration reach a critical point where Schottky equilibrium takes place. Accordingly, the compounds must reduce the oxygen vacancy concentration in order to maintain equilibrium. Therefore, perhaps compound uptakes oxygen and thus Mn^{5+} cations are formed. As a result the iodometric titration shows Mn-valency above 4+ ($Mn^{4+\alpha}$) and oxygen content above 3. The oxygen content observed by iodometric titration for compounds with 10 at. % of Yb

addition is approximately the same as pure $CaMnO_{3.0075}$, while its Mn^{3+}-valence is relatively larger. It seems that a larger amount of Yb addition increases the concentration of Mn^{3+} cations significantly. Due to the larger ionic radius of Mn^{3+} (0.64 Å) than that of Mn^{4+} (0.53 Å) [41] positions of oxygen ions in the lattice might be shifted and perhaps this leads to relatively easier oxygen release. Besides, at sintering in oxidizing regime the Schottky equilibrium suppresses some of the oxygen vacancy concentration. Therefore, the value for δ equal zero approximately, while still the concentration of Mn^{3+} cations is relatively much more than Mn^{5+} cations. Therefore Iodomometric titration analysis shows Mn-valence less than 4+ for 10 at. % Yb-content.
XRD-measurements show that with increasing Yb-dopant concentration the volume of the crystallographic unit cell increases slightly which is due to the increase in the amount of Mn^{3+} cations with larger ionic radius compared to Mn^{4+} cations. These experiments in combination with Iodometric titration analysis reveal an important issue. It can be clearly understood that however some of the compounds show manganese valence state above 4+, the mixture of all three valance states of manganese Mn^{3+}, Mn^{4+} and Mn^{5+} occur in equilibrium for $Yb_xCa_{1-x}Mn^{4\pm\alpha}O_{3\pm\delta}$ according to the disproportional equation, expressed as:

$$2Mn^{4+} \rightleftharpoons Mn^{3+} + Mn^{5+}$$

Consequently, these investigations reveal that the oxygen content and concentration of charge carriers can be adjusted by adding specific amount of dopant.

Thermogravimetric analysis (TGA) at 750°C and in a wide range of $p(O_2) \approx 10^{-1}$ to 10^{-20} MPa demonstrates significant results, as follows:

- **$p(O_2) > 10^{-16}$ MPa**

It is observed that mass loss gradually increases with decreasing $p(O_2)$ for compounds with 0.1 at % and 0.5 at. % of Yb addition. However compounds with 5 at % Yb-content show a relatively smaller decrease and 10 at. % Yb is almost constant down to 10^{-16} MPa. It is suggested that this negligible mass loss (plateau state in TGA diagram) is perhaps due to this fact that with decreasing $p(O_2)$ oxygen vacancies increase and secondary phases $CaMn_2O_4$ and Ca_2MnO_4 are formed. The secondary phases which concentrated in grain boundaries temporarily form barriers to migration of oxygen ions. Accordingly the

amount of oxygen released to the atmosphere will be reduced. This assumption was further elucidated by measurements of DC-conductivity dependence of temperature and oxygen partial pressure in chapter 7.

- **$p(O_2) < 10^{-16}$ MPa**

At lower values of $p(O_2)$ (e.g. < 10^{-16} MPa) the effect of oxygen released is noticeable. This indicates that the compounds release large oxygen concentrations. XRD-measurements which were carried out after TGA experiments in highly reducing regime of $p(O_2) \approx 10^{-19}$ MPa reveal the origin of this effect. All of the investigated compounds contain the main phase of $CaMnO_2$ with cubic crystalline structure. Accordingly it is suggested that at $p(O_2)$ around 10^{-16} Mpa a new phase $CaMnO_{2.5}$ is formed with orthorhombic structure and Mn^{3+} valance state. Defect-sites (oxygen vacancies) in this crystal structure could facilitate ion transport for oxygen migration. Therefore with further reduction relatively higher amount of oxygen vacancies leads to the reduction of Mn^{3+} to Mn^{2+} that forms the cubic phase $CaMnO_2$. Accordingly, the drastic mass loss at high reduction region is due to the phase change and thus structure change from orthorhombic to cubic symmetry.

A comparison of TGA-experiments and DC-conductivity measurements reveals important factors about charge carriers and electrical transport mechanism, which are discussed in chapter 7.

6 Electronic characterization: impedance data analysis

This chapter aims to provide a comprehensive overview on the role of bulk conductivity contributions in compounds of the composition $Yb_xCa_{1-x}MnO_3$ (0 to 10 at. % Yb-dopant concentration). For this purpose, in-situ impedance spectroscopy was successfully employed at different temperatures (-100 to 300°C) and frequencies (1Hz to 1 MHz). Experimental measurements and theoretical simulations were performed in order to investigate the effect of grain boundaries and eventual ionic and electronic contribution to the electrical properties of quaternary oxide ceramic $Yb_xCa_{1-x}MnO_3$.

Theory as well as practical aspects of complex impedance analysis is described in chapter 3 and section 4.3.1, respectively. Here, the experimental results are discussed.

6.1 Complex impedance analysis

Semicircle shaped curves are observed in complex impedance plot (Nyquist plot) for pure $CaMnO_3$ ceramics in the temperature range from -100 to 300°C. As demonstrated in figure 6-1.a, the total impedance decreases with the increasing temperature. To obtain more details about this reduction, the real (*Z'*) and imaginary part (*Z''*) of impedance were plotted in two separate diagrams in dependence of frequency at different temperatures (Figure 6-1b and c).

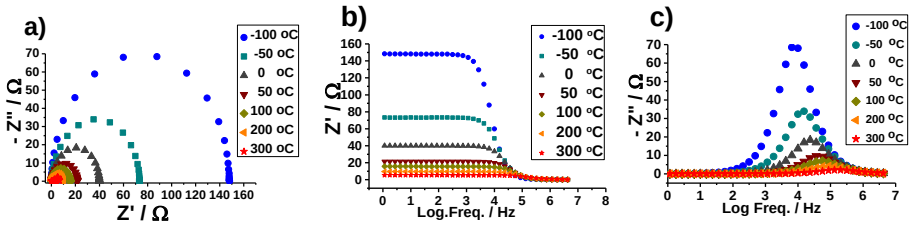

Figure 6-1: a) Impedance plot and frequency dependence of b) real and c) imaginary part of impedance for pure $CaMnO_3$ at different temperatures.

Obtaining higher value for *Z'* at lower frequencies and low *Z'* value at higher frequencies indicates the presence and disappearance of space charge polarization, respectively. Since charge carriers contributing the polarizability are not able to align with rapidly changing external electric field at higher frequencies.

It is also observed that the curve of *Z'* at low frequencies shows negative temperature coefficient of resistance type behavior. At high frequencies, the value of *Z'* merged by

increasing temperatures. This behavior may be due to the thermally activated charge carriers hopping conduction mechanism at elevated temperatures.

As shown in figure 6-1c, at first the *Z″* value increases, reach a peak Z''_{max} and then decreases with frequency as well as temperature. If hopping frequency of localized electrons become equal to the frequency of applied electric field the maximum peak appear [158]. At higher frequencies dipoles are not able to align fully with the electric field variations. Therefore space charge polarization and orientation polarizability released at higher frequencies and thus relaxation occurs.

It is illustrated that increasing temperature from -100 to 300°C shifted the relaxation peak of *Z″* from around 10^4 Hz to higher frequency about 10^5 Hz, respectively. In fact, increasing temperature enhances the rate of hopping of electrons and ions which causes more diffusion through compounds. Some of the charge carriers are trapped because of lacking enough energy to overcome the barrier. These charge carriers have enough energy to align with fast changing filed at higher frequencies and thus restore the space charge polarization.

6.2 Dielectric properties

6.2.1 Frequency dependence of dielectric permittivity

A surprisingly very large dielectric permittivity $\varepsilon' \approx 10^5$ at 10^3 Hz is obtained for compounds $Yb_xCa_{1-x}MnO_3$ (0 to 10 at. % Yb-addition). The large dielectric value is due to the Maxwell-Wagner polarization because of existing grains and grain boundaries in $CaMnO_3$ ceramics. In fact, the polarization forms internal barrier capacitors at the grain boundaries.

Figure 6-2 shows the frequency dependence of the dielectric permittivity for stoichiometric $CaMnO_3$ over a wide temperature range from -100 to 300°C. Increasing frequency from 10^3 to 10^6 HZ decreases dielectric permittivity by factor of around 1.4 and 2.6 at low and high temperatures, respectively. It is due to the phase shift between the dipole alignment and the electric field at high frequency and reduction in polarization.

Lower amount of permittivity at low temperatures is due to the less contribution of charge carrier to space charge polarization. Since space charge polarization is strongly temperature dependent, the permittivity increases with raising temperature. With

enhancing temperature more charges (electrons and ions) reach the grain boundaries and space charge polarization increases and thus enhance dielectric permittivity.

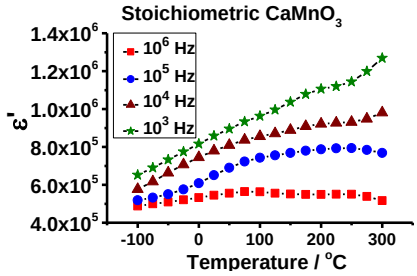

Figure 6-2: Frequency dependence of real permittivity ε' of stoichiometric $CaMnO_3$ at temperature range of -100 to 300°C.

6.2.2 The effect of Yb-contents on dielectric permittivity as a function of temperature

A comparison of real dielectric $\varepsilon'(\omega)$ properties as a function of temperature for different Yb-dopant concentrations is shown in figure-6-3. Pure $CaMnO_3$ shows only one dielectric relaxation. However, two relaxations are formed with increasing the Yb-dopant concentration. There is an exception for 5 at. % Yb-content. This compound shows one relaxation peak. The reason of these variable behavior is discussed below.

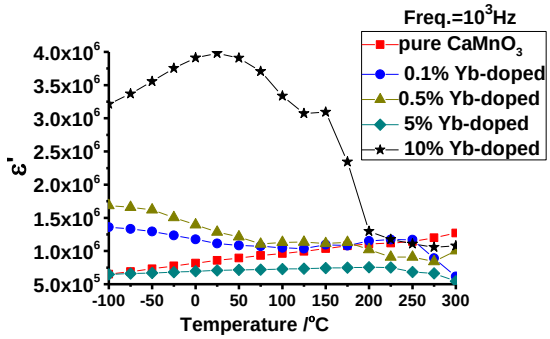

Figure 6-3: A comparison of real dielectric permittivity $\varepsilon'(\omega)$ as a function of temperature (-100 to 300°C) for different Yb-dopant concentration (0 to 10 at. % Yb-conent).

It is found that, the first relaxation observed at low temperatures is probably due to charge carriers contributing to space charge polarization. Increasing temperature initially causes more migration of electrons and ions through compound. The energy of these charges is not adequate to enhance the rate of hopping, and thus they are not

able to participate in conductivity. However, these charge carriers trap within the grain boundaries and enhance the dielectric value. Above certain temperature the charge carriers possess enough energy, then rate of hopping and conductivity increases. Therefore dielectric permittivity decreases and first relaxation occurs.

The first relaxation peak is not observable for compound pure $CaMnO_3$. It is due to the strong lattice-charge carrier interaction at low temperatures. However, the maximum dielectric peak increases with adding dopant concentration. Since the binding energy of donor electrons is relatively low, with slight increase in temperature they can get enough energy for hopping and participating in polarization. However, again compound with 5 at.% Yb addition shows strange behavior, the first relaxation peak is not observable in this compound. According to the iodometric titration analysis (Section 5.6.1, Table 5-9) the manganese cations possess valance state of above 4+ ($Mn^{4+\alpha}$) and oxygen vacancies are reduced for mentioned compound. As discussed in section 5.6.1 the formation of oxygen vacancies (due to the creation of Mn^{3+} with adding Yb-dopant) and depletion of those (because of Schottky equilibrium) coexist in the compounds. This reveals that compound with 5 at. % Yb-content contains mixture of three manganese valence sates of Mn^{3+}, Mn^{4+} and Mn^{5+}. It is well known that the possibility of electron hopping over e_g states of Mn^{3+} and Mn^{4+} is more than hopping of holes over empty e_g states between Mn^{4+} and Mn^{5+}. Accordingly, charge carrier hopping mechanism reduces and thus relatively lower amount of charge carriers move to the grain boundaries. As a result, polarization decreases for compounds contain 5 at.% of Yb addition.

The certain relaxation temperature depends on the Yb-dopant concentration. It is shifted from around -100°C to the higher temperature about 25°C with increasing Yb-content from 0.1 at. % up to 10 at.%. Since the amount of Mn^{3+} and thus charge carrier concentration enhances with increasing the Yb-content. As a result more amount of those participate in polarization and dielectric value increases. Consequently, this experiment reveals that the first relaxation presumably depends on the amount of Mn^{3+} in compound and thus contribution of polarons in conductivity.

It is also observed that the dielectric value for compound with 10 at. % Yb-content increases four times larger than that for pure $CaMnO_3$. According to the Iodometiric titration (section 5.6.1, Table 5-9), the oxygen vacancy concentration of this compound

is approximately similar as that for pure $CaMnO_3$, while its Mn^{3+}-valence is much larger. As discussed above disproportion reactions occur. As a result, charge-ordering is possible due to strong interactions between charge carriers. Charge-ordering here means an ordered arrangement of Mn^{3+}, Mn^{4+} and Mn^{5+} cations. Therefore polarization increases and thus dielectric permittivity enhances drastically for 10 at. % of dopant concentration at low temperatures.

On the other hand, at higher temperatures above 100°C the second peak is formed. It is believed to be due to thermally activated oxygen vacancies at higher temperature. This issue is confirmed with dilatometry measurement (Figure 5-26, Section 5.5.2) and release of oxygen is monitored precisely by ZrO_2 oxygen sensor. In fact, with raising temperature above 100°C more oxygen ions can hop from lattice site to lattice site, and reach to the grain boundaries. The more oxygen vacancy concentration, the larger amount of electrons in grain boundaries. Therefore space charge polarization increases. However, at temperature above 150°C conductivity increase in grain boundaries because the rate of hopping increases and charges can over come the potential barrier. Accordingly, the second relaxation is formed.

The results of the above presented experiments are in excellent agreement with the results of the temperature dependence of the resistive components calculated based on the equivalent circuit model. These are discussed in following section.

6.3 Electrical equivalent circuit model

All samples were modeled in terms of an electrical equivalent circuit for two, three, and four *RC*-elements ($R1|C1+R2|C2+R3|C3+R4|C4$). Depending on the temperature the best fit was selected. Complex impedance measurement of stoichiometric $CaMnO_3$ at 150°C is demonstrated in figure 6-4 (left side). An excellent agreement between experimental result and theoretical calculations is obtained which illustrates that the suggested equivalent circuit clearly describes the electrical properties of the ceramic sample. The variation in resistive components in dependence of temperature (0 to 300°C) is shown in figure 6-4 (right side) for pure $CaMnO_3$. It is observed that at temperature more than 100°C the complex impedance for stoichiometric $CaMnO_3$ can be modeled well with four *RC* elements.

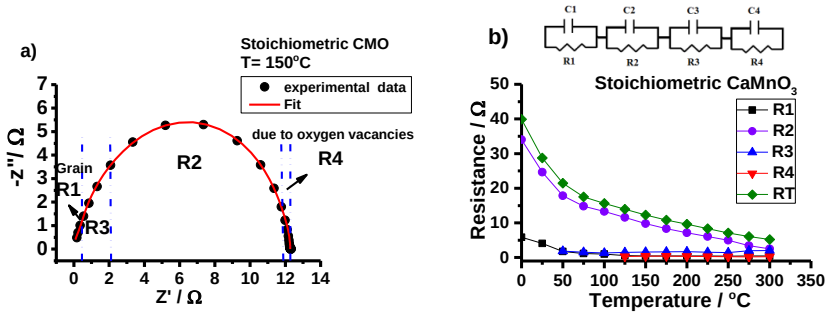

Figure 6-4: a) Complex impedance spectra of stoichiometric $CaMnO_3$ at 150°C containing: experimental data (symbols), and theoretical data (solid line), specified R1-R4 based on the respective equivalent circuit, b) temperature dependence of resistive components (0 to 300°C) based on the respective equivalent circuit.

A previous report [132] revealed that each semicircle can be fully observed on the impedance diagram only if the relaxation frequency that ascribes each semicircle differs at least by three orders of magnitude otherwise semicircles present some degree of overlapping. Accordingly, the present complex impedance diagram in figure 6-4 apparently shows one semicircle, but in fact there is an overlap of semicircles. The distinction is clearly observed in a theoretical model in terms of four electrical equivalent circuits.

During sintering of polycrystalline ceramics at very high temperatures cation and anion vacancies may be formed through Schottky disorder [6]. In the case of slow cooling, the concentration of oxygen vacancies decreases near the grain boundaries, since oxygen ions have larger diffusivity than the other ions. This leads to the formation of cation vacancies [95], V''_{Ca} and/or V''''_{Mn}, along the grain boundaries. They act as acceptor-dopant and trapping areas of electrons.

In the double-Schottky-barrier model, the majority charge carriers (i.e. electrons in the case of oxygen non-stoichiometry compound $CaMnO_{3-\delta}$ or donor doped $CaMnO_3$) migrate from the grain interior to grain boundaries under applied an electric field. This causes high conductivity in the bulk. In the present thesis, the resistance contribution of grains is named “R1” and is specified in Figure 6-4a. The resistivity of grains (R1) is smaller than that of grain boundaries, since electronic charge carriers can move through the bulk easier than in the grain boundary. Generaly for ceramics at high frequencies grain boundary contribution to the electric response decreases. Since at the high

frequency range charge carriers are not able to align with fast changing electric filed and thus space charge polarization in grain boundaries decreases.

With increasing temperature, the hopping rate of some of the charge carriers enhances. These charge carriers are able to overcome the barrier, easily flows to the next grain and participate in conduction mechanism. The resistance created by this type of thermally exited charge carriers is named “R2”. The resistance “R2” decreases by increasing temperature. Since with raising temperature the number of charge carriers increase and thus conductivity enhances.

On the other hand, some of the other charge carriers which do not have enough energy for hopping are trapped by acceptor states in the grain boundary core region. This gives rise to a negative net-charge of the grain boundary core and adjacent space charge layers in the grains where the negative charge carriers are depleted. Here space charge polarization occurs which causes resistance named “R3”. Therefore, the resistance “R3” depends on polarization in grain boundaries. This issue is proved in the following sections by comparing the temperature dependence of dielectric measurement and the resistive components calculated based on the equivalent circuit model.

With raising temperature above 100°C more oxygen ions can hop from lattice site to lattice site, and reach to the grain boundaries. Therefore a fourth contribution to the electric response is observable above 100°C. This resistance is named “R4”. This issue is confirmed with monitoring the release of oxygen precisely by ZrO_2 oxygen sensor (Figure 5-26, Section 5.5.2). It is illustrated that the amount of released oxygen increases at temperature above 100°C. The resistance “R4” is observed above 100°C for all of the investigated doped and undoped ceramic samples. In addition a second increase in dielectric value (Figure 6-3) observed above 100°C. Consequently, these results confirm the suggstion for contribution of resistance “R4” in conductivity mechanism arising due to the contribution of more diffused oxygen vacancies.

6.4 The effect of temperature on the fitted electrical equivalent circuit

Complex impedance data were fitted in terms of an electrical equivalent circuit for all doped and undoped ceramic samples in a wide range of temperature (-100 to 300°C). It is observed that with raising temperature additional *RC* elements must be used in the electrical equivalent circuit model. As an example, temperature dependence of the

complex impedance diagrams for 10 at. % Yb-content are shown in figure 6-5. The experimental data and theoretical curves based on the respective equivalent circuit are in excellent agreement.

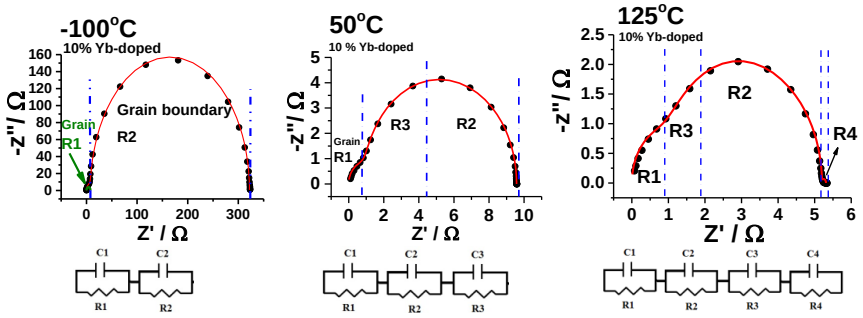

Figure 6-5: Temperature dependence of electrical equivalent circuits with the corresponding complex impedance analysis at different temperatures: -100, 50, and 125 °C, for 10% Yb-doped $CaMnO_3$. Symbols denote experimental data and solid lines indicate theoretical curves based on the respective equivalent circuit.

It is found that complex impedance can be fitted well only with two *RC* elements at low temperature ≈ -100°C. As temperature increases to 50°C the third R_3C_3 element is needed to fit well the experimental data. As explained in section 6.3, some of the charge carriers, which do not have enough energy for hopping, are trapped in the grain boundary core region. This gives rise to the space charge polarization which forms the resistance "R3" and thus R_3C_3 element must be added.

At temperatures above 125°C R_4C_4 elements should be added. Since above 100°C more oxygen ions can hop from lattice site to lattice site, and reach to the grain boundaries. Therefore resistance "R4" is added due to the contribution of more diffused oxygen vacancies in conductivity mechanism.

6.5 The effect of different Yb-contents on resistance as a function of temperature

In ionic compounds, as explained in the previous section, charge carriers which affect the conductivity can be either intrinsic to their lattice as Mn^{3+} cations (by forming polarons) and oxygen ions (by leaving electrons and creating vacancies) or extrinsic due to the addition of dopant to pure compounds. At sufficiently high temperatures diffusion of ions increases. The charge carriers are able to overcome the barrier and under

applying an electric field they easily flow to the next grain and participate in conduction mechanism. As a result, by increasing temperature total resistivity decreases, as shown in figure 6-6.

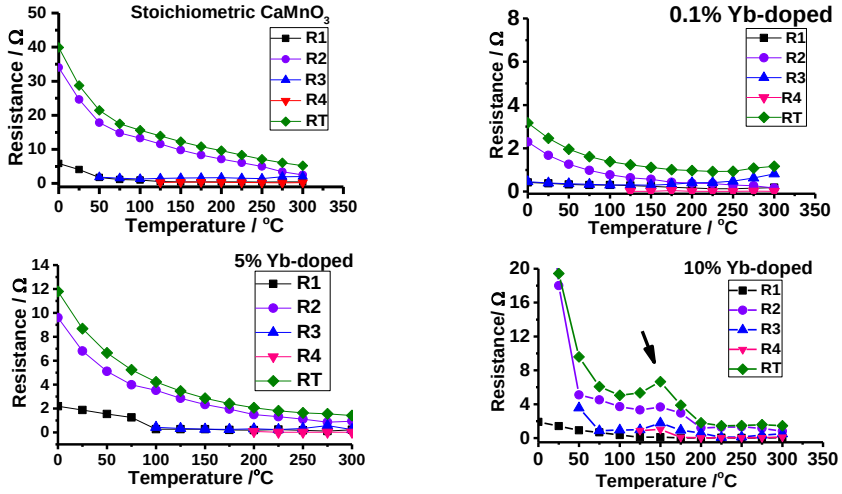

Figure 6-6: The effect of different Yb-contents on resistive components (R1-R4) as a function of temperature. The green curves indicate total resistance (RT).

An ionic compound with 0.1 at. % Yb-dopant concentration possesses a higher amount of oxygen vacant sites compared to pure $CaMnO_3$, as determined by the iodometric titration analysis (Section 5.6.1, Table 5-9). Therefore, by applying an electric field ions easily hop between pre-existing vacancies and this requires a much lower energy than creating a vacant site. The more Mn^{3+} cations in doped compound also form large amount of charge carries. Therefore, the conductivity of doped compounds is higher than that of pure $CaMnO_3$. It is observed that the resistance decreases drastically by factor of 10 at low temperature with doping only 0.1 at. % Yb. At higher temperatures the resistivity of pure $CaMnO_3$ is around 3 times higher than Yb-doped samples.

The additional charge of the substitution of 5 at. % Yb donor-dopant for bivalent Ca is compensated by the concentration of increasing cation vacancies. As described in section 5.6, to maintain the Shottky equilibrium (Eq. 5-2: $nil \rightleftarrows V''_{Ca} + V'''_{Mn} + 3V^{\bullet\bullet}_{O}$) oxygen vacancies are decreased. According to oxidation reaction (Eq.5-4: $\frac{3}{2}O_2 \rightleftarrows 3O^{X}_{O} + V'''_{Mn} + V''_{Ca} + 6Mn^{\bullet}_{Mn}$), Mn^{5+} cation concentration increase. Therefore, there

is a mixture of Mn^{3+}, Mn^{4+} and Mn^{5+} in the mentioned compounds. It is well known that the possibility of electron hopping over e_g states of Mn^{3+} and Mn^{4+} is more probable than hopping of holes over empty e_g states between Mn^{4+} and Mn^{5+}. Accordingly, charge carrier hopping mechanism reduces and thus relatively lower amount of charge carriers participate in conductivity. As a result, resistivity increase for compounds contain 5 at.% of Yb addition in comparison with compounds with 0.1 at % Yb-dopant concentration.

In the case of 10 at. % Yb-addition the concentration of Mn^{3+} cations exceeds a certain amount at which Mn^{3+}-Mn^{4+} states decrease. Therefore charge localization occurs which enhances the resistivity. A peak at 150°C is observed which is at the same temperature where second dielectric relaxation is formed (Figure 6-3). In addition, the forth RC element is added at above 100°C. These confirm the suggestion of diffusion of more oxygen ions from grain to grain boundaries with increasing temperature more than 100°C. More oxygen vacancies leave more electrons. Some of the charge carriers which do not have enough energy for hopping are trapped in the grain boundary core region. This forms space charge polarization which increases with raising temperature. Therefor resistance increases. However, at sufficiently high temperatures above 150°C the hopping rate of the charge carriers enhances and the conductivity increases. Accordingly, resistance decreases again.

6.6 Conclusions

In the present chapter, the effect of bulk conductivity contributions in compounds $Yb_xCa_{1-x}MnO_3$ (0 to 10 at. % Yb-dopant concentration) is observed by in-situ impedance spectroscopy at different temperatures (-100 to 300°C) and frequencies (1Hz to 1 MHz). These characterizations were accompanied by modeling of the compounds in terms of an electrical equivalent circuit. Accordingly, a comprehensive study on the role of grain boundaries and ionic and electronic contribution to the electrical properties of quaternary oxide ceramic $Yb_xCa_{1-x}MnO_3$ is demonstrated.

A large dielectric permittivity value ε' around 10^5- 10^6 is observed at frequency of 10^3 Hz. In fact, the polarization forms internal barrier capacitors at the grain boundaries which can be explained by Maxwell-Wagner polarization. With decreasing frequency from 10^6 to 10^3 HZ dielectric permittivity increases by a factor of around 1.4 and 2.6 at low and high temperatures, respectively. It is as expected due to the reduction in phase shift

between the dipole alignment and the electric field at low frequency and increase in polarization.

A comparison of the impedance measurements and iodometric titration experiments (Section 5.6, Table 5-9) reveals that the first dielectric relaxation probably depends on the amount of Mn^{3+} cations and thus contribution of polarons in conductivity. Since the first relaxation peak is not observed for compounds which contain Mn-valency above 4+ ($Mn^{4+\alpha}$), i.e. pure $CaMnO_3$ and compound with 5 at. % Yb-content. While the other compounds which possess Mn-valency below 4+ show this peak clearly. On the other hand, the second peak appears at temperatures above 100°C. Monitoring the released oxygen (Section 5.5, Figure 5-26) also shows clearly a release of oxygen above 100°C. Accordingly, the second peak is probably due to thermally activated oxygen vacancies. Increasing the amount of oxygen vacancy enhances electron concentration in grain boundaries. Therefore space charge polarization increase. However, at temperatures above 150°C the rate of hopping increases and charges can overcome the potential barrier. Consequently, the second relaxation is formed.

It is found that complex impedance for all investigated components at temperatures above 100°C can be modeled well with four parallel *RC* elements, i.e. *R*1*C*1+ *R*2*C*2+ *R*3*C*3+ *R*4*C*4. A novel schematic illustration based on the double-Schottky-barrier model for polycrystalline ceramics describes the resistance component R1 to R4 (Figure 6-7). According to this model cation vacancies which have been formed during the sintering process along the grain boundaries act as acceptor-dopants and trapping areas of electrons. (i) By applying an electric field the majority charge carriers (here means electrons) migrate from the grain interior to grain boundaries. This causes high conductivity in the bulk. In the present thesis, the resistance contribution of grains is named “R1”. (ii) With increasing temperature some of the charge carriers which possess enough energy are able to overcome the barrier, easily flows to the next grain and participate in conduction mechanism. Accordingly, resistance “R2” appears. (iii) Some of the charge carriers which do not have adequate energy are trapped and accumulated in grain boundaries. Therefore a space charge layer is formed which prevent excess amount of negatively charge carriers after equilibration of Fermi level. This type of charge carriers forms resistance “R3”. (iv) At T > 100°C oxygen vacancy concentration increases. Oxygen ion hop from lattice site to lattice site under the influence of an

electric field, and reach to the grain boundaries. The electrons which are left from oxygen vacancies form resistance R4.

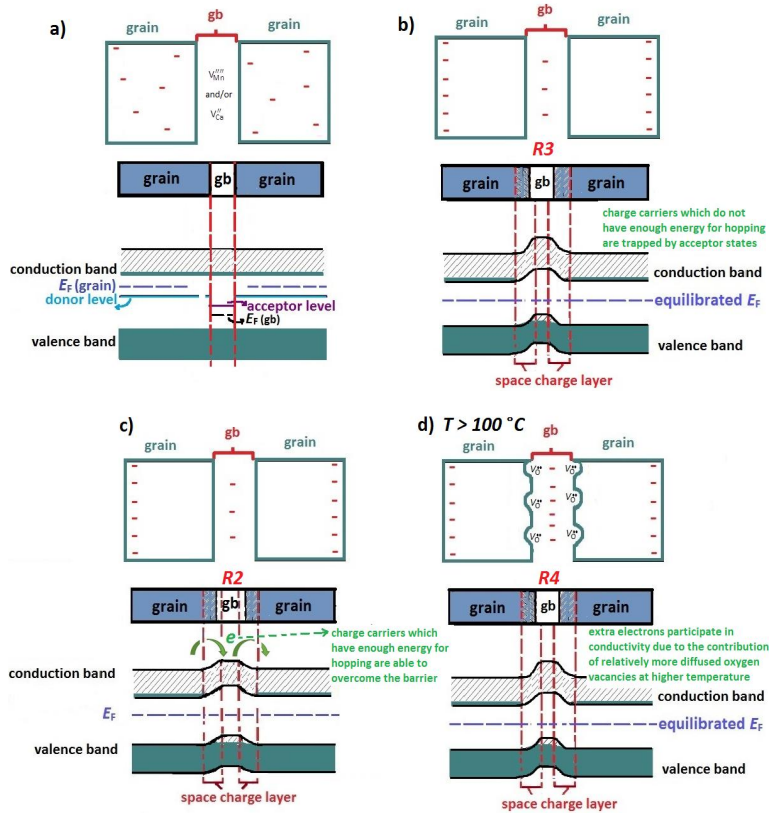

Figure 6-7: Schematic illustration based on the double-Schottky-barrier model for polycrystalline ceramic including a) donor-doped grains, an acceptor state grain boundary (gb), i.e., formation of cation vacancies (during sintering process) acting as acceptor-doped and trapping area of electrons, and b) under applying an electric field some of the charge carriers which do not have adequate energy are trapped and accumulated in gb. Therefore the space charge layer is formed and resistance "R3" appears. c) With increasing temperature, some of the charge carriers which possess enough energy are able to overcome the barrier, easily flow to the next grain and participate in conduction mechanism. Accordingly, resistance "R2" is formed. d) at T > 100°C oxygen vacancy concentration increases. Oxygen ion hop from lattice site to lattice site under the influence of an electric field, and reach to the grain boundary. The electrons left from oxygen vacancies form resistance "R4".

7 Electronic characterization: analysis of DC-conductivity

The electrical DC-conductivity of undoped $CaMnO_3$ and Yb-doped ceramics was investigated at a temperature of 750°C and the oxygen partial pressures were changed successively from 10^{-1} to 10^{-20} MPa. The dimensions of the rectangular shaped ceramic samples are around 4 x 0.7 x 10 mm^3. After each variation of the $p(O_2)$, the conductivity tended to a new equilibrium value. If the conductivity no longer changed with time, it was assumed that the state of equilibrium had been attained. This recorded process of adjustment provides conductivity curve in dependence of a wide range of $p(O_2)$. Afterwards, the equilibrium concentrations of the principal types of defects were calculated in undoped and doped compounds.

Defect chemical model for undoped and rare earth (RE^{3+}) doped $CaMnO_3$ is proposed in the present section. There are only a few reports with respect to undoped $CaMnO_3$ ceramics at high partial pressure of oxygen around 10^{-1} to 10^{-6} MPa [67], but lacking results in literature for the defect chemistry describing the type and behavior of defect concentration in detail specifically for n-type doped $CaMnO_3$ in a wide range of $p(O_2)$. The lack of information possibly is due to the crack formation or deformation of $CaMnO_3$ in to the powder during electrical measurement in the reduction region. This problem is successfully solved in the present thesis with systematic studies on preparation of ceramic samples as discussed in chapter 5.

7.1 The main reactions in defect chemical model

The dominating defects, ionic as well as electronic defects can be described in detail by comparison experimental results of DC-measurements with this theoretical model.

The main equilibrium reactions and their mass action expressions required to construct the defect diagram are described below:

- **Intrinsic Ionic disorder: Schottky disorder**

In the close-packed $CaMnO_3$ perovskite structure Schottky-type disorder is a predominant form of intrinsic ionic disorder.

$$nil \rightleftharpoons V''_{Ca} + V'''_{Mn} + 3V^{\bullet\bullet}_{O} \qquad \textbf{Eq. 7-1}$$

Its mass-action expression is formulated as follows:

$$[V''_{Ca}][V'''_{Mn}][V^{\bullet\bullet}_{O}]^3=K_S=K'_S\exp(-\frac{\Delta H_S}{k_B T}) \quad \textbf{Eq. 7-2}$$

Where K_S is the mass-action constant and K_S' is the entire mass-action constant except for the enthalpy term.

In the present thesis both Ca and Mn vacancies are considered, since two secondary phases of Ca-excess (Ca_2MnO_4) and Mn-excess ($CaMn_2O_4$) are observed in XRD measurements, as discussed in chapter 5. Defect chemical model is calculated with two assumptions. However, both methods lead to the same results. (i) It is possible to assume the same concentration for cation vacancies i.e., $[V''_{Ca}]=[V'''_{Mn}]$, since there is no preference for A sites and B sites and cation defects occur simultaneously. (ii) In the second method suggested in the present thesis, equations are calculated with the assumption of $[V''_{Ca}]\neq[V'''_{Mn}]$ and thus cation vacancy concentrations are formulated separately. It is found that in order to maintain equilibrium an average value for the $p(O_2)$-dependencies (slopes) of $[V''_{Ca}]$ and $[V'''_{Mn}]$ must be considered. The average value of the slops obtained by the second method is equal to the precise slope calculated by the first method. Consequently, the exponential terms will all remain the same either assume $[V''_{Ca}]=[V'''_{Mn}]$ or $[V''_{Ca}]\neq[V'''_{Mn}]$. A principle aspect in the second method is that it shows clearly that both cation defects behave dependently. Besides, it is possible to calculate their concentrations separately.

- **Intrinsic electronic defect: Thermal excitation of charge carriers**

It is related with the transition of electrons from the half-filled t_{2g} to the empty e_g band of Mn^{4+} ions. Therefore all three charged states, Mn^{3+}(Mn'_{Mn}), Mn^{4+} ($Mn^{\times}_{Mn}$), Mn^{5+} ($Mn^{\bullet}_{Mn}$) occur in equilibrium [67]. The reaction can be presented in terms of equilibrium:

$$2Mn^{\times}_{Mn} \rightleftharpoons Mn^{\bullet}_{Mn}+Mn'_{Mn} \quad \textbf{Eq. 7-3}$$

The mass-action expression is written as:

$$[Mn^{\bullet}_{Mn}][Mn'_{Mn}]=K_I \quad \textbf{Eq. 7-4}$$

It is reported that calculated values for enthalpy ΔH of Eq. 7-3 in the temperature range 220 - 550 °C is 78 kJ/mol (0.8 eV) which is essentially equal to the band gap (0.7 eV)

obtained in electron structure simulations for orthorhombic $CaMnO_{3-\delta}$ [67]. In comparison, bandgap for undoped $SrTiO_2$ is around 2.5 eV over temperature range of 1000°–1400°C [73].

- **Reduction reaction:**

If $p(O_2)$ is decreased below the value at the stoichiometric composition, the compound will lose a certain amount of oxygen in order to stay in equilibrium. This should results in the formation of oxygen vacancies. The reduction reaction is formulated as:

$$2Mn_{Mn}^{\times} + O_O^{\times} \rightleftarrows 2Mn_{Mn}' + V_O^{\bullet\bullet} + \frac{1}{2}O_2 \qquad \textbf{Eq. 7-5}$$

Its mass-action expression is written as:

$$[Mn_{Mn}']^2[V_O^{\bullet\bullet}] = K_n p(O_2)^{-1/2} \qquad \textbf{Eq. 7-6}$$

where the subscript "n" indicates nonmetal-deficient (anion defect and electrons) and n-type region. Generally, the concentration of regular oxygen $[O_O^{\times}]$ in the lattice is comparatively large relative to a small variation upon oxygen release. Therefore $[O_O^{\times}]$ is not significantly afected by the deviations from stoichiometry, so that it is included in the preexponential coefficient [8].

- **Oxidation reaction:**

At $p(O_2)$ above that of the stoichiometric composition, a compound must take up an excess of oxygen to maintain equilibrium. Since cation vacancies are one of the preferred intrinsic ionic defects, they are expected to be a product of the oxidation reaction [8, 157]:

$$\frac{3}{2}O_2 \rightleftarrows 3O_O^{X} + V_{Mn}'''' + V_{Ca}'' + 6Mn_{Mn}^{\bullet} \qquad \textbf{Eq. 7-7}$$

Its mass-action expression is formulated as:

$$[V_{Mn}''''][V_{Ca}''][Mn_{Mn}^{\bullet}]^6 = K_p p(O_2)^{3/2} \qquad \textbf{Eq. 7-8}$$

Where the subscript "p" represents p-type region where cation vacancies and holes are dominant defects.

According to mentioned mass action expressions above, all considerable charged defect species in $CaMnO_3$ in the Kröger-Vink notation can be formulated as general charge neutrality condition as follows:

$$[Mn'_{Mn}]+2[V''_{Ca}]+4[V''''_{Mn}]=2[V^{\bullet\bullet}_{O}]+[Mn^{\bullet}_{Mn}]+[D^{\bullet}] \qquad \textbf{Eq. 7-9}$$

The concentration of intrinsic defects, i.e. Mn vacancies $[V''''_{Mn}]$, Ca vacancies $[V''_{Ca}]$ oxygen vacancies $[V^{\bullet\bullet}_{O}]$, electrons $[Mn'_{Mn}]$, and holes $[Mn^{\bullet}_{Mn}]$ are determined by the defect equilibrium of investigated compound as will be indicated below. $[D^{\bullet}]$ represents the constant concentration of extrinsic defects (donor-doped), and it could be trivalent rare earth element, such as Yb^{3+} or Pr^{3+}, substituted in divalent Ca cation site and donates one electron. In the case of acceptor-doped compound, such as divalent Ca substituted in trivalent rare earth element, acceptor-dopant concentration [*A*'] is added to the left side of Eq. 7-9. All terms in eq. 7-9 are functions of temperature *T* and ambient oxygen partial pressure $p(O_2)$.

At intermediate temperatures, where the diffusivity of metal vacancies is too low to reach equilibration in reasonable time, the Schottky reaction is considered to be inactive. Therefore, the charge neutrality condition for donor-doped $CaMnO_3$ is expressed as:

$$[Mn'_{Mn}]=2[V^{\bullet\bullet}_{O}]+[Mn^{\bullet}_{Mn}]+[D^{\bullet}] \qquad \textbf{Eq. 7-10}$$

7.2 The defect chemistry modeling for undoped Calcium manganite

The influence of partial pressure of oxygen $p(O_2)$ on conductivity and the corresponding defect diagram for pure ceramic compound $CaMnO_3$ are shown in figure 7-1. Comparing the experimental results observed by DC-measurement with the corresponding defect diagram calculated based on the equilibrium concentrations reveal dominating defects, which are described further below.

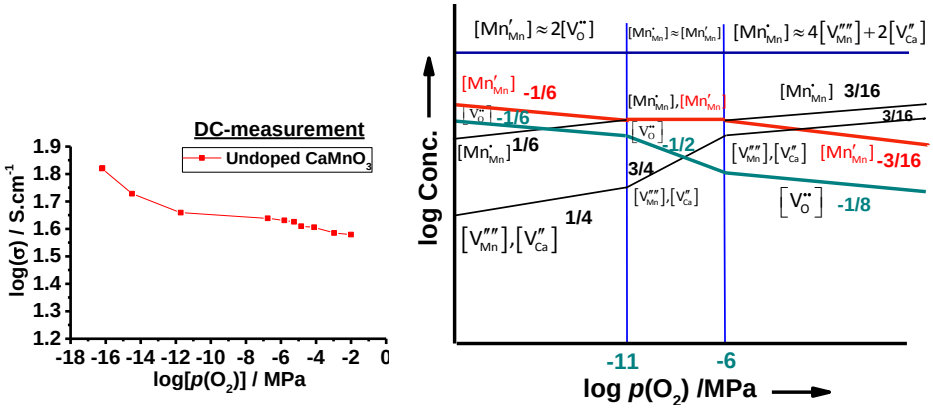

Figure 7-1: The effect of wide range of $p(O_2) \approx 10^{-1}$ to 10^{-16} MP on conductivity for undoped $CaMnO_3$ at 750°C observed by DC-measurement (left side), and corresponding defect diagram calculated based on the equilibrium concentrations reveals dominating defects (right side).

- **The highly oxidizing region: $p(O_2)>10^{-6}$**

A comparison of experimental data and theoretical calculation (Figure 7-1) reveals that in the oxidizing regime, the gradual decrease in conductivity by increasing partial pressure of oxygen above $p(O_2) \approx 10^{-6}$ MPa is due to the reduction in the concentration of conducting electrons $[Mn'_{Mn}]$.

The TGA experiments (Figure 5-12) are in excellent agreement with DC-measurements and demonstrate mass gain at the same $p(O_2)$ region (>10^{-6} MPa). As discussed in section 5.3.3, if $p(O_2)$ is sufficiently high, the oxidation reaction is major source of defects. In the case of active Schottky disorder, this reaction can increase the number of holes while the concentration of oxygen vacancies decreases, as formulated below.

$$\frac{3}{2}O_2 \rightleftarrows 3O_O^X + V_{Mn}''' + V_{Ca}'' + 6Mn_{Mn}^{\bullet} \qquad \textbf{Eq. 7-11}$$

Where $Mn_{Mn}^{\bullet}$ indicates Mn^{5+}.

Therefore with increasing $p(O_2)$ above 10^{-6} MPa the weight of the compound increases gradually because of up taking oxygen. Accordingly, concentration of conducting electrons $[Mn'_{Mn}]$ (i.e. the amount of Mn^{3+} cations) decreases while concentration of holes $[Mn^{\bullet}_{Mn}]$ (i.e. the amount of Mn^{5+} cations) increases. It is well known that the possibility of electron hopping over e_g states of Mn^{3+} and Mn^{4+} is more than hopping of holes over empty e_g states between Mn^{4+} and Mn^{5+}. As a result charge carrier hopping mechanism reduces and thus relatively lower amount of charge carriers participate in conductivity. Consequently, conductivity decreases.

To model appropriate defect chemical diagram, charge neutrality expression should be determined initially. According to the oxidation reaction (Eq. 7-7), concentration of electrons $[Mn'_{Mn}]$ in the *p*-type regime is negligible and thus charge neutrality expression is supposed to be:

$$[Mn^{\bullet}_{Mn}] \approx 4[V'''_{Mn}] + 2[V''_{Ca}] \qquad \textbf{Eq. 7-12}$$

As discussed in section 7.1 two methods are suggested for solving the equations:

Method 1: It is possible to assume $[V''_{Ca}] = [V'''_{Mn}]$ and insert it in Eq. 7-12. The concertation of cation vacancies, oxygen vacancies, electron and hole concentrations can be calculated with combination of the Schottky reaction (Eq. 7-2: $[V''_{Ca}][V'''_{Mn}][V^{\bullet\bullet}_{O}]^3 = K_S = K'_S \exp(-\frac{\Delta H_S}{k_B T})$), intrinsic electronic reaction (Eq. 7-4: $[Mn^{\bullet}_{Mn}][Mn'_{Mn}] = K_i$) and oxidation reaction (Ee. 7-8: $[V'''_{Mn}][V''_{Ca}][Mn^{\bullet}_{Mn}]^6 = K_p p(O_2)^{3/2}$), as expressed below:

$$[Mn^{\bullet}_{Mn}] \approx 6[V'''_{Mn}]$$

$$[V'''_{Mn}] = \left(\frac{K_p}{6^6}\right)^{1/8} p(O_2)^{3/16}$$

$$[V^{\bullet\bullet}_{O}] = \frac{(K_s)^{1/3}}{(K_p/6^6)^{2/3}} p(O_2)^{-1/8}$$

$$[Mn^{\bullet}_{Mn}] = \left(\frac{K_p p(O_2)^{3/2}}{[V'''_{Mn}][V''_{Ca}]}\right)^{1/6} = (36K_p)^{1/8} p(O_2)^{3/16}$$

$$[Mn'_{Mn}] = \frac{K_i}{(36K_p)^{1/8}} p(O_2)^{-3/16}$$

Method 2: It is assumed that $[V''_{Ca}] \neq [V'''_{Mn}]$. A combination of charge neutrality with the mass action expression of the oxidation reaction (Eq.7-8: $[V'''_{Mn}][V''_{Ca}][Mn^{\bullet}_{Mn}]^6 = K_p p(O_2)^{3/2}$) results in defect concentrations of cation vacancies vary as $[V''_{Ca}] \propto p(O_2)^{1/8}$ and $[V'''_{Mn}] \propto p(O_2)^{1/4}$. Therefore the average slope of both cation vacancy concentrations (or sum of two line) can be formulated as:

$$\text{Average slope of } [V''_{Ca}] \text{ and } [V'''_{Mn}] \propto p(O_2)^{3/16} \qquad \textbf{Eq. 7-13}$$

Concentration of oxygen vacancies $[V^{\bullet\bullet}_{O}]$ can also be calculated by inserting cation vacancy concentrations in the Schottky reaction (Eq. 7-2: $[V''_{Ca}][V'''_{Mn}][V^{\bullet\bullet}_{O}]^3 = K_S$) formulated as:

$$[V^{\bullet\bullet}_{O}] \propto \left(\frac{K_S}{p(O_2)^{3/8}} \right)^{1/3} \propto K_s^{1/3} p(O_2)^{-1/8} \qquad \textbf{Eq. 7-14}$$

The concentration of hole $[Mn^{\bullet}_{Mn}]$ is determined by combination of mass-action expression of oxidation reaction (Eq.7-8: $[V'''_{Mn}][V''_{Ca}][Mn^{\bullet}_{Mn}]^6 = K_p p(O_2)^{3/2}$) and charge neutrality expression (Eq. 7-12: $[Mn^{\bullet}_{Mn}] \approx 4[V'''_{Mn}] + 2[V''_{Ca}]$), which can be expressed as:

$$[Mn^{\bullet}_{Mn}] = \left(\frac{K_p p(O_2)^{3/2}}{[V'''_{Mn}][V''_{Ca}] \propto p(O_2)^{3/8}} \right)^{1/6} \propto K_p^{1/6} p(O_2)^{3/16} \qquad \textbf{Eq. 7-15}$$

The concentration of electrons $[Mn'_{Mn}]$ also is calculated by substituting $[Mn^{\bullet}_{Mn}]$ in intrinsic electronic defect mass action expression (Eq. 7-4: $[Mn^{\bullet}_{Mn}][Mn'_{Mn}] = K_I$). The concentration of electrons is calculated as follow:

$$[Mn'_{Mn}] \propto \frac{K_I}{K_p^{1/6}} p(O_2)^{-3/16} \qquad \textbf{Eq. 7-16}$$

As Figure 7-1 demonstrates, in the region of $p(O_2) > 10^{-6}$ conductivity decreases by increasing $p(O_2)$ with the slope around -0.03 which is lower than the calculated slope of -3/16. The difference perhaps is due to the temperature dependence of the carrier concentration. This illustrates that the Schottky reaction is slightly active at intermediate temperatures around 750°C in the region of $p(O_2) > 10^{-6}$ for pure $CaMnO_3$.

- **Intermediate region : $10^{-11} < p(O_2) < 10^{-6}$ MPa**

At $p(O_2)$ approximately between 10^{-6} MPa and 10^{-11} MPa (plateau-type region) the conductivity is around 47 $S \cdot cm^{-1}$ which seems to be almost independent of $p(O_2)$.

Such a plateau-like regime from 10^{-13} up to 10^{-6} MPa was observed by Daniels, et. al [9]. Katsu [83] also reported a nearly partial pressure independent of electron concentration region between around 10^{-12} MPa to 10^{-6} MPa theoretically for donor-doped $BaTiO_3$-based compositions. Both of these authors agree that the electron concentration is governed by the amount of donor addition and is not governed by the dominant donor-type oxygen vacancies. Because the donor concentration is independent of temperature and $p(O_2)$, electron concentration, and thus electrical conductivity should remain unchanged at this level. A question then arises, why the plateau region is observed in compound pure $CaMnO_3$ and why electron concentration is not governed by oxygen vacancies.

As discussed in chapter 5, two secondary phases $CaMn_2^{3+}O_4$ and $Ca_2Mn^{4+}O_4$ were observed clearly with XRD measurements (Figure 5-7) after sintering in $p(O_2)$ lower than 10^{-2} MPa (1% O_2 + 99% Ar and pure Ar). In addition, the TGA experiments (Section 5.3.3, Figure 5-12) illustrate that the weight of compound is almost constant at the same mentioned intermediate $p(O_2)$ region. It is found that weight resistant is due to formation of secondary phases which probably form temporary barriers to oxygen migration near grain boundaries. Therefore releasing oxygen and thus weight loss is negligible.

Accordingly, as shown in defect diagram, the oxidation process does not have considerable effects on electron and hole concentration in the intermediate region. Consequently, decreasing $p(O_2)$ from 10^{-6} down to 10^{-11} MPa yields to the plateau region in conductivity.

As shown in Figure 7-1 (right side), electron and hole concentrations do not depend on $p(O_2)$ at the intermediate region. Therefore the expression of charge neutrality is dominated by the intrinsic electronic defects:

$$[Mn_{Mn}^{\bullet}] \approx [Mn_{Mn}^{\prime}] \qquad \textbf{Eq. 7-17}$$

From Eq.7-5: $[Mn_{Mn}^{\bullet}][Mn_{Mn}']=K_I$, and 7-17, the concentration of electron holes is calculated as:

$$[Mn_{Mn}^{\bullet}] \approx [Mn_{Mn}']=K_I^{1/2} \qquad \textbf{Eq. 7-18}$$

Substituting this in Eq.7-6: $[Mn_{Mn}']^2[V_O^{\bullet\bullet}]= K_n p(O_2)^{-1/2}$, concentration of oxygen can be formulated as:

$$[V_O^{\bullet\bullet}]=\frac{K_n}{K_I} p(O_2)^{-1/2} \qquad \textbf{Eq. 7-19}$$

Concentration of cation vacancies can be calculated by inserting Eq. 7-18 in oxidation reaction Eq. 7-8, $[V_{Mn}'''']$ $[V_{Ca}'']$ $[Mn_{Mn}^{\bullet}]^6=K_p p(O_2)^{3/2}$, and can be expressed as:

$$[V_{Ca}''] \propto p(O_2)^{1/2}$$

$$[V_{Mn}''''] \propto p(O_2)$$

$$\text{Average slope of } [V_{Ca}''] \text{ and } [V_{Mn}''''] \propto p(O_2)^{3/4} \qquad \textbf{Eq. 7-20}$$

$$[V_{Ca}''][V_{Mn}''''] = \frac{K_p}{K_I^3} p(O_2)^{3/2} \qquad \textbf{Eq. 7-21}$$

According to the calculation above which are based on the equilibrium concentrations, by increasing $p(O_2)$ the cation vacancies increase with the average slope of 3/4, and oxygen vacancies decrease with the slope of -1/2.

- **The reduction region: $10^{-16} < p(O_2) < 10^{-11}$ MPa**

From $p(O_2) \approx 10^{-11}$ down to 10^{-16} Mpa, conductivity increases with decreasing $p(O_2)$. This is also in excellent agreement with TGA measurements, which show a slight increase in oxygen vacancy concentration after plateau region down to 10^{-16} MPa (Section 5.3.3, Figure 5-12). In fact compounds release oxygen in order to maintain equilibrium with ambient pressure. With decreasing $p(O_2)$ the concentration of oxygen vacancies increased and electron concentration enhance on the base of the reduction reaction and thus conductivity increases:

$$O_O^{\times} \rightleftarrows \frac{1}{2} O_2 + V_O^{\bullet\bullet} + 2e \qquad \textbf{Eq. 7-22}$$

Consequently, in this region, the oxygen vacancy term $2[V_O^{\bullet\bullet}]$ is dominant and charge neutrality estimated as:

$$[Mn'_{Mn}] \approx 2[V_O^{\bullet\bullet}] \qquad \textbf{Eq. 7-23}$$

Electron concentration $[Mn'_{Mn}]$ and oxygen vacancy concentration $[V_O^{\bullet\bullet}]$ show an additional increase with the slope of -1/6, which can be calculated by substituting the charge neutrality (Eq. 7-23) in reduction reaction (Eq. 7-6: $[Mn'_{Mn}]^2[V_O^{\bullet\bullet}]= K_n p(O_2)^{-1/2}$) and expressed as

$$n = (2K_n)^{1/3} p(O_2)^{-1/6} \qquad \textbf{Eq. 7-24}$$

$$[V_O^{\bullet\bullet}] = (\frac{K_n}{4})^{1/3} p(O_2)^{-1/6} \qquad \textbf{Eq. 7-25}$$

According to the Schottky disorder reaction (Eq. 7-2: $[V''_{Ca}][V'''_{Mn}][V_O^{\bullet\bullet}]^3=K_S$) when oxygen vacancies increase with reducing $p(O_2)$, concentration of cation vacancies should decrease with the average slope of 1/4 which can be formulated as:

$$[V''_{Ca}]=\frac{K_p(2K_n)^{2/3}}{K_I^2} p(O_2)^{1/6}$$

$$[V'''_{Mn}]=\frac{K_p(2K_n)^{4/3}}{K_I^4} p(O_2)^{1/3}$$

The average value of the slopes $[V''_{Ca}]$ and $[V'''_{Mn}] \propto p(O_2)^{1/4}$ **Eq. 7-26**

$$[V''_{Ca}][V'''_{Mn}]=\frac{4K_S}{K_n} p(O_2)^{1/2} \qquad \textbf{Eq. 7-27}$$

In this region, increasing electron will enhance conductivity slightly.

7.3 The influence of doping on conductivity: Yb-doped calcium manganite

As shown in figure 7-2, the DC-measurements were performed for ceramic compounds $Yb_xCa_{1-x}MnO_3$ (0 to 10 at. % Yb-addition) in order to investigate the conductivity dependence of partial pressure of oxygen in $p(O_2)\approx 10^{-1}$ down to 10^{-20} MPa and study the effect of doping concentration in conductivity. It is observed that the addition of Yb to the pure $CaMnO_3$ as a donor-dopant results in an increase of the conductivity in whole range of investigated $p(O_2)$. In fact, substitution of trivalent Yb for bivalent Ca is

compensated by increasing Mn^{3+} cations and thus creates a high carrier concentration of electrons (polarons). It makes easier the electron hopping between Mn^{3+} and Mn^{4+} sites which yields to the increase in conductivity. The conductivity value of undoped $CaMnO_3$ and 10 at. % Yb-dopant in $p(O_2) \approx 10^{-2}$ MPa is 38 and 175 S-cm^{-1} respectively, the logarithmic scale is shown in the figure 7-2 (left side).

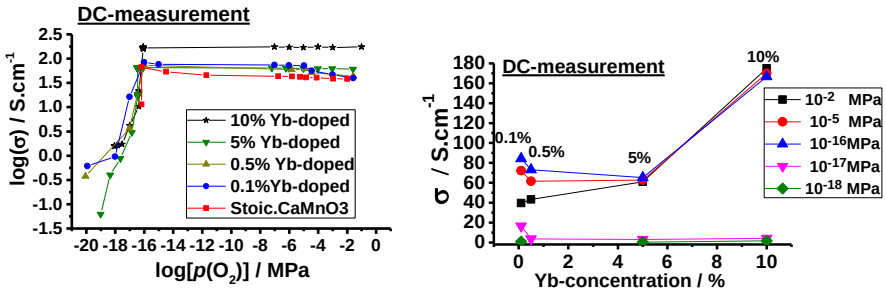

Figure 7-2: The effect of different Yb-content on conductivity as a function of $p(O_2)$ for compound $Yb_xCa_{1-x}MnO_3$ (0 to 10 at. % Yb-dopant concentration) at 750°C observed by DC-measurement (left side), and conductivity dependence of Yb-dopant concentration (0.1 to 10 at. % Yb) at different selected $p(O_2)$ (right side).

- **The oxidizing region: $p(O_2) > 10^{-16}$ MPa**

Figure 7-2 (right side) shows that with decreasing $p(O_2)$ from 10^{-2} down to 10^{-16} MPa conductivity increases for 0.1 at. % and 0.5 at % Yb-content. In fact in mentioned $p(O_2)$ region oxygen vacancies increase with decreasing $p(O_2)$ which add more charge carriers and thus enhance the concentration of Mn^{3+}. Therefore the number of Mn^{3+}-Mn^{4+} chains increase and conductivity enhances. However, the conductivity for compound with 5 at. % and 10 at. % Yb-content are almost constant in mentioned region. The origin of relatively constant conductivity is discussed below.

- **The plateau region**

As described in the previous section, if at high $p(O_2)$ region the conductivity increases with decreasing $p(O_2)$, this indicates n-type conductivity. Accordingly, compound with 0 at. % up to 0.5 at. % Yb- content clearly show n-type conductivity. In contrast, for samples with 5 at. % Yb-content the slope is negligible and for 10 at. % Yb-addition it is approximately plateau.

As discussed in the previous section, TGA experiments (Section 5.3.3, Figure 5-12) illustrate almost constant values in the intermediate $p(O_2)$ region. It is found that weight resistant is due to the fact that deviated oxygen anions participate in the formation of secondary phases $CaMn_2O_4$ and Ca_2MnO_4. Therefore releasing oxygen and thus weight loss is negligible and does not have considerable effects on electron and hole concentration in the intermediate region. Consequently, for pure $CaMnO_3$ decreasing $p(O_2)$ from 10^{-6} down to 10^{-11} MPa yields to the plateau region in conductivity.

The Mn^{3+} cations (0.645 Å) in Yb-doped compounds have relatively larger ionic radius compared to Mn^{4+} cations (0.53 Å) in $CaMnO_3$. A low tolerance factor *t* deviated from unity distorts the structure. Accordingly, perhaps secondary phases such as $CaMn_2O_4$ and Ca_2MnO_4 are formed even at higher $p(O_2)$ compare to the pure $CaMnO_3$. Therefore with increasing dopant concentration the plateau region is extended from 10^{-6} MPa for pure $CaMnO_3$ to 10^{-5} MPa for 0.1 at. % up to 0.5 at % Yb, and to lower than 10^{-3} MPa for 5 at. % and 10 at % Yb-addition.

- **The reduction region: $p(O_2) < 10^{-16}$ MPa**

On the other hand, with further reduction lower than 10^{-16} MPa conductivity decreases for all compounds. According to the TGA experiments (Figure 5-27) the compounds show large amount of oxygen released in $p(O_2) < 10^{-16}$ MPa. As shown in XRD measurement (Section 5.5.3, Table 5-8), the main phase detected by XRD is $Ca_{0.5}Mn_{0.5}O$ with cubic crystalline structure which also known as $CaMnO_2$. The structure of $CaMnO_2$ is characterized by oxygen vacancies generated by the reduction of Mn^{4+} in $CaMnO_3$ to Mn^{3+} in $CaMnO_{2.5}$ [156] and then under highly reduction regioin reduced to Mn^{2+} in $CaMnO_2$. Accordingly, the decrease in conductivity at high reduction region could be due to the charge localized ordering in cubic symmetry ($CaMnO_2$). Charge localization due to the ordered oxygen vacancies for $CaMnO_2$ structure has been reported previously [159,160].

Since with further reduction lower than 10^{-16} MPa $CaMnO_{2.5}$ and $CaMnO_2$ phases are formed, compound contains high amount of Mn^{3+} and Mn^{2+} in mentioned region. As a result, the number of Mn^{3+}-Mn^{4+} chains decrease and hence conductivity decreases drastically. Accordingly, the nonlinear conductivity property for different Yb-dopant

concentration is due to the different amount of Mn^{3+}-Mn^{4+} chains in the compounds. Phase transition obtained for $CaMnO_3$ is shown in figure 7-3.

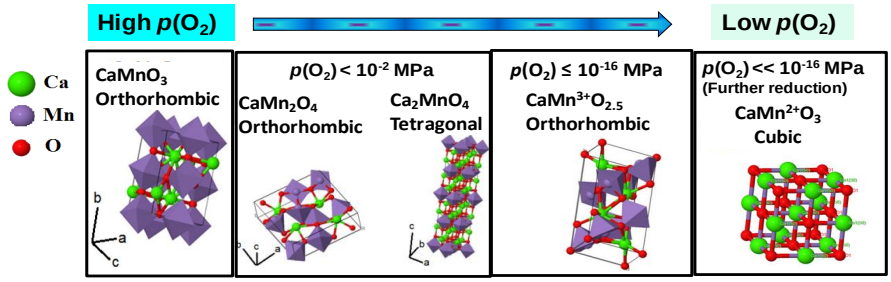

Figure 7-3: Phase transition observed for $CaMnO_3$ from pure oxygen down to 10^{-19}MPa. The phase $CaMnO_{2.5}$ is suggested at around 10^{-16}MPa or below, since it has similar atomic arrangement as $CaMnO_3$ while it has large amount of oxygen-defect sites which facilitate ion transport in reduction region.

In conclusion, a comparison of the present experimental data with those reported by Wang et. al [161] is shown in figure 7-4. Data are in well agreement. The author reported that in the electron-doped $CaMnO_3$ system, when the electron concentration exceeds a certain magnitude, charge ordering or local charge ordering arises which increases the resistivity.

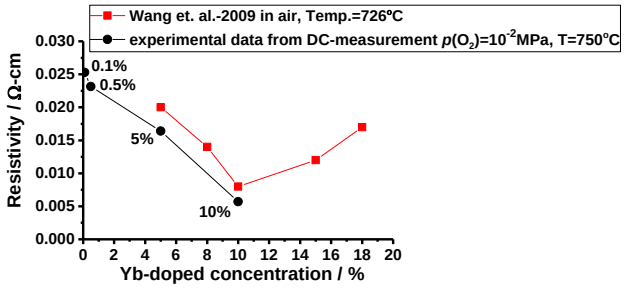

Figure 7-4: A comparison of the resistivity dependence of different Yb-dopant concentration reported by Wang et. al. [161] and the experimental data obtained in the present thesis.

The experiments in the present thesis clearly reveal that localization of the charge carriers not only depends on the amount of Yb-dopant concentration but also it is significantly affected by the variation of partial pressure of oxygen. With reducing $p(O_2)$ down to 10^{-16} MPa conductivity increases, while it decreases by further reduction below

10^{-16} MPa. In fact reducing gas composition leads to the phase change from orthorhombic to cubic symmetry which reduces the conductivity drastically due to charge localization.

7.3.1 The effect of oxygen vacancies on conductivity

In order to clarify the effect of oxygen vacancies on conductivity some of the data were selected from DC-conductivity measurements (Figure 7-2) and TGA-measurements (Figure 5-27) and plotted in different bar charts, as shown in figure 7-5.

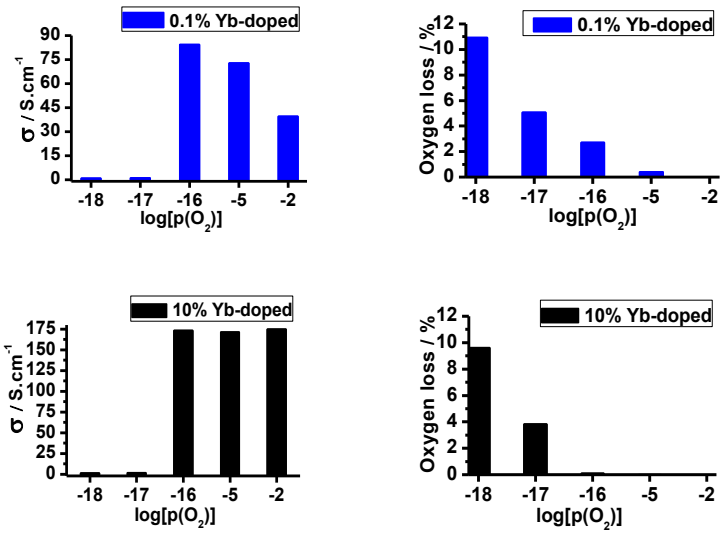

Figure 7-5: The effect of oxygen vacancies on conductivity, $p(O_2)$ dependence of conductivity obtained from the DC-measurements and the amount of oxygen loss selecting from TGA-measurements for 0.1 at. % Yb concentration (Blue bar) and 10 at. % Yb addition (Black bar).

It is observed that for compounds with 0.1 at. % Yb addition, conductivity increases with decreasing $p(O_2)$ down to 10^{-16} MPa. The TGA measurements in the mentioned $p(O_2)$ region show increase in oxygen loss, which probably indicates that oxygen vacancies are increasing. Therefore conductivity increase, since it depends on oxygen vacancy concentration. In the case of 10 at. % Yb-dopant concentration, no detactable oxygen loss is observed down to 10^{-16}MPa and conductivity also is constant. Therefore two experimental data obtained from different methods are in agreement. However below 10^{-16} MPa drastic decrease in conductivity is observed and the TGA measurements show

significant increase in oxygen loss. In fact, at high reduction region around 10^{-18} MPa large resistance around 10^4 Ω was observed after 1 ½ day. The interesting issue is that this process is reversible, i.e. with increasing $p(O_2)$ resistance R decreases fast. A resistance value of around 7 Ω is observed by keeping the sample at $p(O_2)= 10^{-1}$ MPa over night. However after that R will decrease very slowly (Figure 7-6). The origin of drastic change in conductivity and oxygen loss below 10^{-16} MPa could be due to a phase transition as explained in the previous section.

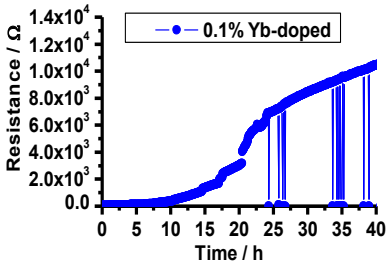

Figure 7-6: Time dependence of resistance obtained from the DC-measurements and large resistance value around 10^4 Ω after 40 h.

7.4 The defect chemistry modeling for donor-doped calcium manganite

7.4.1 Low doping level: 0.1 at. % Yb-dopant concentration

The predominant defects expected for the compound with 0.1 at. % Yb-content in dependence of $p(O_2)$ can be derived by a comparison of experimental data of conductivity with the proposed defect diagram, as shown in figure 7-7.

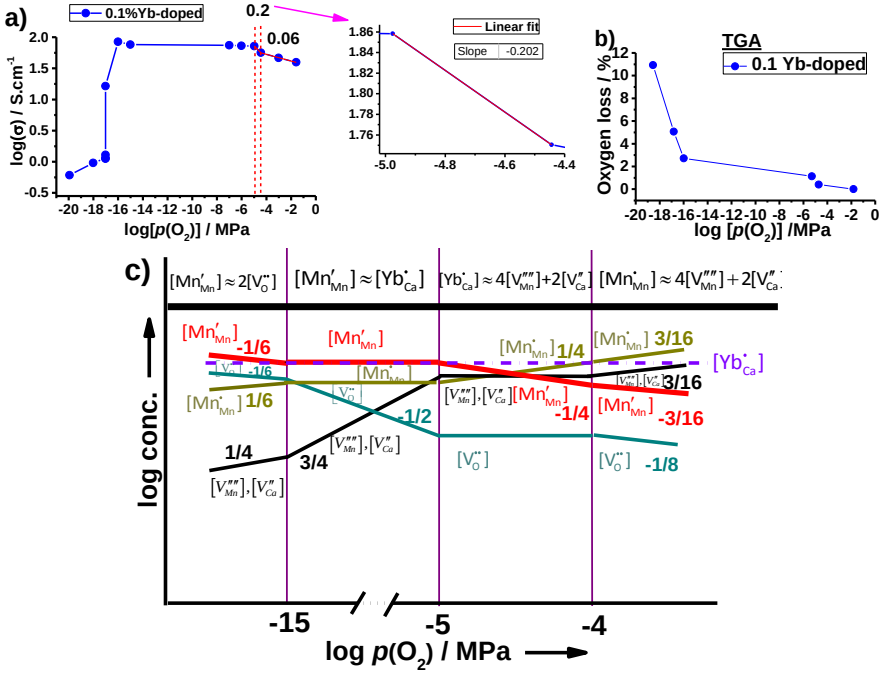

Figure 7-7: a) The conductivity as a function of $p(O_2)$ for the compound $Yb_{0.001}Ca_{0.999}MnO_3$ at 750°C observed by DC-conductivity measurement with specified value of the slopes, b) Oxygen loss as a function of $p(O_2)$ measured by TGA experiments for the same compound at the same temperature and c) corresponding theoretical defect diagram calculated based on the equilibrium concentrations.

The calculation is described as follows providing the mentioned defect diagaram for donor doped $Yb_xCa_{1-x}MnO_3$.

- **High oxidation region: $p(O_2) > 10^{-4}$ MPa**

The TGA experiments (Figure 7-4b) are in excellent agreement with the DC-measurements and demonstrate mass gain with increasing $p(O_2)$. As discussed in section 7.2, if $p(O_2)$ is sufficiently high, the oxidation reaction is major source of defects. In the

case of active Schottky disorder, this reaction can increase the number of holes while the concentration of oxygen vacancies decreases, as formulated below.

$$\frac{3}{2}O_2 \rightleftarrows 3O_O^X + V_{Mn}''' + V_{Ca}'' + 6Mn_{Mn}^{\bullet} \qquad \textbf{Eq. 7-28}$$

Where $Mn_{Mn}^{\bullet}$ indicates Mn^{5+}.

Therefore with increasing $p(O_2)$ above 10^{-4} MPa the weight of the compound increases gradually because of the take up of oxygen. Consequently, the concentration of conducting electrons $[Mn_{Mn}']$ decreases and thus conductivity is reduced.

Therefore charge neutrality can be approximated by:

$$[Mn_{Mn}^{\bullet}] \approx 4[V_{Mn}'''] + 2[V_{Ca}''] \qquad \textbf{Eq. 7-29}$$

Combing charge neutrality with the mass action expression of the oxidation reaction (Eq. 7-8: $[V_{Mn}'''][V_{Ca}''][Mn_{Mn}^{\bullet}]^6 = K_p p(O_2)^{3/2}$) results in the defect concentrations of cation vacancies ($[V_{Ca}''] \propto p(O_2)^{1/8}$ and $[V_{Mn}'''] \propto p(O_2)^{1/4}$). Therefore the average slope of both cation vacancy concentrations is 3/16.

Concentration of oxygen vacancies $[V_O^{\bullet\bullet}]$ can also be calculated by inserting the concentrations of cation vacancies mentioned above in the Schottky reaction (Eq. 7-2: $[V_{Ca}''][V_{Mn}'''][V_O^{\bullet\bullet}]^3 = K_S$) which can be formulated as:

$$[V_O^{\bullet\bullet}] = \left(\frac{K_S}{[V_{Ca}''][V_{Mn}'''] \propto p(O_2)^{3/8}}\right)^{1/3} \propto K_s^{1/3} p(O_2)^{-1/8} \qquad \textbf{Eq. 7-30}$$

Substituting concentrations of cation vacancies in the oxidation reaction (Eq.7-8: $[V_{Mn}'''][V_{Ca}''][Mn_{Mn}^{\bullet}]^6 = K_p p(O_2)^{3/2}$) leads to the concentration of electron holes, which can be expressed as:

$$[Mn_{Mn}^{\bullet}] = \left(\frac{K_p p(O_2)^{3/2}}{[V_{Mn}'''][V_{Ca}''] \propto p(O_2)^{3/8}}\right)^{1/6} \propto K_p^{1/6} p(O_2)^{3/16} \qquad \textbf{Eq. 7-31}$$

According to the intrinsic electronic defect reaction (Eq. 7-4: $[Mn_{Mn}^{\bullet}][Mn_{Mn}'] = K_I$) the concentration of electrons is calculated as follows:

$$[Mn_{Mn}'] \propto \frac{K_I}{K_p^{1/6}} p(O_2)^{-3/16} \qquad \textbf{Eq. 7-32}$$

Comparing these theoretical calculations with experimental results for 0.1% Yb-doped $CaMnO_3$ elucidates that Schottky disorder is apparently more active in this region

compared to undoped $CaMnO_3$. Since conductivity increases with decreasing $p(O_2)$ by slope of around -0.06 which is slightly less than calculated slope (≈ 0.18) in Kröger-Vink diagram.

- **Impurity controlled region (Ionic compensation): $10^{-5}<p(O_2)< 10^{-4}$**

In the region of $10^{-5} <p(O_2)<10^{-4}$, the conductivity of $Yb_{0.001}Ca_{0.999}MnO_3$ increases with the slope close to the expected value of 1/4 in modified Kröger-Vink diagram. It confirms the ionic compensation of the extrinsic donors by cation vacancies and thus the lattice charge-neutrality condition is expressed as:

$$[Yb_{Ca}^{\bullet}] \approx 4[V_{Mn}^{\prime\prime\prime\prime}]+2[V_{Ca}^{\prime\prime}] \approx \text{constant} \qquad \textbf{Eq. 7-33}$$

Therefore, over some range of $p(O_2)$ cation vacancies will be independent of $p(O_2)$. According to the Schottky disorder reaction (Eq.7-2: $[V_{Ca}^{\prime\prime}][V_{Mn}^{\prime\prime\prime\prime}][V_O^{\bullet\bullet}]^3=K_S$) oxygen vacancies also must be independent of $p(O_2)$. Concentration of electron hole $[Mn_{Mn}^{\bullet}]$ can be calculated by substituting charge neutrality expression (Eq. 7-33) into the oxidation reaction (Eq. 7-8: $[V_{Mn}^{\prime\prime\prime\prime}][V_{Ca}^{\prime\prime}][Mn_{Mn}^{\bullet}]^6=K_p p(O_2)^{3/2}$) as follow:

$$[Mn_{Mn}^{\bullet}] = \left(\frac{K_p}{[V_{Ca}^{\prime\prime}][V_{Mn}^{\prime\prime\prime\prime}]}\right)^{1/6} p(O_2)^{1/4} \qquad \textbf{Eq. 7-34}$$

Inserting Eq. 7-34 in intrinsic electronic defect reaction (Eq.7-4: $[Mn_{Mn}^{\bullet}][Mn_{Mn}^{\prime}]=K_i$) yields to the concentration of electron $[Mn_{Mn}^{\prime}]$, expressed as:

$$[Mn_{Mn}^{\prime}] = \frac{K_i([V_{Ca}^{\prime\prime}][V_{Mn}^{\prime\prime\prime\prime}])^{1/6}}{K_P^{1/6}} p(O_2)^{-1/4} \qquad \textbf{Eq. 7-35}$$

Consequently, in the region of $10^{-5} < p(O_2) < 10^{-4}$ MPa oxygen vacancies and cation vacancies are independent of $p(O_2)$ while electrons and holes change with the slope of -1/4 and +1/4, respectively.

- **Impurity controlled region (electronic compensation): $p(O_2) \approx 10^{-15}< p(O_2) <10^{-5}$**

Over some range of $p(O_2)$ lower than 10^{-5} MPa, electrons $[Mn_{Mn}^{\prime}]$ will be fixed at the donor level and will be independent of $p(O_2)$, as a result the conductivity of donor-doped $CaMnO_3$ also shows an conductivity plateau. Therefore, this region corresponds to the compensation of donors by electrons:

$$[Mn'_{Mn}] \approx [Yb^{\bullet}_{Ca}] \qquad \textbf{Eq. 7-36}$$

The electron concentration cannot yet rise above the donor level because that would violate charge neutrality [8]. Since, in this plateau region the concentration of oxygen vacancies is much smaller than $[Yb^{\bullet}]$ and it seems oxidation and reduction do not have an effect on the macroscopic electronic conductivity**.**

According to the mass-action expression Eq. 7-36 and the intrinsic electronic defect reaction (Eq. 7-4: $[Mn^{\bullet}_{Mn}][Mn'_{Mn}] = K_I$) concentration of holes also are independent of $p(O_2)$. The average slope with the value of 3/4 is calculated for cation vacancies concentration by inserting constant value of hole concentration in oxidation reaction (Eq. 7-8: $[V''''_{Mn}][V''_{Ca}][Mn^{\bullet}_{Mn}]^6 = K_p p(O_2)^{3/2}$), and expressed as:

$$[V''_{Ca}] = \frac{K_p [Yb^{\bullet}_{Ca}]^2}{K_I^2} p(O_2)^{1/2}$$

$$[V''''_{Mn}] = \frac{K_p [Yb^{\bullet}_{Ca}]^4}{K_I^4} p(O_2)$$

$$[V''_{Ca}][V''''_{Mn}] = \frac{K_p [Yb^{\bullet}_{Ca}]^6}{K_I^6} p(O_2)^{3/2} \qquad \textbf{Eq. 7-37}$$

The average value of the slopes is 3/4 which is specified in the diagram.

Combining Eq.7-36 with mass-action expression of reduction reaction (Eq. 7-6: $[Mn'_{Mn}]^2[V^{\bullet\bullet}_O] = K_n p(O_2)^{-1/2}$) yields to the oxygen vacancy concentration with slope of -1/2, as follow:

$$[V^{\bullet\bullet}_O] = \frac{K_n}{[Yb^{\bullet}]^2} p(O_2)^{-1/2} \qquad \textbf{Eq. 7-38}$$

According to these calculations by decreasing $p(O_2)$ the concentration of oxygen vacancies increase, while the cation vacancies concentration decrease in order to satisfy charge neutrality.

- **Further reduction region: $p(O_2) < 10^{-15}$**

Further reduction pushes the process into a new region, where the effect of the donor dopant decreases and the behavior converges with that of pure $CaMnO_3$, with the same approximation to charge neutrality:

$$[Mn'_{Mn}] \approx 2[V^{\bullet\bullet}_O] \qquad \textbf{Eq. 7-39}$$

This behavior corresponds to the intrinsic behavior of the bulk of $CaMnO_3$.

In this region, increasing electron concentration enhances electrical conductivity slightly. However, as experimental data show (Figure 7-4a) conductivity decreases drastically in $p(O_2)$ below 10^{-16} MPa. According to the XRD-measurements, increasing the number of oxygen vacancies in highly reduction regime leads to the formation of the phase $CaMnO_{2.5}$ and with further reduction of the phase $CaMnO_2$. In these compounds localization of the charge carriers occur due to the oxygen ordering [159] which leads to the drastic decrease in conductivity.

Consequently, a comparison of figure 7-4a and 7-4c reveals that $p(O_2)$ dependence of concentration obtained from the defect chemical model is in good agreement with experimental results for 0.1% donor-doped $Yb_{0.001}Ca_{0.99}MnO_3$ compounds.

7.4.2 High doping level: 10 at. % Yb-dopant concentration

As discussed in section 7.3 (Figure 7-2), the experimental conductivity data demonstrate that by increasing the Yb concentration the negative slope in the high oxidizing region slightly tend to the plateau-like behavior. In the case of 10 at.% of Yb-addition this plateau-like region is extended from high oxidizing region down to around 10^{-16} MPa which indicates inactive Schottky reaction. Therefore, total charge neutrality condition for inactive Schottky reaction, as discussed before, can be formulated as:

$$[Mn'_{Mn}]=2[V_O^{\bullet\bullet}]+[Mn^{\bullet}_{Mn}]+[Yb^{\bullet}] \qquad \textbf{Eq. 7-40}$$

The experimental DC-conductivity measurement as a function of $p(O_2)$ as well as the corresponding defect diagram for 10 at % Yb-content is demonstrated in Figure 7-8.

Comparing experimental results with modified Kröger-Vink diagram reveals that in $p(O_2) > 10^{-16}$ MPa the extrinsic donors are electronically compensated corresponding to the charge neutrality condition:

$$[Mn'_{Mn}] = [Yb^{\bullet}] \qquad \textbf{Eq. 7-41}$$

In this plateau region, the concentration of oxygen vacancies is much smaller than $[Yb^{\bullet}]$ and it seems oxidation and reduction do not have an effect on the macroscopic electronic conductivity**.**

As Figure 7-8b shows, at highly reduction condition, the product of reduction reaction become the major defects and thus the dopant can be neglected. As a result, the

behavior is identical to that of the undoped material and charge neutrality can be described by bulk concentration of oxygen vacancies increases above the donor level.

The experimental measurements illustrates that by further reduction lower than 10^{-16} MPa drastic decrease in conductivity occurs. According to the XRD-characterizations, phase change takes place with decreasing $p(O_2)$ below 10^{-16} MPa as follows:

$$CaMnO_3\ (Orthorhombic) \xrightarrow{H_2\ in\ Ar} CaMnO_{2.5}(Orthorhombic) \xrightarrow{H_2\ in\ Ar} CaMnO_2(Cubic)$$

As a result, as mentioned before charge localization occurs which leads to the drastic reduction in mobility of charge carriers and hence conductivity decreases significantly.

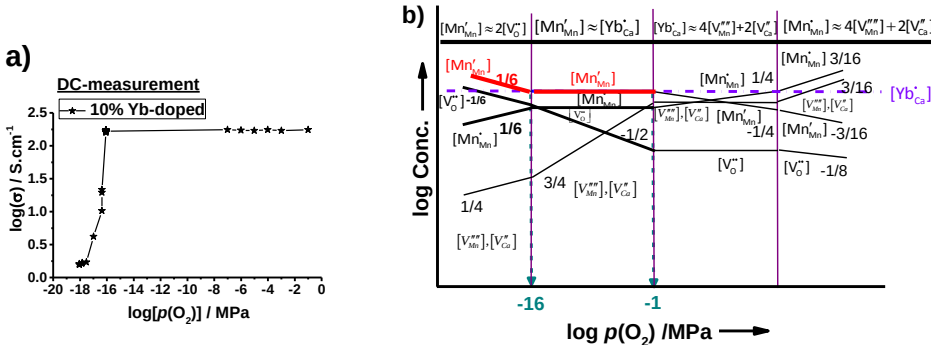

Figure 7-8: a) $p(O_2)$ dependence of conductivity observed by DC-measurement, and b) corresponding defect diagram calculated based on the equilibrium concentrations, which reveals inactive Schottky reaction for 10% of Yb-dopant ($Yb_{0.1}Ca_{0.9}MnO_3$) at 750°C.

In addition, the conductance of 40 nm thick thin film of 48 at. % Pr-doped $CaMnO_3$ (PCMO) grown on $SrTiO_3$ (STO) in different oxygen partial pressures $p(O_2)$ is shown in figure 7-9a which has been measured at 700°C by Herpers [162]. It is reported that, due to the defect formation during measurement in different $p(O_2)$ regions, the insulate substrates at room temperature and atmospheric pressure can become conducting at high temperatures. A reference data of a substrate is shown as open circles. At above 10^{-12} MPa conductance increases and demonstrates a positive slope. This is in agreement with proposed theoretical defect chemistry model in the present thesis.

According to the defect diagram (Figure 7-9b) the Schottky disorder will become active in high $p(O_2)$ more than 10^{-4} MPa which is due to the gradual increase in contribution of cation vacancies and electron holes in conductivity.

With reducing $p(O_2)$ concentration of intrinsic holes decrease while rising electron concentration cross the line for the hole and cation vacancy concentrations and intersect the horizontal line of donor doped. In this region, donor doped is compensated by cation vacancies, with charge neutrality approximated by $[Yb_{Ca}^{\bullet}] \approx 4[V_{Mn}^{\prime\prime\prime\prime}]+2[V_{Ca}^{\prime\prime}]$. In the mentioned region, according to the Schottky disorder reaction, oxygen vacancies must be independent of $p(O_2)$. Electrons and holes have the same dependence of $p(O_2)$, and expressed as:

$$[Mn_{Mn}^{\bullet}] = \left(\frac{K_p}{[V_{Ca}^{\prime\prime}][V_{Mn}^{\prime\prime\prime\prime}]}\right)^{1/6} p(O_2)^{1/4} \quad , \quad [Mn_{Mn}^{\prime}] = \frac{K_I([V_{Ca}^{\prime\prime}][V_{Mn}^{\prime\prime\prime\prime}])^{1/6}}{K_P^{1/6}} p(O_2)^{-1/4}$$

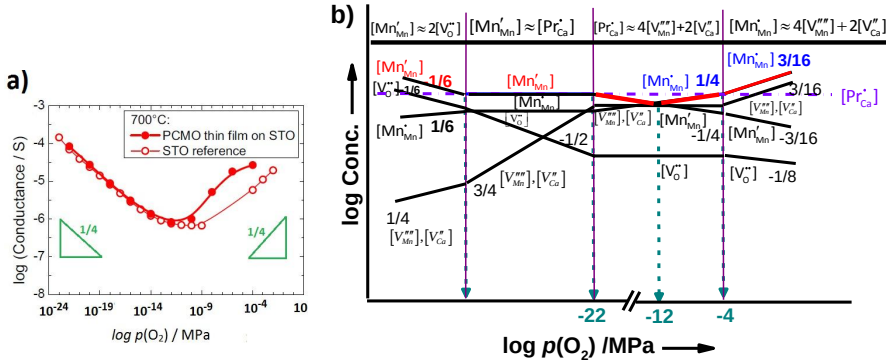

Figure 7-9: a) $p(O_2)$ dependence of conductivity observed by DC-measurement for $Pr_{0.48}Ca_{0.52}MnO_3$ [162], and b) corresponding proposed defect diagram calculated based on the equilibrium concentrations.

7.5 The defect chemistry modeling for acceptor-doped calcium manganite

In present thesis, the defect chemical model is suggested also for acceptor-doped $Ca_xRE_{1-x}MnO_3$, as shown in figure 7-10.

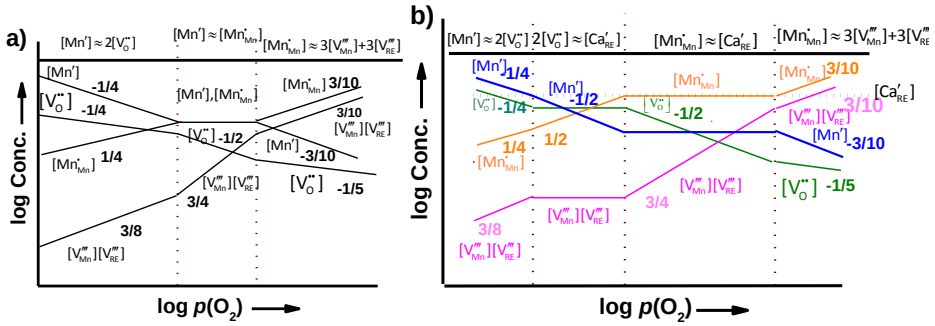

Figure 7-10: Proposed defect diagram for a) undoped and b) acceptor-doped $Ca_xRE_{1-x}MnO_3$.

The e_g bands are filed in $RE^{3+}Mn^{3+}O_3$ compounds. After adding acceptor-dopant, therefore there are charged states of $Mn^{4+}(Mn^{\bullet}_{Mn})$ and Mn^{3+} $(Mn^{\times}_{Mn})$. Accordingly, $Mn^{2+}(Mn'_{Mn})$ occur in equilibrium [156]. Since, the Mn^{2+} formation in manganites is often written as:

$$2Mn^{3+} = Mn^{2+} + Mn^{4+} \qquad \textbf{Eq. 7-42}$$

Schottky-type disorder and corresponding mass-action expression is formulated as:

$$nil \rightleftarrows V'''_{RE} + V'''_{Mn} + 3V^{\bullet\bullet}_{O} \qquad \textbf{Eq. 7-43}$$

$$[V'''_{Pr}][V'''_{Mn}][V^{\bullet\bullet}_{O}]^3 = K_S = K'_S \exp\left(-\frac{\Delta H_S}{\kappa T}\right) \qquad \textbf{Eq. 7-44}$$

In this case, the total charge neutrality can be expressed as:

$$[Ca'_{RE}] + [Mn'_{Mn}] + 3[V'''_{Mn}] + 3[V'''_{RE}] = 2[V^{\bullet\bullet}_{O}] + [Mn^{\bullet}_{Mn}] \qquad \textbf{Eq. 7-45}$$

$[Ca'_{RE}]$ refers to as the constant concentration of extrinsic defects, and indicates substitution of divalent Ca cation as an acceptor-dopant in rare earth element RE such as Yb^{3+} or Pr^{3+}. The concentration of intrinsic defects, i.e. Mn vacancies $[V'''_{Mn}]$, RE

vacancies $[V'''_{RE}]$, oxygen vacancies $[V^{\bullet\bullet}_{O}]$, electrons $[Mn'_{Mn}]$, and holes $[Mn^{\bullet}_{Mn}]$ are determined by the defect equilibrium of investigated compound.

In highly reduction regime where $[V^{\bullet\bullet}_{O}] >> [Ca'_{RE}]/2$, the constant acceptor concentration cannot compensate all number of oxygen vacancies, and thus electrons have to compensate the charge of the oxygen vacancies. Therefore, charge neutrality is simplified as: $[Mn'_{Mn}] \approx 2[V^{\bullet\bullet}_{O}]$. Increasing $p(O_2)$ shifts the electron concentration to the lower level of acceptor doped concentration. In this region the oxygen vacancy concentration is independent of $p(O_2)$. Since the negative charge of the acceptors must be compensated by a sufficient amount of positive charge, the further incorporation of oxygen is restricted [77]. Accordingly, the charge neutrality can be expressed as $2[V^{\bullet\bullet}_{O}] \approx [Ca'_{RE}]$. If Schottky equilibrium is activated, further oxidation changes the charge neutrality to $[Ca'_{RE}] \approx [Mn^{\bullet}_{Mn}]$ where holes compensate the negative charge of the acceptors. Because there is a considerable decrease in $[V^{\bullet\bullet}_{O}]$ with the slope of -1/2 in this region. And finally, in the highly oxidized region hole concentrations increase and cross the constant acceptor level. In this region the oxidation reaction becomes the major source of defects, and charge neutrality can be formulated as $[Mn^{\bullet}_{Mn}] \approx 3[V'''_{Mn}]+3[V'''_{RE}]$. All defect densities can be calculated according to mentioned charge neutrality and mass action expression of oxidation, reduction, intrinsic electronic, and Schottky disorder reactions, as explained for donor doped in previous sections.

7.6 Conclusions

In the present chapter, comprehensive DC-conductivity measurements accompanied by a defect chemistry modeling were performed in a wide range of oxygen partial pressure $p(O_2)$ (from 10^{-1} to 10^{-20} MPa) for compounds $Yb_xCa_{1-x}MnO_3$ (0 to 10 at. % of Yb addition) at 750°C for the first time. The defect chemistry models based on charge neutrality and mass action laws are suggested for both acceptor- and donor-doped $CaMnO_3$. The electric transport properties of rare earth doped $Yb_xCa_{1-x}MnO_3$ systems strongly depend to the chemistry of point defects. Kind and concentration of the electronic and ionic majority charge carriers are determined and formulated according to the proposed defect diagram.

It is observed that the DC-measurements are in excellent agreement with TGA experiments. A comparison of the mentioned experimental measurements and theoretical defect chemistry modeling reveals n-type conductivity for $Yb_xCa_{1-x}MnO_3$ (x = 0 to 0.005) accompanied by slightly active Schottky disorder at high oxidizing region. However for compounds with x > 0.005 Schottky disorder tends to be inactive and thus a plateau region (i.e. $p(O_2)$ independent conductivity) is observed even at highly oxidizing regime.

A plateau region also is observed for undoped $CaMnO_3$. The theoretical defect chemistry model demonstrates that the plateau region is attributed to the expression of charge neutrality dominated by the intrinsic electronic defects. It is suggested that the plateau region in conductivity for pure $CaMnO_3$ in the $p(O_2)$ range from 10^{-6} down to 10^{-11} MPa attributed to the formation of secondary phases $CaMn_2O_4$ and Ca_2MnO_4. The secondary phases adjacent to the grain boundaries probably form temporary barriers to migration of oxygen ions from grain to grain boundaries and thus to atmosphere in the mentioned $p(O_2)$ region. Consequently, oxygen vacancies do not have considerable effects on the electron and hole concentrations in the intermediate region. TGA experiments confirm this suggestion because they show a rather good weight stability (negligible released oxygen) in the same $p(O_2)$ region where the plateau state is observed in DC-measurements. In the case of Yb-doped compounds, the plateau region is extended to 10^{-5} MPa for 0.1 at. % up to 0.5 at % Yb-content, and to $p(O_2) > 10^{-3}$ MPa for 5 at. % and 10 at % Yb-addition. This is due to the fact that increasing dopant concentration enhances the amount of Mn^{3+} cations in Yb-doped compounds. The relatively larger ionic radius of Mn^{3+} (0.645 Å) cations compared to Mn^{4+} cations (0.53 Å) in $CaMnO_3$ lead to a low tolerance factor *t* deviated from unity. Accordingly, structure distortion takes place and perhaps secondary phases are formed even at higher $p(O_2)$ compared to pure $CaMnO_3$. Therefore the plateau state is extended with increasing Yb-dopant concentration.

The proposed defect chemistry model for pure $CaMnO_3$ contains three regions: the oxidation region, near-stoichiometric region and reduction region. While donor-doped $CaMnO_3$ demonstrates four regions. The extra region is clearly observed for 0.1 at % Yb-content in the range of $10^{-5} < p(O_2) < 10^{-4}$ which elucidates the ionic compensation of the

extrinsic donors by cation vacancies. In $p(O_2)$ lower than 10^{-5} MPa, as discussed above, the amount of oxygen released is negligible due to the formation of secondary phases. As a result, the electron concentration is governed by the amount of donor addition and charge neutrality is approximated by $[Mn'_{Mn}] \approx [Yb^{\bullet}_{Ca}]$ which is thus independent of $p(O_2)$. Therefore the conductivity of donor-doped $CaMnO_3$ shows a conductivity plateau in the specific region. It is also found that the slight increase in conductivity after plateau region down to 10^{-16} MPa is due to the slight oxygen released from the compounds in order to maintain an equilibrium state. Since each oxygen left two electrons, this leads to the increase in charge carrier concentration which causes gradual increase in conductivity.

The origin of significant reduction in conductivity in $p(O_2)$ less than 10^{-16} MPa is found to be due to the drastic oxygen loss at high reduction region. This leads to the formation of the phase $CaMnO_2$. Ordered oxygen vacancies in $CaMnO_2$ structure cause charge localization and thus conductivity decreases drastically.

A comparison of DC-conductivity measurements, TGA experiments, dilatometery analysis and XRD-measurements reveals a systematic phase change for $Yb_xCa_{1-x}MnO_3$ system which depends on the ratio of Mn^{3+}/Mn^{4+} as follows:

$$CaMnO_3 \text{ (Orthorhombic)} \xrightarrow[p(O_2) < 10^{-2} MPa]{O_2 \text{ in Ar}} Ca_2MnO_4 \text{ \& } CaMn_2O_4$$

$$\xrightarrow[p(O_2) < 10^{-16} MPa]{H_2 \text{ in Ar}} CaMnO_{2.5}\text{(Orthorhombic)} \xrightarrow[p(O_2) < 10^{-16} MPa]{H_2 \text{ in Ar (Further reduction)}} CaMnO_2\text{(Cubic)}$$

In fact, just before plateau region, compounds start to form secondary phases $CaMn_2O_4$ and Ca_2MnO_4. With decreasing $p(O_2)$ released oxygen causes relatively higher amount of Mn^{4+} cations reduce to Mn^{3+} cations. At around 10^{-16} MPa a phase $CaMnO_{2.5}$ is formed. In this structure all manganese ions are trivalent and oxygen deficient sites facilitate ion transport for oxygen via oxygen vacancies. Then at highly reduction region $CaMnO_{2.5}$ is reduced to $CaMnO_2$ with Mn^{2+} cations. Charge localization in $CaMnO_2$ leads to the drastic reduction in conductivity.

It is found that at $p(O_2) \approx 10^{-2}$ MPa with increasing donor dopant concentration from 0 at. % up to 10 at. % of Yb the conductivity increases gradually. Since substitution of Yb^{3+} cations for Ca^{2+} cations increases Mn^{3+} cations and thus enhances the charge

carriers which hop between Mn^{3+} and Mn^{4+} sites. However the nonlinearity is observed at lower $p(O_2)$. In fact, conductivity strongly depends on the density of Mn^{3+}-Mn^{4+} chains which form paths for electron migration. DC-measurements successfully reveal that both Yb-dopant concentration and the amount of partial pressure of oxygen $p(O_2)$ change the ratio of Mn^{3+}/Mn^{4+} and thus conductivity illustrate nonlinear behavior.

8 Summary

The main focus of the present thesis is to clarify the electric transport properties of rare earth doped $Yb_xCa_{1-x}MnO_3$ systems. These properties strongly depend on the chemistry of point defects. The least understood and incomplete information about the effect of chemistry of point defect on the electric transport properties of donor doped $CaMnO_3$ motivates the author to investigate on this subject comprehensively. One reason for this lack of information in the scientific literature relies certainly in the complexity of this material system since manganese cations possess several valence states in the quaternary oxide. The other reason possibly is due to the formation of cracks or deformation of $CaMnO_3$ in to the powder during electrical measurements in the reduction regions. This problem is successfully solved in the present thesis with systematic studies on preparation of ceramic samples as discussed in chapter 5.

To clarify the above mentioned objectives, initially the effect of different calcination and sintering conditions on physical properties of stoichiometric, non-stoichiometric (Ca-excess and Mn-excess) and 0.1 to 10 at. % of Yb-doped $CaMnO_3$ ceramics were intended in dependence of temperature T and partial pressure of oxygen $p(O_2)$.

Dilatometry measurements accompanied with SEM, EDX, XRD, Raman spectroscopy, iodometric titration and TGA experiments provide comprehensive and essential information that are extremely useful for choosing the right calcination and sintering conditions to produce desired crack free-ceramics suitable for electrical measurements. This is an important achievement regarding the further development of ceramics preparation.

Furthermore, based on the mentioned experiments phase transitions for different compounds $Yb_xCa_{1-x}MnO_3$ are defined in a wide range of $p(O_2)$ from 10^{-1} to 10^{-20} MPa as follows:

After sintering at 1350°C, in gas composition of 100% O_2: $CaMnO_3$ (Orthorhombic)

$$\xrightarrow[p(O_2) < 10^{-2}\ \text{MPa}]{O_2\ \text{in Ar}} Ca_2MnO_4\ \&\ CaMn_2O_4 \xrightarrow[p(O_2) < 10^{-16}\ \text{MPa}]{H_2\ \text{in Ar}} CaMnO_{2.5}\,(\text{Orthorhombic})$$

$$\xrightarrow[p(O_2) < 10^{-16}\ \text{MPa}]{H_2\ \text{in Ar (Further reduction)}} CaMnO_2\,(\text{Cubic})[\text{after TGA experiments at } p(O_2) \approx 10^{-19}\,\text{MPa}]$$

It is found that the phase transitions are due to change in the ratio of Mn^{3+}/Mn^{4+}. DC-conductivity measurements and impedance experiments successfully reveal that the Yb-dopant concentration, the partial pressure of oxygen $p(O_2)$ and temperature strongly change the ratio of Mn^{3+}/Mn^{4+} which affect the electrical conductivity.

The electronic and ionic contributions of conductivity originate from the bulk are investigated in chapter 6 by impedance measurements accompanied by modeling the compounds in terms of an electrical equivalent circuit in a wide range of temperatures (-100 to 300°C) and frequencies (1Hz to 1 MHz). The measurements also reveal the main role of grain boundaries in $Yb_xCa_{1-x}MnO_3$ systems. A novel schematic illustration based on the double-Schottky-barrier model for polycrystalline ceramics is proposed which clearly describes the contribution of different resistance components in electric transport properties. An additional resistive component is obsreved in electrical equivalent circuit models at temperatures above 100°C which probably is related to ionic contribution due to oxygen vacancies. Since measuring the ambient gas composition with regard to the oxygen content using a ZrO_2 oxygen sensor during dilatometery measurements from room to elevated temperatures up to around 1400°C reveals that compounds start to release O_2-gas from 100°C upwards. It is also found that polarization forms internal barrier capacitors at the grain boundaries which can be explained by Maxwell-Wagner polarization. This leads to a surprisingly large dielectric permittivity value ε' around 10^5 at frequency of 10^3 Hz. It is demonstrated that the first dielectric relaxation below 25°C probably depends on the amount of Mn^{3+}cations and thus on the contribution of polarons to conductivity. The second relaxation peak is observed at above 100°C which is probably due to the thermally activated creation of oxygen vacancies.

Kind and concentration of the electronic and ionic majority charge carriers are determined and formulated according to the proposed defect chemistry modeling for both acceptor and donor-doped $CaMnO_3$ in chapter 7. It is demonstrated that in the highly oxidizing regime around $p(O_2) > 10^{-6}$ MPa the oxidation reaction is major source of defects and thus holes are compensated by cation vacancies. According to the oxidation reaction and Schottky equilibrium reaction in this region the number of holes increases while the concentration of oxygen vacancies decreases.

A $p(O_2)$ independent conductivity (plateau region) is observed in the intermediate $p(O_2)$ region from 10^{-11} to 10^{-6} MPa for pure $CaMnO_3$. According to the proposed theoretical defect chemistry modeling (Kröger-Vink diagram) in this region expression of charge neutrality is dominated by the intrinsic electronic defects. At 0.1 at. % of Yb addition in $p(O_2)$ range from 10^{-14} MPa up to 10^{-5} the electron concentration is governed by the amount of donor addition. Therefore charge neutrality is approximated by $[Mn'_{Mn}] \approx [Yb^{\bullet}_{Ca}]$ which is thus independent of $p(O_2)$ and shows a conductivity plateau.

The origin of the plateau state in conductivity is investigated by a comparison of TGA-experiments and DC-conductivity measurements, since both demonstrate a plateau state in approximately identical $p(O_2)$ region. In fact, positions of oxygen anions in the lattice might be shifted by reducing $p(O_2)$ which means that oxygen vacancy concentration increases. It is suggested that deviated oxygen ions form the secondary phases $CaMn_2O_4$ and Ca_2MnO_4. The secondary phases which are accumulated near grain boundaries temporarily form barriers to oxygen migration. Therefore the amount of oxygen released from grain to grain boundaries and thus to the atmosphere is reduced in the intermediate region. Consequently oxygen vacancies do not have considerable effects on the electron and hole concentrations. SEM, EDX, XRD- measurements and Raman spectroscopy experiments demonstrate that the mentioned secondary phases are formed after sintering at $p(O_2)$ lower than 10^{-2} MPa, which confirm the suggestion above.

Further reduction increases the amount of oxygen released which causes relatively higher amount of Mn^{4+} cations reduce to Mn^{3+} cations. Therefore in this reduction region electrons are charge compensating species. Therefore conductivity slightly enhances after the plateau state. However drastic reduction is observed by reducing $p(O_2)$ below 10^{-16} MPa. According to some previous reports [163] conductivity of $CaMnO_{3-\delta}$ increases with increasing oxygen vacancies up to $\delta \approx 0.25$ at any fixed temperature. However at $\delta > 0.25$ conductivity decreases. Therefore it is suggested that at around 10^{-16} MPa a new phase $CaMnO_{2.5}$ is formed with trivalent manganese valency state. In this structure oxygen deficient sites facilitate ion transport for oxygen via oxygen vacancies. Then at highly reduction region $CaMnO_{2.5}$ is reduced to $CaMnO_2$ with Mn^{2+} cations. Charge localization in cubic $CaMnO_2$ leads to the drastic reduction in

conductivity. This suggestion is confirmed by XRD-measurements after TGA experiments at high reduction region. In addition, the defect chemistry models for pure $CaMnO_3$ contain three regions, while those for donor doped $CaMnO_3$ demonstrate four regions. Consequently, a comparison of DC-conductivity measurements and proposed theoretical defect chemistry modeling (Kröger-Vink diagram) reveal the main role of the ionic (oxygen vacancies and cation vacancies) and electronic (electrons and holes) contributions in conductivity. Accordingly, n-type conductivity is determined for $Yb_xCa_{1-x}MnO_3$ (x = 0 to 0.005) accompanied by slightly active Schottky disorder at high oxidizing region. However for compounds with x > 0.005 Schottky disorder is inactive and thus a plateau region is observed even at highly oxidizing regime. This is probably due to the increase in the electron concentration and structure distortion with raising dopant concentration which causes perhaps secondary phases form even at higher $p(O_2)$ compared to pure $CaMnO_3$. Finally, the proposed model reveals the origin of charge carriers participating in electronic transport.

In summary, the present thesis reveals the answer of the main questions about the details of the chemistry of point defects, ionic as well as electronic charge transport contributing in conductivity for donor-doped $Yb_xCa_{1-x}MnO_3$ systems. A comparison of the experimental observations and the theoretical defect chemical models clearly show the way for controlling charge carriers in dependence of partial pressure of oxygen $p(O_2)$ and dopant concentrations. The origin of plateau state in conductivity is figure out to be probably due to formation of secondary phases where oxygen ions do not substantially influence the electron and hole concentrations. Bulk conductivity measurements reveal the main role of grain boundaries and electronic and ionic contributions in conductivity. According to the present experiments the formation of oxygen vacancies and corresponding change in density of Mn^{3+}-Mn^{4+} pair sites seem to play an important role in phase transition, charge migration and resistance properties of the complex systems $Yb_xCa_{1-x}MnO_3$. It is well known that resistive switching mechanism and thermoelectric power *S* depend on the concentration and nature of the charge carriers. Therefore the obtained information probably will be useful for better understanding the effect of resistive switching as well as thermoelectric properties for the investigated compounds and probably for other similar complex oxide systems.

9 References

[1] A. J. Moulson and J. M. Herbert: "Electroceramics, materials, properties and applications", *Chapman and Hall, New York, USA*. (1990) 464 pages.

[2] N. Bonanos, K. S. Knight and B. Ellis: "Perovskite solid electrolytes: Structure, transport properties and fuel cell applicatiaons", *Solid State Ionics.* **79** (1995) 161-170.

[3] P. Granger, V. I. Parvulescu, S. Kaliaguine and W. Prellier: "Perovskites and related mixed oxides: concepts and applications, Band 1", *John Wiley & Sons.* (2016) 1056 pages.

[4] S. Keav, S. K. Matam, D. Ferri and A. Weidenkaff: "Structured perovskite-based catalysts and their application as three-way catalytic converters—a review", *J. Catalysts.* **4** (2014) 226-255.

[5] Y. Xiao, D. Wang, G. Cai, Y. Zheng and F. Zhong: "A $GdAlO_3$ perovskite oxide electrolyte-based NO_x solid-state sensor", *J. Scientific Reports.* **6** (2016) 1-9.

[6] R. Waser, T. Baiatu and K. H. Härdtl: "Dc electrical degradation of perovskite-type titanates: I, ceramics", *J. Am. Ceram. Soc.* **73** (1990) 1645–1673.

[7] H. H. Nahm and C. H. Park: "Microscopic study of defects in perovskite oxide", *J. the Korean Physical Society*. **47** (2005) S329-S332.

[8] D. M. Smyth: "The defect chemistry of metal oxides", *Oxford University Press, New York, USA*. (2000) 294 pages.

[9] J. Daniels and K. H. Härdtl: "Electric conductivity at high temperature of donor-doped barium titanate ceramics, part1", *J. Philips Res. Rep*. **31** (1976) 489.

[10] J. Daniels: "Defect equilibria in acceptor-doped barium titanate", *J. Philips Res. Rep*. **31** (1976) 505.

[11] D. Hennings: "Thermogravimetric investigations", *J. Philips Res. Rep*. **31** (1976) 516.

[12] R. Wernicke: "The kinetics of equilibrium restoration in barium titanate ceramics", *J. Philips Res. Rep.* **31** (1976) 526.

[13] J. Daniels and R.Wernicke: "New aspects of an improved PTC model", *J. Philips Res. Rep.* **31** (1976) 544.

[14] N. H. Chan and D.M.Smyth: "Nonstoichiometry in $SrTiO_3$", *J. Electrochem. Soc.* **128** (1981) 1762.

[15] N. H. Chan, R. K. Sharma and D. M. Smyth: "Nonstoichiometry in acceptor-doped $BaTiO_3$", *J. Am. Ceram. Soc.* **65** (1982) 167.

[16] N. H. Chan and D. M.Smyth: "Defect Chemistry of Donor-Doped $BaTiO_3$ ", *J. Am. Ceram. Soc*. **67** (1984) 285-288.

[17] R. Waser, T. Baiatu and K. H. Härdtl: "DC electrical degradation of perovskite-type titanates: II, single crystals", *J. Am.Ceram. Soc*. **73** (1990) 1654.

[18] F. A. Kröger, H.J. Vink: "Relations between the concentrations of imperfections in crystalline solids", *J. Solid State Physics*. **3** (1956) 307–435.

[19] J. M. D. Coey, M. Viret and S. v. Molnár: "Mixed valence manganites", *J. Adv. Phys*. **58** (2009) 571.

[20] S. B. Adler: "Factors governing oxygen reduction in solid oxide fuel cell cathodes", *J.* Chem. *Rev.* **104** (2004) 4791.

[21] S. Jin, T. H. Tiefel, M. McCormack, R. A. Fastnacht, R. Ramesh and L.H. Chen: "Thousandfold changes in resistivity in magnetoresistive La-Ca-Mn-O films", *J. Science.* **15** (1994). 413.

[22] S. Kumar, V.S. Raju, S. Bera, K. Vijaynandhini and T.R.N. Kutty: "Studies on surface composition and chemical states of calcium manganites", *J. Nuclear Instruments and Methods in Physics Research B*. **237** (2005) 623–630.

[23] L. Malavasi: "The role of defect chemistry in the properties of perovskite manganites", *J. Mater. Chem.* **18** (2008) 3295.

[24] H. S. Lee, S. G. Choi, H. j. Choi, S. W. Chung and H. H. Park: "Study of resistive switching property in $Pr_{0.7}Ca_{0.3}MnO_3$, $CaMnO_3$ and their bi-layer films", *J. Thin Solid Films.* **529** (2013) 347–351.

[25] P. Thiel, S. Populoh, S. Yoon, G. Saucke and K. Rubenis: "Charge-Carrier Hopping in Highly Conductive $CaMn_{1-x}M_xO_{3-\delta}$ Thermoelectrics", *J. Phys. Chem. C.* **119** (2015) 21860−21867.

[26] P. Hallberg, M. Källén, D. Jing, F. Snijkers, J. v. Noyen, M. Rydén and A. Lyngfelt: "Experimental investigation of $CaMnO_{3-\delta}$ based oxygen carriers used in continuous chemical-looping combustion", *J. Chemical Engineering*. (2014) 1-9.

[27] D. Jing, T. Mattisson, H. Leion , M. Rydén and A. Lyngfelt : "Examination of perovskite structure $CaMnO_{3-\delta}$ with MgO addition as oxygen carrier for chemical looping with oxygen uncoupling using methane and syngas", *J. Chemical Engineering*. (2013) 1-16.

[28] L. Bocher, M. H. Aguirre, R. Robert, D. Logvinovich, S. Bakardjieva, J. Hejtmanek and A. Weidenkaff: "High-temperature stability, structure and thermoelectric of properties $CaMn_{1-x}Nb_xO_3$ phases", *J. Acta Materialia.* **57** (2009) 5667–5680.

[29] V. Markovich, I. Fita, A. Wisniewski, R. Puzniak, D. Mogilyansky and L. Titelman: "Surface and exchange-bias effects in compacted $CaMnO_{3-\delta}$ nanoparticles", *J. Physical review B.* **77** (2008) 054410.

[30] M. Molinari, D. Tompsett, S. Parker, F. Azoughb and R. Freer:" Structural, electronic and thermoelectric behaviour of $CaMnO_3$ and $CaMnO_{3-\delta}$", *J. Mater. Chem*. A. **2** (2014) 14109–14117.

[31] M. Ohtaki, H. Koga, T. Tokunaga, K. Eguchi and H. Arai: "Electrical transport properties and high-temperature thermoelectric performance of $(Ca_{0.9}M_{0.1})MnO_3$ (M = Y, La, Ce, Sm, In, Sn, Sb, Pb, Bi)", *J. Solid State Chemistry.* **120** (1995) 105-111.

[32] R. Mahendiran A. Maignan, C. Martin, M. Hervieu and B. Raveau: " $Ca_{0.85}Sm_{0.15}MnO_3$: A mixed antiferromagnet with unusual properties", *J. Physical review B.* **62** (2000) 11 644-11 648.

[33] T. Maitra and A. Taraphder: "Magnetic, orbital, and charge ordering in the electron-doped manganites", *J. Physical review B.* **68** (2003) 174416 .

[34] J. Du, T. Zhang, F. Cheng, W. Chu, Z. Wu and J. Chen: "Nonstoichiometric perovskite $CaMnO_{3-\delta}$ for oxygen electrocatalysis with high activity", *J. Inorg. Chem.* **53** (2014) 9106−9114.

[35] R. Mathieu and Y.Tokura: "The nanoscale phase separation in hole-doped manganites", *J. Physical Society of Japan*. **76** (2007) 124706.

[36] S. Suga und A. Sekiyama: "Photoelectron spectroscopy: bulk and surface electronic structures", *Springer-Verlag Berlin Heidelberg.* (2014) 378 pages.

[37] H. T. Lin, Y. Katoh, J. Matyáš, A. Gyekenyesi and M. Halbig: "Ceramic materials for energy applications IV: ceramic engineering and science proceedings", *John Wiley & Sons, New Jersey*. **35** (2015) 44-48/176 pages.

[38] J. Zhu, H. Li, L. Zhong, P. Xiao, X. Xu and X. Yang: "Perovskite oxides: preparation, characterizations and applications in heterogeneous", *J. ACS Catal.* **4** (2014) 2917−2940.

[39] M. Johnsson and P. Lemmens: "Crystallography and chemistry of perovskites", *Handbook of Magnetism and Advanced Magnetic Materials*, *John Wiley & Sons, Ltd*. (2007) 1-11.

[40] N. Hamdad and B.Bouhafs: "Theoretical analysis of the spin effect on the electronic and magnetic properties of the calcium manganese oxide $CaMnO_3$: GGA+U calculation", *J. Physica B.* **405** (2010) 4595–4606.

[41] B. Sarbas, W. Töpper: "Mn manganese: natural occurrence. minerals (native metal, solid solution, silicide, and carbide. Sulfides and related compounds. Halogenides and oxyhalogenides. Oxides of type MO)", *Springer-Verlag, Berlin Heidelberg.* (2013) 181 pages.

[42] ICSDWeb: "$CaMnO_3$ Crystal Structure", ICSD Coll.Code: 35218, *Forschungszentrum Juelich GmbH* (2017).

[43] ICSDWeb: "$CaMn_2O_4$ Crystal Structure", ICSD Coll.Code: 34117, *Forschungszentrum Juelich GmbH* (2017).

[44] ICSDWeb: "Ca_2MnO_4 Crystal Structure", ICSD Coll.Code: 50789, Forschungszentrum Juelich GmbH (2017).

[45] D. Cristophe: "Multiferroic perovskites under epitaxial strain: the case of $TbMnO_3$ thin films", *Diss.*, *Groningen* (2009) 141 pages.

[46] J. M. D. Coey and M. Viret: "Mixed-valence manganites", *J. Advances in Physics,* **48** (1999) 167/293.

[47] G. Iadonisi, J. Ranninger and G. De Filippis: "Polarons in bulk materials and systems with reduced dimensionality", *Band 161 von International School of Physics: Enrico Fermi, IOS Pres.* (2006) 468 pages.

[48] P. Beaud, A. Caviezel, S. O. Mariager, L. Rettig, G. Ingold, C. Dornes and S. W. Huang: "A time-dependent order parameter for ultrafast photoinduced phase transitions", *J. Nature materials.* **13** (2014) 923–927.

[49] Y. Tokura, and N. Nagaosa: "Orbital physics in transition-metal oxides", *J. Science*. **288** (2000) 462-468.

[50] E. Pavarini, E. Koch, F. Anders, and M. Jarrell: "Correlated Electrons: from Models to materials", *Forschungszentrum Jülich.* **2** (2012) chapter 7/463 pages.

[51] J. R. Hook and H. E. Hall: "Solid state physics", *John Wiley & Sons*. (2013) chapter 8/ 392 pages.

[52] G. Jonker & J. Van Santen: "Ferromagnetic compounds of manganese with perovskite structure", *J. Physica*. **16** (1950) 337.

[53] C. Zener: "Interaction between the d-Shells in the Transition Metals II. Ferromagnetic Compounds of Manganese with Perovskite Structure", *J. Phys. Rev.* **81** (1951) 403-405.

[54] P.W. Anderson and H. Hasegawa: "Considerations on double exchange", *J.Phys. Rev.* **100** (1955) 675.

[55] P.G. de Gennes: "Effects of double exchange in magnetic crystals", *J. Phys. Rev.* **118** (1960) 141.

[56] H. A. KRAMERS: " L'interaction Entre les Atomes Magnétogènes dans un Cristal Paramagnétique ", *Physica.* 1 (1934) 1 182-192.

[57] Y. Tokura: "Critical features of colossal magnetoresistive manganites", *J. Rep. Prog. Phys.* **69** (2006) 797–851.

[58] H.O. Wang Z. Chu, K.P. Su, W.S. Tan and D.X. Huo: "Colossal magnetoresistance of $Pr_{0.7}Sr_{0.3}MnO_3$ layer grown on charge-ordered $La_{0.5}Ca_{0.5}MnO_3$ manganite layer", *J. Alloys and Compounds*. **689** (2016) 69-74.

[59] T. Chatterji, P. F. Henry and B. Ouladdiaf: "Neutron diffraction investigation of the magneto-elastic effect in $LaMnO_3$", *J. Physical review B*. **77** (2008) 2124031-4.

[60] D. Khomskii: "Transition metal compounds" *J. Cambridge University Press.* 500 Seiten, (2014) 151.

[61] T. Chatterji, G. J. McIntyre, A. Stunault, B. Ouladdiaf, and F. Fauth: "Neutrons and magnetism, a review of ILL research on magnetic", *J. Neutrons for science.* (2004) 1-24.

[62] S. Dong S. Dai, X. Y. Yao, K. F. Wang, C. Zhu and J.-M. Liu: "Jahn-Teller distortion induced charge ordering in the CE phase of manganites", *J. Physical review B.* **73** (2006) 104404.

[63] C. N. R. Rao, B. Raveau: "Colossal Magnetoresistance, charge ordering and related properties of manganese oxides", *J. World Scientific.* (1998) 356 Seiten/242.

[64] D. Sousa, M.R. Nunes, C. Silveira, I. Matos, A. B. Lopes and M. E. Melo Jorge: "Ca-site substitution induced a metal–insulator transition in manganite $CaMnO_3$", *J. Materials Chemistry and Physics.* **109** (2008) 311–319.

[65] T. Lichtenthaler: "Ordering of oxygen vacancies in reduced phases of $CaMnO_{3-x}$ and $SrMnO_{3-x}$", *Blindern, Oslo, November : University of Oslo* (2005) 118 pages.

[66] S. Jin, M. McCormack, T. H. Tiefel and R. Ramesh: "Colossal magnetoresistance in La-Ca-Mn-O ferromagnetic thin films", *J. Applied Physics.* **76** (1994) 6929-33.

[67] E. I. Goldyreva, I. A. Leonidov, M. V. Patrakeev and V. L. Kozhevnikov: "Oxygen non-stoichiometry and defect equilibrium in $CaMnO_{3-\delta}$", *J. Solid State Electrochem.* **16** (2012) 1187–1191.

[68] C. B. Carter and M. G. Norton: "Ceramic materials, science and engineering", *Springer-Verlag New York* (2013) 766 pages.

[69] Interstitial defects vacancies, https://www.fisk.edu/

[70] J. Frenkel: "Über die Wärmebewegung in festen und flüssigen Körpern", *J. Z. Physik*. 35 (1926) 652.

[71] P. Kofstad and T. Norby: "Defects and transport in crystalline solids", *Department of Chemistry Faculty of Mathematics and Natural Sciences University of Oslo*, (2004) 209 pages.

[72] R. Waser :" Bulk conductivity and defect chemistry of acceptor-doped strontium titanate in the quenched state", *J. Am. Ceram. Soc*. **74** (1991) 1934-40.

[73] R. Moos and K.H. Hardtl: "Defect chemistry of donor-doped and undoped strontium titanate ceramics between 1000° and 1400°C", *J. American Ceramic Society.* **80** (1997) 2549–62.

[74] R. Waser, R. Dittmann, G. Staikov and K. Szot: "Redox-Based resistive switching memories nanoionic mechanisms, prospects, and challenges", *J. Adv. Mater.* **21** (2009) 2632–2663.

[75] R. A. De Souza:"Oxygen diffusionin $SrTiO_3$ and related perovskite oxides", *J. adv. funct. Mater. WILEY-VCH Verlag GmbH & Co.KGaA, Weinheim.* (2015) 1-17.

[76] C. Ohly, S. Hoffmann-Eifert, X. Guo, J. Schubert and R. Waser: "Electrical conductivity of epitaxial $SrTiO_3$ thin films as a function of oxygen partial pressure and temperature", *J. Am. Ceram. Soc.* **89** (2006) 2845.

[77] F. Gunkel: " The role of defects at functional interfaces between polar and non-polar perovskite oxides", *Diss., RWTH Aachen University, Forschungszentrum Juelic*. **29** (2013).

[78] S. N. Ruddlesden and P. Popper:"The compound $Sr_3Ti_2O_7$ and its structure", *Acta Cryst.* **11** (1958) 54-55.

[79] N.W. Ashcroft and N. D. Mermin: "Solid state physics", *Saunders College*, USA. (1976) 12/826 pages.

[80] W. H. Lee, W. A. Groen, H. Schreinemacher and D. Hennings: „Dysprosium doped dielectric materials for sintering in reducing atmospheres ", *J. Electroceram.* **5** (2000) 31.

[81] X. Guo, C. Pithan, C. Ohly, C. L. Jia, J. Dornseiffer, F. H. Haegel and R. Waser: "Enhancement of p-type conductivity in nanocrystalline $BaTiO_3$ ceramics", *J. Appl. Phys. Lett.* **86** (2005) 082110 1-4.

[82] C. Pithan, w. Y. Shiratori and R. Waser: "Preparation, processing, and characterization of nano-crystalline$BaTiO_3$ powders and ceramics derived from microemulsion-mediated synthesis", *J. Am. Ceram. Soc.*, **89** (2006) 2908–2916.

[83] H. Katsu:"Crystal- and defect-chemistry of fine grained thermistor ceramics on $BaTiO_3$ basis with BaO excess", Diss., RWTH Aachen University, Forschungszentrum Jülich GmbH. **18** (2011).

[84] C. Pithan, Y. Otsukaa, C. Pithan, J. Dornseiffer, T. Takada, T. Konoike and Rainer Waser: "Synthesis of nitrogen and lanthanum codoped barium titanate with anovel thermal ammonolysis reactor", *J. European Ceramic Society*. **36** (2016) 2719–2725.

[85] N. David: "Grain Boundaries", *National Board*. (1991) 1-3. https:// www.nationalboard.org/ Print Page. aspx?pageID=164&ID=194.

[86] http://www.bnm.mtl.kyoto-u.ac.jp/outline/background_e.html (2010).

[87] R. F. Klie, M. Beleggia, Y. Zhu, J. P. Buban and N. D. Browning: "Atomic-scale model of the grain boundary potential in perovskite oxides", *J. Physical review B*. **68** (2003) 214101-10.

[88] F. Greuter and G. Blatter: "Eelectrical properties of grain boundaries in polycrystalline compound semconductors", *J. Semicond. Sci. Technol.* **5** (1990) 111-137.

[89] Y. M. Chiang and T. Takagi: "Grain-boundary chemistry of barium titanate and strontium titanate: I, high-temperature equilibrium space charge", *J. Am Cefum Soc.* 73 (1990) 3278-85.

[90] R. A. De Souza, J. Fleig, J. Maier, O. Kienzle, Z. Zhang, W. Sigle and M. Rühle: "Electrical and structural characterization of a low-angle tilt grain boundary in iron-doped strontium titanate", *J. Am. Ceram. Soc.* **86** (2003) 922–28.

[91] R. A. De Souza:"The formation of equilibrium space-charge zones at grain boundaries in the perovskite oxide $SrTiO_3$", *J.Phys. Chem. Chem. Phys.* **11** (2009) 9939–9969.

[92] Y. Sato, T. Tanaka, F. Oba, T. Yamamoto, Y. Ikuhara and T. Sakuma: "Non-linear current–voltage characteristics related to native defects in SrTiO3 and ZnO bicrystals", *J, Science and Technology of Advanced Materials.* **4** (2003) 605–611.

[93] Y. M. Chiang, D. P. Birnie and W. D. Kingery: "Physical Ceramics: principles for ceramic science and engineering", *John Wiley & Sons, Inc.* (1997) 544 pages.

[94] A. Asamitsu, Y. Tomioka, H. Kuwahara and Y. Tokura: "Current switching of resistive states in magnetoresistive manganites", *J. Nature.* **388** (1997) 50–52 .

[95] R. Fors, S. I. Khartsev and A. M Grishin: "Giant resistance switching in metal-insulator-manganite junctions: evidence for Mott transition", *J. Physical review B.* **71** (2005) 045305.

[96] A. Sawa, T. Fujii, M. Kawasaki and Y. Tokura: "Interface resistance switching at a few nanometer thickperovskite manganite active layers", *J. Appl. Phys. Lett.* **88** (2006) 232112.

[97] R. Shawna, B. Eric, S. Toberer, T. Ikeda, A. C. Cox, F. Gascoin, M. S. Kauzlarich and G. J. Snyder: "Improved thermoelectric performance in $Yb_{14}Mn_{1-x}Zn_xSb_{11}$ by the reduction of spin-disorder scattering", *J. Chem. Mater.* **20** (2008) 3412–3419.

[98] N. Orlovskaya, A. Terracciano and A. Dasgupta: "Hermoelectric power generator and combustion apparatus", *Vols. WO Patent App.* PCT/US2015/019,916 (2015).

[99] M. Schier, N. Kevlishvili, B. Mayer: "Thermal management concepts for vehicles of next generation", *Ninth International Conference on Ecological ehicles and Renewable Energies* (2014).

[100]V. V. Kharton:"Solid State Electrochemistry II: Electrodes, Interfaces and Ceramic Membranes", *John Wiley & Sons*. (2011) 568 pages.

[101]R. Waser and M. Aono: "Nanoionics-based resistive switching memories", *J. nature materials.* **6** (2007) 833-840.

[102]T. W. Hickmott :"Low-frequency negative resistance in thin anodic oxide films", *J. Appl. Phys.* **33** (1962) 2669–2682.

[103]G. Dearnaley, A. M. Stoneham and D. V. Morgan :"Electrical phenomena in amorphous oxide films", *J. Rep. Prog. Phys.* **33** (1970) 1129–1191.

[104]D. P. Oxley: "Electroforming, switching and memory effects in oxide thin films", *J. Electrocomponent Sci. Technol. UK* **3** (1977) 217–224.

[105]H. Pagnia and N. Sotnik: "Bistable switching in electroformed metal-insulator-metal devices", *J. Phys. Status Solidi.* **108** (1988) 11–65.

[106]M. N. Kozicki, M. Yun, L. Hilt and, A. Singh: "Applications of programmable resistance changes in metal-doped chalcogenides", *Pennington NJ USA: Electrochem. Soc.* (1999) 298–309.

[107] A. Beck, J. G. Bednorz, C. Gerber, C. Rossel and D. Widmer: "Reproducible switching effect in thin oxide films for memory applications", *J. Appl. Phys. Lett.* **77** (2000) 139–141.

[108]A. Sawa: "Resistive switching in transition metal oxides", *J. Mater.* **11** (2008) 28–36.

[109]S. Park, S. Jung, M. Siddik, M. Jo, J. Lee, J. Park, W. Lee, S. Kim, S. M. Sadaf, X. Liu and H. Hwang: "Memristive switching behaviour in $Pr_{0.7}Ca_{0.3}MnO_3$ by incorporating an oxygen-deficient layer", *J. Phys. Stat. Sol. RRL.* 5 (2011) 409.

[110]C. Rodenbücher, W. Speier, G. Bihlmayer, U. Breuer, R. Waser and K. Szot: "Cluster-like resistive switching of $SrTiO_3$:Nb surface layers", *New J. Phys.* **15** (2013) 103017 1-15..

[111]B.P. Anderasson, M. Janousch, U. Staub and G.I. Meijer: "Spatial distribution of oxygen vacancies in Cr-doped $SrTiO_3$ during an electric-field-driven insulator-to-metal transition", *J. Appl. Phys. Lett.* **94** (2009) 013513.

[112]B.P. Anderasson, M. Janousch, U. Staub, G.I. Meijer, A. Ramar, J. Krbanjevic and R. Schaeublin: "Origin of oxygen vacancies in resistive switching devices", *J. Phys.* **190** (2009) 012074 1-17.

[113]H. Schock, G. Brereton, E. Case, J. D'Angelo, T. Hogan, M. Lyle, R. Maloney, K. Moran, J. Novak, C. Nelson, A. Panayi, T. Ruckle, J. Sakamoto, T. Shih, E. Timm, L. Zhang, G. Zhu: "Prospects for implementation of thermoelectric generators as waste heat recovery systems in class 8 truck applications", *J. Energy Resources Technology.* **135** (2013) 022001-1.

[114]F. Suarez, A. Nozariasbmarz, D. Vashaee and M. C. öztürk: "Designing thermoelectric generators for self-powered wearable electronics", *J. Energy Environ. Sci.* ***9*** (2016) 2099-2113.

[115]J. C. ZHENG:"Recent advances on thermoelectric materials", *J. Front. Phys. China,* **3** (2008) 269-279.

[116]G. Xu, R. Funahashi, I. Matsubara, M. Shikano, and Y. Zhou: "High-temperature thermoelectric properties of the $Ca_{1-x}Bi_xMnO_3$ system", *J. Mater. Res.* **17**(2002) 1092-1095.

[117]https://www.youtube.com/watch?v=21EC0lZ0imw

[118]K. Koumoto, Y. Wang, R. Zhang, A. Kosuga and R. Funahashi: "Oxide thermoelectric materials: a nanostructuring approach", *Annu. Rev. Mater. Res.* **40** (2010) 363.

[119]T. Takabatake, K. Suekuni, T. Nakayama and E. Kaneshita: "Phonon-glass electron-crystal thermoelectric clathrates: Experiments and theory", Rev. Mod. Phys. 86, (2014) 699.

[120]R. Waser: "Nanoelectronics and information technology-Advanced Electronic Materiels and Novel Devices", *Wiley-VCH verlag GmbH&KGaA, Weinheim (2003)*. 3rd Edition **7** (2012) chapter 1/1002 pages.

[121] "Semiconductor material for solar cells", *TU Delft OpenCourseWare.* Chapter 3. https://ocw.tudelft.nl/course-readings/solar-cells-r3-semicon-materials/.

[122]R. E. Hummel:"Electronic Properties of Materials", *Springer-Verlag, New York, Inc.* (1985) Fourth Edition (2010) 440 pages.

[123]D. Wolpert, P. Ampadu:"Managing temperature effects in nanoscale adaptive systems", *Springer-Verlag, New York*. (2011) 174 pages.

[124]A. Marikani: "Engineering physics", *PHI Learning Pvt. Ltd.* (2013) 426/ 504 pages.

[125]Freude: "Molecular physics", *Nature science*, **4** (2012) Chapter 3, 276-285. http://home.uni-leipzig.de/energy/freume.html.

[126]G. Brodie, M. V. Jacob, P. Farrel: "Microwave and radio-Frequency technologies in agriculture: an introduction for agriculturalists and engineers", *Walter de Gruyter GmbH & Co KG.* (2016) 369 pages.

[127]A. J. Moulson and J. M. Herbert: "Electroceramics: materils, properties, applications", *John Wiley & Sons*, 2nd edition 52 (2003) 576 pages.

[128]R. C. Buchanan: "ceramic materials for electroncs: processing, properties, and applications", *MDekker*, *NewYork.* (1991) 532 pages.

[129]D. R. Askeland, P. P. Fulay, W. J. Wright "The Science and Engineering of Materials", *Cengage Learning.* (2010) 896 pages.

[130]A. V. Dova and M. I. Kalogerasö: "Thermal analysis of polymers: fundamentals and applications", *John Wiley & Sons, Inc.*: 1st Edition (2008) Chapter 6/ 613.

[131] J. L. Liu: "Poisson's equation in electrostatics", *National Hsinchu University of Education* (2011).

[132]S. Lanfredi, C. Darie, F. S. Bellucci, C. V. Colin and M. A. L. Nobre: "Phase transitions and interface phenomena the cryogenic temperature domain of a niobate nanostructured ceramic", *J. The Royal Society of Chemistry. Dalton Trans.* **43** (2014) 10983–10998.

[133]M. A. L. Nobre and S. Lanfredi : "Negative temperature coefficient thermistor based on $Bi_3Zn_2Sb_3O_{14}$ ceramic: An oxide semiconductor at high temperature", *J. Appl. Phys,* **82** (2003) 2284;

[134]S. Lanfredi, G. Palacio, F. S. Bellucci3, C. V. Colin and M. A. L. Nobre: " Thermistor behaviour and electric conduction analysis of Ni-doped niobate ferroelectric: the role of multiple β parameters , *J. Appl. Phys.* **45** (2012) 435302.

[135]Crystal Structure Analysis: Essence of diffraction: Bragg Diffraction, http://www.chem.uci.edu/~lawm/263%204.pdf

[136]H. Bob: "Energy Dispersive Spectroscopy on the SEM",http://www.charfac.umn.edu/instruments/eds_on_sem_primer.pdf

[137]P.J. Potts, J.F. Bowles, S.J. Reed and R. Cave: "Microprobe techniques in the earth sciences", *The Mineralogical Society, Springer US.* ***6*** (1995) 408 pages.

[138]L. Nasdala, D. C. Smith, R. Kaindl and M. A. Ziemann: "Raman spectroscopy: analytical perspectives in mineralogical research", *EMU Notes in Mineralogy*. **6** (2004) Chapter 7/ 281–343 pages.

[139]Prinsceton Instruments, Raman Spectroscopy Basics. Retrieved from www.piacton.com.

[140]Dilatometry, Analyzing & Testing, NETZSCH, www.netzsch.com/n33623

[141]R. E. Hummel: "Science history, properties, applications", *Springer-Verlag New York, LLC.* (1998) Second Edition (2004).

[142]R. Moos , K. Sahner, M. Fleischer , U. Guth, N. Barsan and U. Weimar: "Solid State Gas Sensor Research in Germany – a Status Report", *Sensors* 2009, ***9*** **(2009)** 4323-4365; doi:10.3390/s90604323

[143]CTI Reviews: "Chemistry, The Practical Science Chemistry", *Cram101 Textbook Reviews*, (2016) 496 pages.

[144]"booklet of Basics of Titration", Mettler-Toledo AG, Analytical, Schwerzenbach, Switzerland: *Market Support AnaChem* (2009).

[145]C. R. Silva, J. A. Simoni, C. H. Collins and P. L. O. Volpe: "Ascorbic acid as a standard for Iodometric titrations. an analytical experiment for general chemistry", *J. Chem. Educ.*, **76** (1999) 1421.

[146]R. E. Barsoukov, J. R. Macdonald: " Impedance spectroscopy: theory, experiment, and applications", *John Wiley & Sons.* Second Edition (2005) 608 pages.

[147]D.C. Sinclair, P.B. Morrison, F. Velasco and A. R. WEST:" Use of blocking In/Ga electrodes for conductivity measurements", *J. solid State Ionics.* **37** (1990) 295-298.

[148]S. Asanuma, H. Akoh, H. Yamada and A. Sawa: "Relationship between resistive switching characteristics and band diagramsof $Ti/Pr_{1-x}Ca_xMnO_3$ junctions", *J. physical review B.* **80 (**2009) 235113-8.

[149]H. S. Lee, H. H. Park and M. J. Rozenberg: "Manganite-based memristive heterojunction with tunable non-linear I–V characteristics", *J. Royal Society of Chemistry Nanoscale*. **7** (2015) 6444–6450.

[150]Manual, Novocontrol Technologies, issue:01/2007.

[151]Rainer Waser: "Proton Solubility in Undoped and Fe-doped SrTiO3: Temperature Dependence and Formation of Defect Associates"*, Philips GmbH Forschungslaboratorium Aachen, Z. Naturforsch*. **42 a** (1987) 1356-1365.

[152]R. WASER: "Solubility of Hydrogen Defects in Doped and Undoped BaTi03", *J. Am. Cerarn.* Soc., **71** (1988) 58-63.

[153]M. V. Abrashev, J. Bäckström, L. Börjesson, V. N. Popov, R. A. Chakalov, N. Kolev, R.-L. Meng, M. N. Iliev: "Raman spectroscopy of $CaMnO_3$: Mode assignment and relationship between Raman line intensities and structural distortions", *Phzsical review B.* **6** (2002) 184301-9.

[154]V. G. Ivanov, V. G. Hadjiev, A. P. Litvinchuk, D. Z. Dimitrov, B. L. Shivachev, M. V. Abrashev, B. Lorenz, and M. N. Iliev: "Lattice dynamics and spin-phonon coupling in $CaMn_2O_4$: A Raman study", *Physical review B,* **89** (2014), 184307-8.

[155]J. Kim, X. Yin, K. C. Tsao, S. Fang, and H. Yang: "$Ca_2Mn_2O_5$ as oxygen-deficient perovskite electrocatalyst for oxygen", *J. Am. Chem. Soc.* **136** (2014), 14646−14649.

[156]K. R. Poeppelmeier, M. E. Leonowicz and J. M. Longo: "$CaMn0_{2.5}$ and $CazMn0_{3.5}$: new oxygen-defect perovskite-type oxides", *J. Solid State Chemistry.* **4** (1982) 89-98.

[157]J. Nowotny and M. Rekas : "Defect chemistry of (La,Sr)MnO_3", *J. Am. Ceram. Soc.* **81** (1998) 67–80.

[158]K. K. Bharathi, G. Markandeyulu and C. V. Ramana: " Microstructure, AC impedance and DC electrical conductivity characteristics of $NiFe_{2-x}Gd_xO_4$ (x = 0, 0.05 and 0.075)", *J. AIP ADVANCES.* **2** (2012) 012139.

[159]A. Varela, S. d. Dios, M. Parras, M. Hernando, M. T. F. Díaz, A. R. L. Cánovas and J. M. G. Calbet: "Ordere drock-salt related nanoclusters in $CaMnO_2$", *J. AM. CHEM. SOC.* **131** (2009) 8660–8668.

[160]R. Riedel, I. W. Chen: "Ceramics Science and Technology, Materials and Properties", *John Wiley & Sons.* (2015) 888 pages.

[161] Y. Wang, Y. Sui, H. Fan, X. Wang, Y. Su, W. Su and X. Liu: " High temperature thermoelectric response of electron-doped $CaMnO_3$", *J. Chem. Mater.* **21** (2009) 4653–4660.

[162]Anja Herpers: "Electrical characterization of manganite and titanate heterostructures", *Diss., RWTH Aachen University, Forschungszentrum Juelic*. **32** (2014)

[163]J. Briático, B. Alascio, R. Allub, A. Butera, A. Caneiro, M. T. Causa, and M. Tovar: "Double-exchange interaction in electron-doped $CaMnO_3$ 2d perovskites", *Physical review B.* **53** (1996) 4020-4.

Acknowledgements

I must express my deepest gratitude to my supervisor Professor Dr. Rainer Waser for giving me the opportunity to continue my study as a doctoral student at the Institute of Electrical Engineering and Information Technology IWEII at RWTH Aachen University / Peter Grünberg Institute 7 at the Forschungszentrum Jülich GmbH.

I would like to thank Professor Dr. Manfred Martin, the director of the Institute of Physical Chemistry at RWTH Aachen University for agreeing to be my second supervisor.

I want to thank my advisor at Forschungszentrum Jülich GmbH Dr. Christian Pithan for patient guidance, encourage and advice that he provided throughout my study as a PhD student. The present dissertation would never have been possible without his assistance.

I would also like to thank all the members of staff at RWTH Aachen University and Forschungszentrum Jülich GmbH, in particular Dr. Paul Meuffels, Cerstin Makovicka, Jochen Friedrich. Georg Pickartz, René Borowski, Marcel Gerst, Dr. Marco Moors and Dr. Felix Gunkel for nice dicussions and help to set up the experiment instduments.

I like to thank Dr. N. Lühmann who taught me how to work with Raman spectroscopy and solving the problems.

I feel indebted to my dear parents and my parents in law who experienced all of the ups and downs of my research. Special thanks go to my husband Reza Ghasemi for his continued support and encouragement.

Hiermit versichere ich, dass ich die vorliegende Arbeit selbständig verfasst und keine anderen als die angegebenen Quellen und Hilfsmittel verwendet habe.

Aachen, den 23 . 01 . 2018

Meimanat Rahmani

Band / Volume 40
Strained Silicon and Silicon-Germanium Nanowire Tunnel FETs and Inverters
S. Richter (2014), iii, 117 pp
ISBN: 978-3-95806-002-9

Band / Volume 41
Integration of Redox-Based Resistive Switching Memory Devices
F. Lentz (2014), i, 166 pp
ISBN: 978-3-95806-019-7

Band / Volume 42
Ladungstransportuntersuchungen an nanofunktionalen Bauelementen mit Diodencharakteristik basierend auf funktionalisierten Nanopartikeln
N. Babajani (2015), iv, 138, XLVII
ISBN: 978-3-95806-026-5

Band / Volume 43
Transport and Noise Properties of Nanostructure Transistors for Biosensor Applications
J. Li (2015), vii, 175 pp
ISBN: 978-3-95806-034-0

Band / Volume 44
Quantitative scanning tunneling spectroscopy of non-polar III-V compound semiconductor surfaces
M. Schnedler (2015), 122 pp
ISBN: 978-3-95806-075-3

Band / Volume 45
Model-based Algorithm Development with Focus on Biosignal Processing
Y. Yao (2015), x, 169 pp
ISBN: 978-3-95806-080-7

Band / Volume 46
Growth and characterization of crystalline rare-earth based thin oxide fims for the application as gate dielectric in nanotechnology
A. B. Schäfer (2015), xiii, 157 pp
ISBN: 978-3-95806-111-8

Band / Volume 47
TEM/STEM Investigations of Phase Change Materials for Non-volatile Memory Applications
M. Bornhöfft (2017), viii, 135 pp
ISBN: 978-3-95806-221-4

Band / Volume 48
Investigation of ternary nitride semiconductor alloys by scanning tunneling microscopy
V. Portz (2017), 140 pp
ISBN: 978-3-95806-232-0

Band / Volume 49
Redox processes and ionic transport in resistive switching binary metal oxides
K. Skaja (2017), VII, 203 pp
ISBN: 978-3-95806-236-8

Band / Volume 50
Investigation of switching mechanism in Ta_2O_5-based ReRAM devices
K. Wonjoo (2017), iii, 138 pp
ISBN: 978-3-95806-261-0

Band / Volume 51
Development of ReRAM-based Devices for Logic- and Computation-in-Memory Applications
T. Breuer (2017), x, 179 pp
ISBN: 978-3-95806-270-2

Band / Volume 52
Resistive switching memory devices from atomic layer deposited binary and ternary oxide thin films
N. Aslam (2017), X, 172 pp
ISBN: 978-3-95806-274-0

Band / Volume 53
Operando X-ray photoemission electron microscopy (XPEEM) investigations of resistive switching metal-insulator-metal devices
C. J. Schmitz (2017), IX, 153 pp
ISBN: 978-3-95806-283-2

Band / Volume 54
Optimization of powder and ceramic processing, electrical characterization and defect chemistry in the system $Yb_xCa_{1-x}MnO_3$
M. Rahmani (2018), XIV, 164 pp
ISBN: 978-3-95806-323-5

Information
Band / Volume 54
ISBN 978-3-95806-323-5

Mitglied der Helmholtz-Gemeinschaft

JÜLICH
Forschungszentrum